3D PRINTING IN THE BIOSCIENCES: APPLICATIONS FOR DIABETC COMPLICATIONS

By

Andre Castiaux II

A DISSERTATION

Submitted to
Michigan State University
in partial fulfillment of the requirements
for the degree of

Chemistry – Doctor of Philosophy

2018

ABSTRACT

3D PRINTING IN THE BIOSCIENCES: APPLICATIONS FOR DIABETIC COMPLICATIONS

By

Andre Castiaux II

Work presented in this dissertation demonstrates the utility of 3D printers in scientific research with specific applications to diabetic research. An overview of 3D printing techniques is discussed with special emphasis on PolyJet 3D printing. This printing technique is utilized to explore Cell-to-Cell communication in relationship to diabetes, binding of protein- ligand complexes under diabetic conditions, and teaching and research applications tangentially related to diabetes.

PolyJet 3D printing technology is a recent technique to the 3D printing field. It works by utilizing a liquid photocurable resin that can be sprayed onto a substrate layer by layer and cured into a final desirable three-dimensional object. With this printer multiple materials and colors can be incorporated into a single model. By incorporating multiple materials into a device, researchers can use the rubber like properties to imbed and seal various non-printable components into a rigid plastic device. One such non-printable component of interest is membranes for size exclusion of molecules up through cells.

Diabetes is characterized by the bodies inability to produce insulin (Type 1) or the bodies inability to effectively utilize the insulin produced (Type 2) leading to elevated glucose levels within the body. With this definition, there is an implication made that insulin is the only important molecule in relation to this disease. However, C-peptide is co-secreted with insulin and is suspected to play an important role in the health of the microvasculature. The ability to monitor the communication between cells types would

lend to a better understanding of the role of C-peptide under diabetic conditions. Specifically, looking at the communication of pancreatic β-cells, where C-peptide and insulin are synthesized, with red blood cells and endothelial cells, would allow researchers to understand the potential beneficial effects of C-peptide. Proposed within is a new ex vivo 3D printed platform that can selectively capture cells secretions while monitoring the effects on various cell types under both heathy and diseased states.

In addition to understanding the role of molecules no longer present or effective under diabetic conditions, it is important to understand the role of molecules synthesized under diabetic conditions. Specifically, the increased glucose concentration leads to the non-enzymatic addition of glucose (glycation) to long lived molecules in the body or Advanced Glycation End Products (AGEs) and can alter the behavior of molecules in vivo. A 3D printed device was developed to study the effect of glycation on albumins ability to bind zinc. It was determined that under healthy condition human serum albumin (HSA) will bind a maximum of 2 molecules of zinc per molecule of HSA whereas under diabetic or glycated conditions there is 1 molecule of zinc per 2 molecules of HSA.

In addition to research related to diabetic conditions, applications for 3D printing exist in labware and teaching aids. Utilizing 3D printers, cheap disposable pumps can be employed in hazardous conditions such as handling of radioactive materials. Data presented here demonstrates the development of a multichannel 3D printed peristaltic pump. The majority of the components are 3D printed and the pump is powered by a microcontroller and a continuous rotation servo motor. All in this pump can be assembled for under $150 and can achieve flow rates from 0.4 to 1.4 mL/ min.

ACKNOWLEDGEMENTS

First, I would like to acknowledge the sources of funding for this work: Michigan State University and the National Institute of Health. Without their financial support none of the work presented in this dissertation would have been possible. Additionally, with this support I was able to present this work on several occasions at various conferences throughout the Unites States.

I would like to thank my guidance committee, Dr. Gary Blanchard, Dr. Liangliang Sun, and Dr. Peter Lillehoj. Their advice and feedback has been invaluable throughout my research.

Additionally, I would like to thank Dr. Dana Spence my research advisor. Dr. Spence offered invaluable advice early in my graduate school career and eventually provided me with a home when my academic career was uncertain. Without his advice and the positive research environment that he has cultivated over the years, I would not have completed my dissertation. His passion for science and drive to advance the field is something that motivates all of his students, and I will carry this throughout my career.

No scientific advancement is accomplished by a single person, this is especially evident in the group atmosphere found within the Spence Group. I would like to thank Dr. Suzanne Summers, Dr. Tiffany Janes, and Dr. Hamideh Keshavarz, who, as more experienced members of the group set the example for quality of research and work ethic. They also provided invaluable guidance navigating life. A special thank you goes to Cody

Pinger without which many of my ideas would never have led to productive research. He provided invaluable insight in the all the areas where I was not as knowledgeable and was always available to discuss new ideas and experiments regardless of their worth. I would also like to thank Andrew Heller for his advice in learning to use the 3D printer. I would also like to acknowledge the contributions of the newer group members, Morgan Geiger, Marcus Bunn, Lisa Meints, and Brit Eggly. Their positive attitudes and fresh insight helped to make for a positive work environment.

Finally, I would like to thank my family and friends for all of their support over the years. My parents and grandparents have always been my motivation in life and they have always supported my no matter what direction I have chosen. Lastly, without my wife, Elena, I would be nowhere. She is the only constant in a life that is constantly changing and the reason I was able to accomplish this work.

TABLE OF CONTENTS

LIST OF TABLES

LIST OF FIGURES

Chapter 1 – Introduction to 3D printing

1.1 Introduction to 3D Printing

A large effort is being put forth by the scientific community to design and fabricate devices to advance research. These devices come in many forms, from custom glassware for analytical or synthetic chemical applications to microfluidic systems to assist in medical diagnosis.[1–3] In the past, research equipment was created by hand, as needed, by a machinist, glass blower, or other skilled tradesperson. While these people and techniques are (still) vital to advancing research and creating new devices and tools, the techniques can be time consuming or inaccessible to many. More recently, in-house fabrication of devices has become common in many scientific laboratories for the development of devices, microreactors, and other tools.[2,4–6] In addition, microfluidics is another area where in-house fabrication of devices is common; unfortunately, the reproducible production of polymer-based microfluidics suffers from lab-to-lab variability, and the technique becomes significantly more labor intensive as the design of the device becomes more complex.[7,8] Recently, scientists have been exploring new techniques for device fabrication that overcome the problems associated with previous methods.

A relatively new technique, 3D printing, has eagerly been adopted by the research community, as evident by a Web of Science database search involving “3D-printing” reporting over 40,000 references across all fields,[9] the majority of which were reported in the last 7 years (**Figure 1.1)**. An analysis of the reported fields (**Figure 1.2)** shows “Chemistry" with the fifth most citations for 2017.[9]

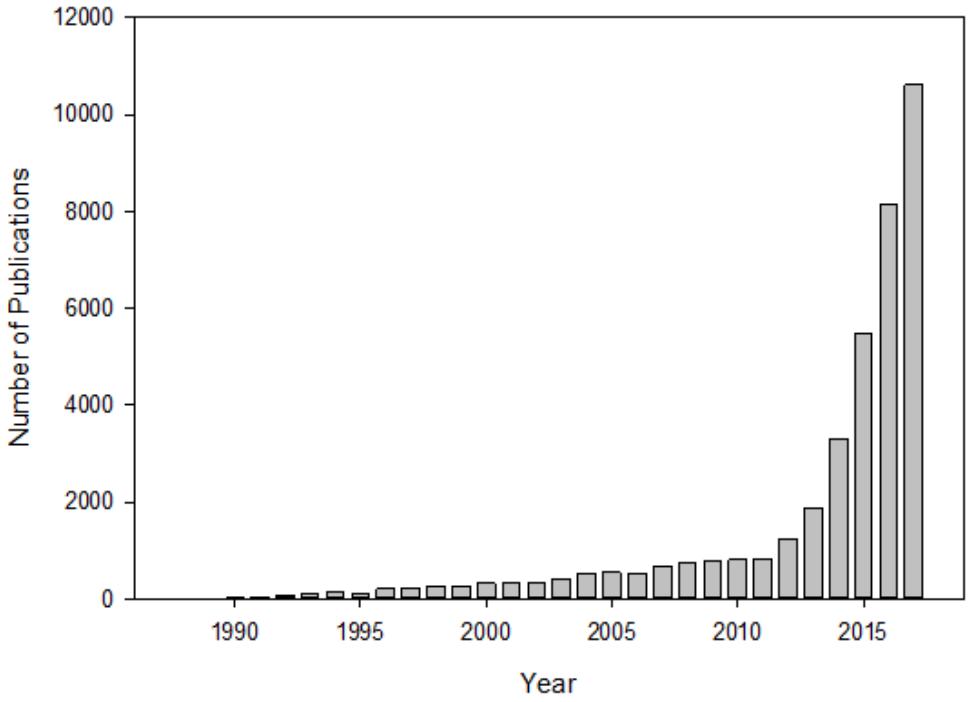

Figure 1.1: History of publications relating to 3D printing as reported by the web of science database.[9]

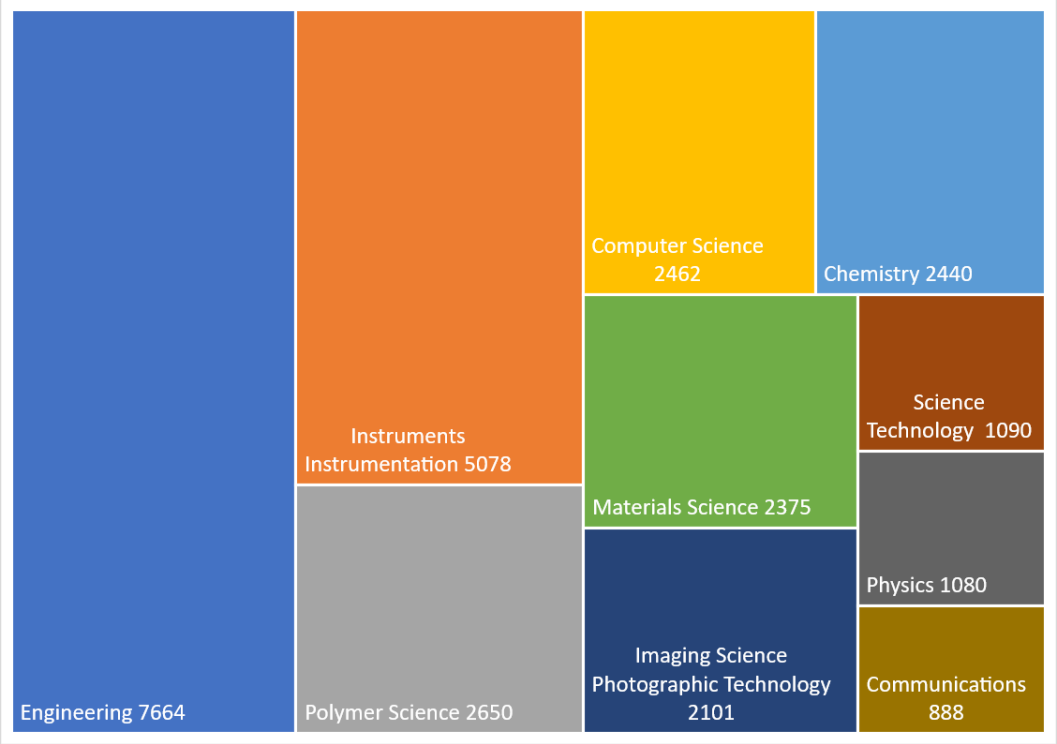

Figure 1.2: Publications relating to 3D printing for the publication year 2017 as reported by the Web of Science Database and broken up by division.[9]

3D printing is characterized as an additive manufacturing technique and works by building a physical model one layer at a time. The first “3D printer” was developed in the early 1980s by Charles Hull and was called a stereolithography apparatus (SLA).[10] Stereolithography uses light to selectively cure a liquid resin into a hard material.[10,11] Since Hull’s advancement of the SLA style 3D printer, there have been several different 3D printing machines developed, including extrusion machines, lamination machines, inkjet machines, and bioplotters. These machines can print multiple materials that have rubber-like properties to hard plastics, metals, and cement, or even biological components such as cells. These options have given researchers the ability to rapidly advance their research with customized specifications.

1.2 Types of 3D Printers

Many different types of 3D printers are currently available, each with their own advantages and disadvantages. This section will focus on the most commonly used 3D printing techniques in research. However, it should be noted that this is not an exhaustive list, and the list is ever growing.

1.2.1 Stereolithography Apparatus

The SLA printer was the first 3D printer, and since that time, the basic design has not changed significantly, although there have been significant advancements in resolution and efficiency.[12] **Figure 1.3A** shows how a typical SLA printer works.[10] The first iteration of the SLA used a vat of photocurable resin. A computer guided laser would selectively cure the top layer of the resin in the design of the desired model. A stage would then drop allowing fresh uncured resin to fill in on top. The laser would then cure the next layer, and then the process would repeat. The fact that there is a single point laser means

that the models can have very high resolution, with the XY resolution being determined by the laser spot size (100-200 μm for desktop versions and 20-30 μm for the highest resolution machines) and the Z resolution determined by the stage motor.[10,13–17] Though effective, this first SLA method has its drawbacks, specifically, a smaller laser spot size results in a longer production time of the model. In addition, as mentioned above, the model is pulled into the vat of resin resulting in a maximum model size being limited by the size of the resin vat. **Figure 1.3B** shows a new generation SLA, known as digital light processing printers (DLP).[10] The DLP printer uses a much smaller, but refillable, vat of resin and is essentially an inverted SLA printer. This means the stage now moves out of the vat of material, while the model is cured from the bottom of the resin bath.[10,18,19]

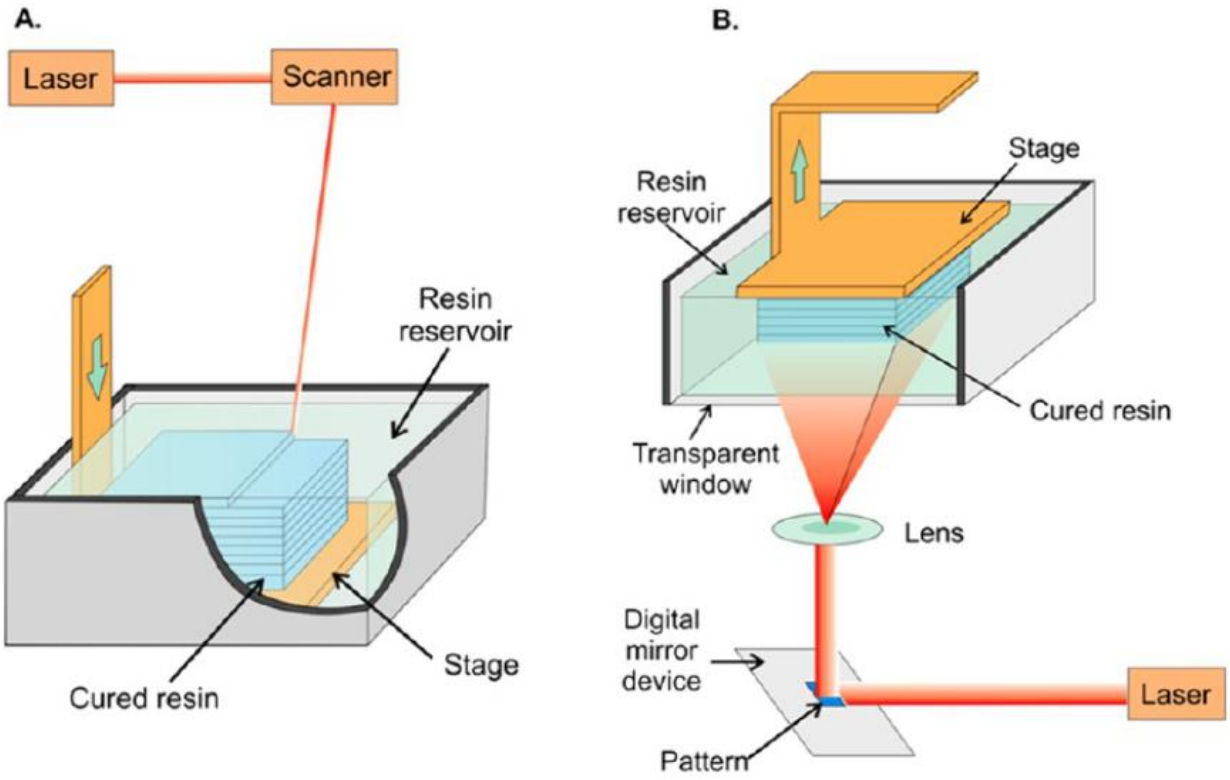

Figure 1.3: Sketch representations of (A) an SLA printer and (B) a DLP printer. The SLA printer uses a laser that scans from the top of the resin reservoir to selectively cure a model. The DLP printer uses a laser and mirrors angled either away from or towards the bottom of the resin reservoir to selectively cure the entire layer at one time.[10]

Instead of a laser, the DLP printer uses light projection and mirrors to cure the entire layer at one time, thus resulting in lower resolution than the SLA.[10,19] Typically, the highest resolution machines have an XY resolution of ~50 μm.[10,20] Additionally, these printers typically have a decreased resolution as the build platform is increased.

Both printers may require processing after printing if a smooth, finished surface is required, especially when support material is required. Some geometries like the letter L are self-supporting (**Fig 1.4A)**. However, **Figure 1.4B**, shows how the letter T would need supports during the print job. These supports are made from the same material as the model and are cut off at the end of the print job, and the products is then sanded smooth. The number of supports and the design of the supports determines the quality of the model. The need for these supports also make complex internal geometries, such as large channel networks, difficult.

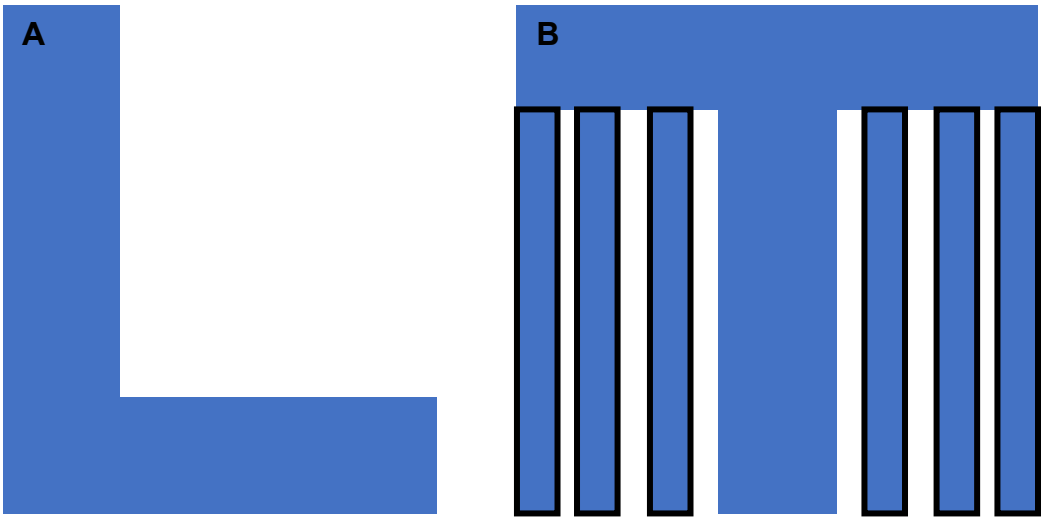

Figure 1.4.: Drawing representing support configuration for selected models printed with SLA, DLP, or FDM. (A) represents the letter L being printed completely support free also known as a self-supporting model. (B) represents the printing of the letter T which would require sacrificial support beams if printed in this geometry. These sacrificial supports (outlined in black) are printed in the same material as the model but would be removed after printing and sanded smooth.

1.2.2 Selective Laser Sintering Machines

In many ways, selective laser sintering (SLS) printers are like the traditional SLA printers. **Figure 1.5** shows the layout for a typical SLS printer.[10] The biggest difference with the SLS printer is that a powdered material is used instead of a photocurable liquid bath. In this format, metals and more durable plastics can be easily printed.[21,22] With this machine, a roller is used to evenly disperse a layer of powder. The material is then selectively heated by laser to its melting point, causing the material to bind together. While the SLS mechanism enables the printing of a wide variety of materials, the biggest advantage of this printer is the lack of support structures. Unlike the SLA printer, this printer does not need support structures because the print leaves excess powder on the print stage, supporting the model during the print process. This means that little to no post

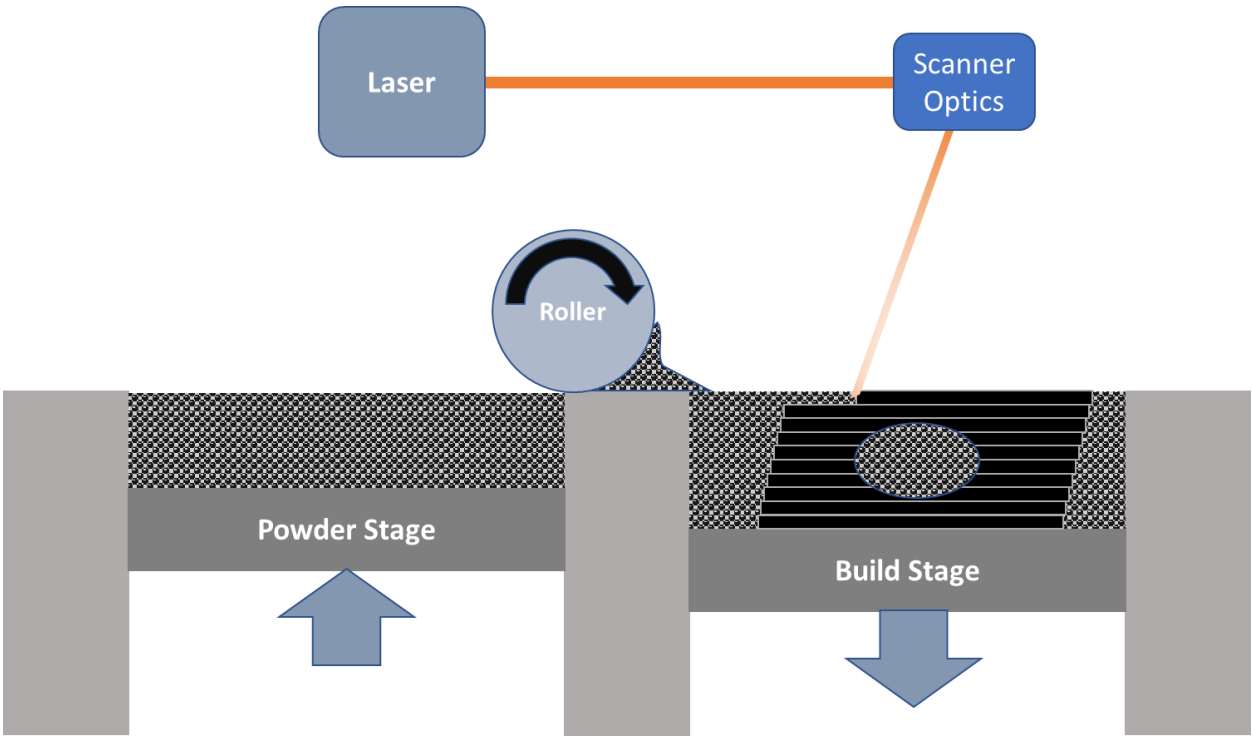

Figure 1.5: Representation of a SLS printer. In this machine, a laser is scanned to selectively sinter a powdered material to form the model. Once one layer is cured the roller delivers a fresh layer of powder for sintering.

processing is required with this method. However, fine detail is difficult to achieve with features typically limited to greater than 500μm.[22]

1.2.3 Extruder Machines

The most common 3D printer is the extruder machine, also called fused deposition modeling (FDM) printers. These are the least expensive printers on the market and found commonly in schools and libraries.[13] FDM machines typically use a solid thread of material that is made malleable, almost to the point of melting, as it is pulled through the extruder tip, as shown in **Figure 1.6**.[10] The material is laid on a stage, and typically, the tip moves up for additional layers. These machines are considered lower-resolution, with the industrial FDM printers generally having 200 μm XY resolutions.[21] This lower resolution requires sanding and post-processing for a show-quality model. However, FDM is advantageous over other types of printers because of the materials that can be printed,[8,21,22] which include a wide variety of thermoplastics. The most notable material printed by FDM is Polyether ether ketone (PEEK), a material known to be highly chemically resistant and a great option for 3D printed reactors or 3D printed analytical devices. Other notable materials are polycarbonate and acrylonitrile butadiene styrene (ABS).

While these materials are good options for use in chemistry, they are challenging to print. PEEK and polycarbonate are especially difficult because of the high extrusion temperature required to get the material in a malleable form.[21,23,24] High extrusion temperatures also requires that the model must be kept at a higher temperature to prevent uneven cooling, and thus warping of the model. While this printer allows the ability to print multiple materials or colors in a single build doing so complicates the printing process.[23,24]

The incorporation of multiple extruder heads into the design of the printer allows the printer to print one color per print head. Additionally, FDM machines can print different materials simultaneously, though the properties of the thermoplastics may cause difficulties as each material experiences different cooling characteristics, which can lead to layer separation or warping.[23,24]

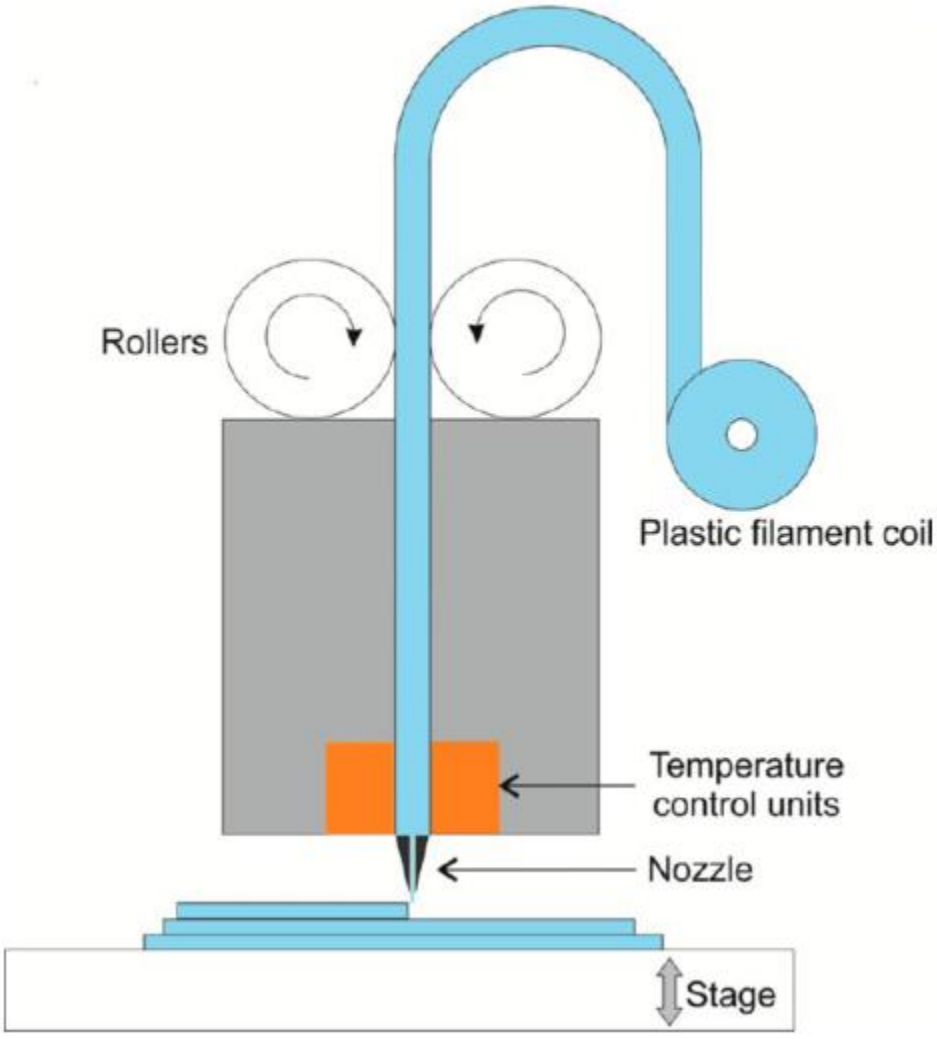

Figure 1.6: Representation of an FDM printer. Rollers feed a filament of material into a heater core at which point the material is brought to a malleable state and then pushed through the nozzle to be deposited on the build tray.[10]

1.2.4 Polyjet Machines

Polyjet machines, shown in **Figure 1.7**, are one of the most recently developed 3D-printer types and are considered to be the most versatile.[10,13,25,26] The machine essentially works like a desktop inkjet printer, in which multiple printheads are loaded with different photocurable resins. These resins are versatile and cover the entire color-spectrum, while incorporating materials that have characteristics from hard-plastics to rubber-like properties.[25,26] The printer builds a model one layer at a time by spraying one layer while a UV light source simultaneously cures the material. The stage lowers and then a new layer is sprayed and cured. An advantageous feature of this machine, besides being able to effectively lay-down different materials in a single print, is the printers ability to mix materials in the printing process.[13,27] Material mixing during printing enables hard-plastics and rubber-like plastics to be mixed concurrently resulting in varying degrees of firmness. Colors can be mixed in the same way to give true color gradients and provide more realistic prints. These printers exhibit high resolution, with XY being approximately 100 μm and the Z axis resolution being as low as 14 μm.[25] With this low of a Z-axis resolution, layer-lines are difficult to see with the naked eye, and very little post-processing is required.

For this type of printer, a paraffin-like sacrificial support material is used. This soft material is used to fill in voids and support the model during the build but does not leave hard protrusions like the scaffolding for SLA and FDM printers. The bulk of the material can be removed by hand, then the remaining material can be sprayed off using high-pressure water. Stratasys, the primary manufacturer of polyjet machines, has recently released a caustic soluble support material, making it easier to clean complex parts with

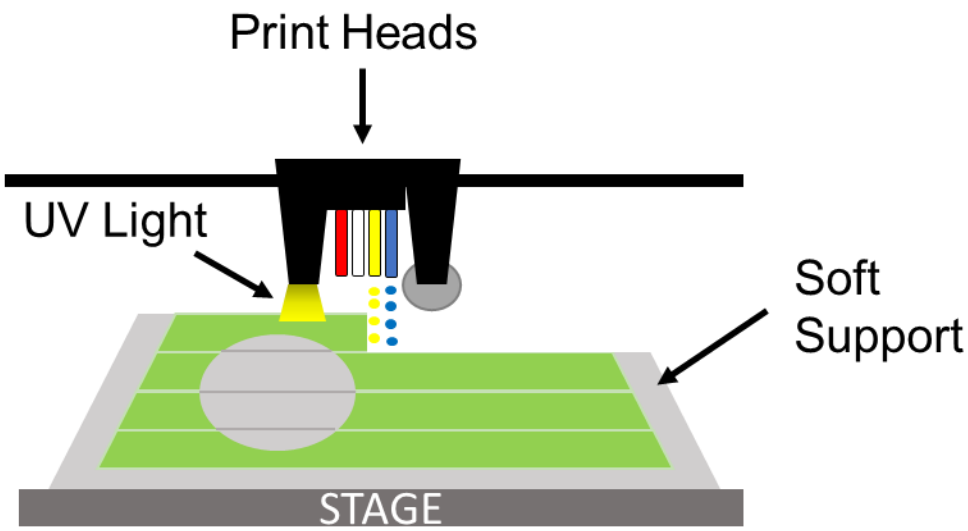

Figure 1.7: Depiction of a polyjet printer. The printer has multiple print heads for the different materials or for different colors. The printer can mix those materials as they are laid to produce a wide variety of colors and material properties. A UV light initiates the polymerization of the material, and while it is still soft a roller flattens out the layer.

fragile geometries by simply soaking the printed parts in a 2% sodium hydroxide solution. While this is an optimal technique for models with complex geometries and color patterns, the high resolution makes it a slow printing technique; printing an object the size of a soda can may take over 12 hours to print.

1.2.5 Bioprinting

Many believe that the future of 3D printing applications in the bio-sciences will be 3D printing biological molecules and cells.[14,25,28–30] Bioplotters are a type of 3D printer that can lay cells, gel matrices, or biomolecules onto 2D platforms or within 3D scaffolds.[21,23,31,32] Some of the first bioprinters, shown in **Figure 1.8**, were made in the early 2000s from modified commercial inkjet printers.[33,34] The early versions used cleaned-out ink cartridges and filled the different color cartridges with varying protein solutions. With this modification, any pattern that could be made in Micfrosoft PowerPoint or Word can be printed with color settings turned on to lay the various biological

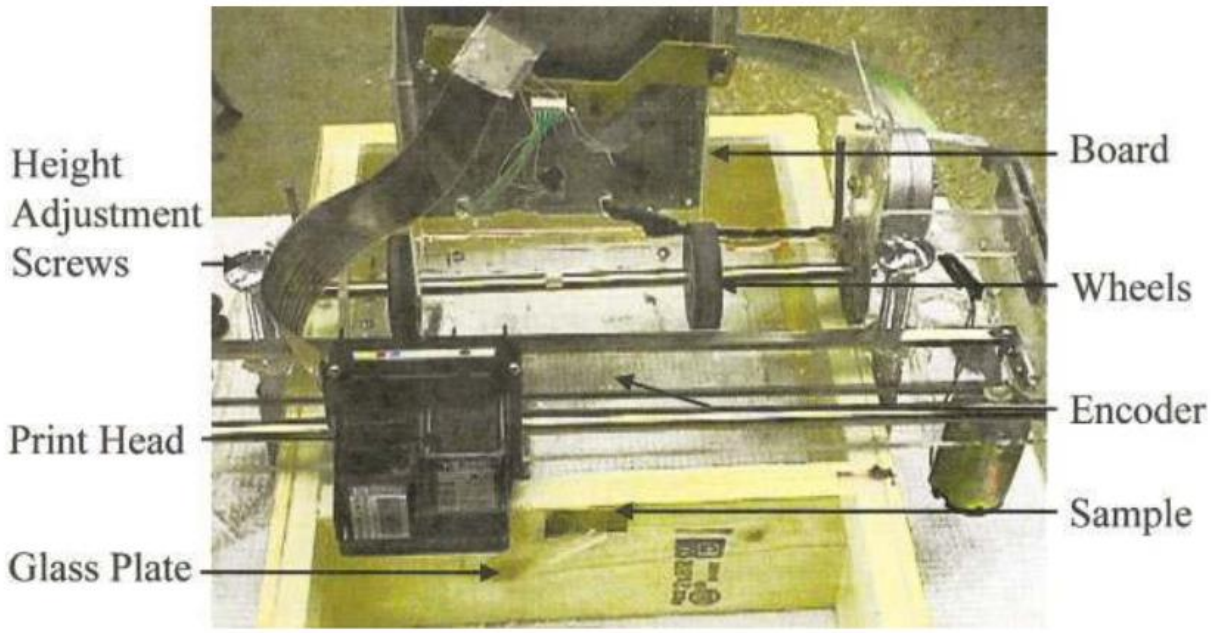

Figure 1.8: Picture of one of the fist bio plotters. This machine used an inkjet print cartridge from a desktop printer. The print cartridge was cleaned out and loaded with either a protein solution for protein printing or a suspension of cells for laying cells.[31]

molecules.[33,34] A similar procedure was used for the early cell printers, although instead of loading the cells into ink cartridges, the cell solution was loaded into a sterile syringe needle, and the needle was screwed onto the end of the print head.[34] By varying the size of the syringe, the maximum number of cells that can be printed in single sport can be controlled.

Envision TEC carries the most complex commercially available bioplotter.[35] This bioplotter, which can lay down porous scaffolding, change tips, and then fill the scaffolding with cells, works much like an FDM printer. The porous scaffolding is deposited through an extrusion process identical to FDM.[35,36] The cell matrix is patterned through a needle that uses a pump to move the solution into the scaffold. Since this printer pumps the cells to the location where they are placed, the number of cells that can be printed is not limited

to the size of a syringe. Another feature of the bioplotter is that the reservoir can be both temperature and gas controlled, which can be used to optimize cell-culture conditions.[35,36]

An ideal application of this technology is whole-organ printing.[32,37] Thus far, the first major advancement in whole-organ printing with a bioplotter was the printing of the scaffold and laying of cells for the production of a full human ear on to an appropriate scaffolding.[37] In addition, other groups have 3D printed vasculature features, and there is a group at Harvard working toward the 3D printing of structures that mimic kidney function.[29,30,38]

1.3 Files for 3D Printing

In order to print an object, a computer file containing the details of the object must first be created and then submitted to the printer. Libraries of printable files have become openly accessible and common in the 3D printing community. These include sites such as thingiverse.com, grabcad.com, and even an NIH site launched in 2014: the NIH 3D Print Exchange. It has also become common place during publication to submit files of 3D printed parts for inclusion in supplemental material.

1.3.1 Making Printable Files

Several different software packages for creating 3D printable models are available, some being free to download and use, and others requiring payment. A few of these packages include SolidWorks, SiemensNX, and Autodesk. Essentially, they all function in the same way by enabling a user to create custom three-dimensional sketches. The software has a platform for quick and easy conversion into a file format that can be interpreted by the 3D printer.

The most common file format is the .STL. The .STL abbreviation is for stereolithography, and it is the oldest and most widely used 3D printer format.[23,39,40] It has also become known as standard triangle language, which accurately describes what is happening when CAD software converts to this format. Using a three-dimensional coordinate system, the CAD software takes the smooth CAD drawing and fits triangles onto the surface, assigning coordinates to the triangle vertices. **Figure 1.9** shows the output of a .STL conversion where the top left is the CAD design and rotating counter clock wise is a higher and higher resolution .STL. As more triangles are incorporated, the resolution will increase, as will the file size; however, the final model will more closely resemble the intended design. This is a very limited file format because the file only

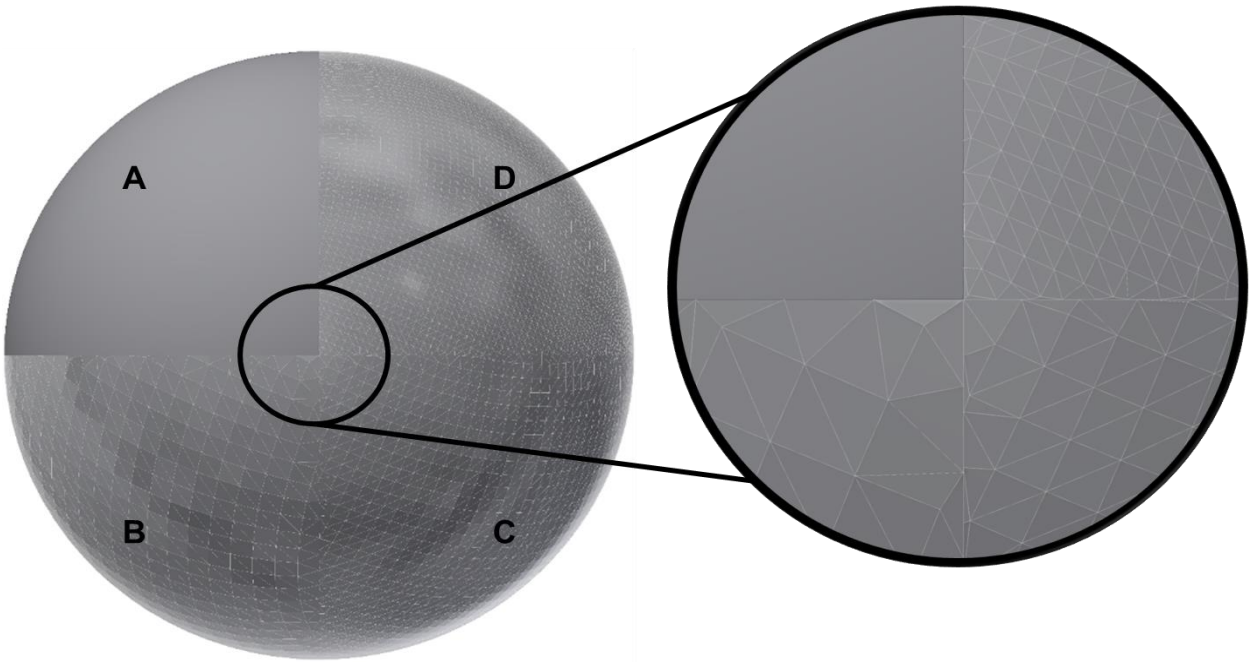

Figure 1.9: Sphere drawn in Autodesk Inventor to display triangulation when CAD file is converted to an .STL at different resolutions. Quadrant A is the standard CAD representation, so the surface is completely smooth. Quadrant B is a low resolution conversion to .STL. Quadrant C is a medium resolution .STL. Quadrant D is a high resolution .STL. As can be seen in the expanded view there are increasing triangles with increased resolution doing this increases the surface quality of the model.

consists of a series of surface coordinates; there are no imbedded colors, material properties, or units associated with the model.[39]

With 3D printers now printing in full color, one file format that is become more popular is virtual reality modeling language, or VRML (.wrl).[39,41–44] VRML originated in 1994 and was originally designed for use on the internet.[43] The VRML format stores all the vertices and vectors in a similar way to the .STL, but also encodes color and texture with each shape.[42] This allows the designer to imbed the full color spectrum into the model. However, since this was originally designed for virtual reality applications, there is no imbedded function for different material properties. Stratasys has been working towards fixing that issue by incorporating material properties into a 3D printed model in the form of a Voxel print. [20,27,45]

A voxel is the three-dimensional equivalent to the pixel. Voxel print requires the user to program the material and color properties of each of the voxels in the model.[27] With the ability to program each voxel to be a unique material, one can design functionality into a model. For example, it is possible to design a rod that bends in the Y direction but is rigid in the X direction. This application is currently being used by a group in the Netherlands to fabricate custom-made prosthetics.[45] Specifically, they use Voxel prints to fabricate the socket for a prosthetic leg. By using a gradient of material for the socket that goes over the amputated leg they can create a custom fit that is much more comfortable and less likely to cause pain.[45]

1.3.2 Additional Methods for Making Printable Files

In addition to designing custom-made files, much effort is being put forth to scan physical objects and print 3D representations. Much of the original work in converting

physical objects into digital or printable objects comes from topological scanning methods and is well reviewed in literature.[46–48] The history of scanning and digitizing physical objects is older than 3D printing and much more mature. Commercially available 3D scanners have been developed that use lasers to trace surfaces to sub-micron scale, resolutions even the best 3D printers cannot reproduce.

The field of customized medicine is an interesting and rapidly growing field where recently, researchers are developing 3D printer files from patient scans. Specifically, researchers are working on the conversion of medical scans such as computerized axial tomography (CT) and magnetic resonance imaging (MRI) for 3D printing to help with customized treatment and surgical preparations.[10,21,32,46,49] Further details about how this data translation occurs and applications will be discussed in chapter four.

1.4 Future of 3D Printing

As with all technology, 3D printing is rapidly improving. There are many groups around the world working toward the advancement of 3D printing resolution, printing techniques, and materials. From a chemist's perspective, the greatest need for improvements are in two areas: resolution and materials.

Resolution is defined as the smallest feature that can be accurately represented in the final model. The majority of 3D printers available on the market have an XY resolution around 150 μm. This resolution means that channels fabricated as part of a microfluidic device are limited to 400 μm or larger for fluid flow. This is not high enough resolution to reach the narrow channels sizes commonly used in microfluidic devices (<100 μm). There are custom-made SLA and DLP printers that can achieve resolutions fine enough to print sub 100 μm channels by limiting the build platform size and utilizing very expensive

mirrors and lasers. However, at this resolution, channels are left rough and irregularly shaped, similar to the image shown in **Figure 1.10**.[50] This leads to sanding, filling, or coating steps to make the channels usable.

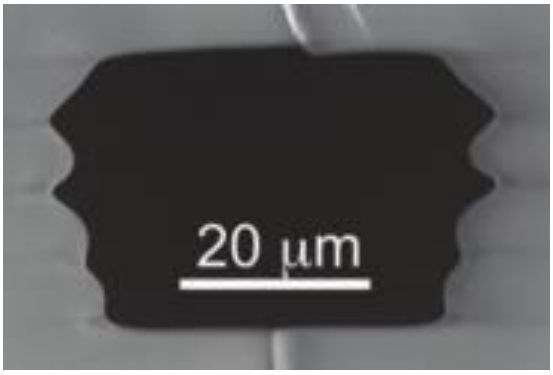

Figure 1.10: SEM image of an SLA printed 30 µm channel. This shows how irregularly shapes a circular channel is are being printed.[50]

As far as materials are concerned, there is a wide array of available materials ranging from soft rubber-like to thermoplastics with good chemical and physical properties. However, there is a mismatch between the printers with the best materials and the printers with the best resolution. The FDM printers have the lowest resolution but have the best material compatibility. Whereas with the polyjet machine, the machine with very high resolution and the ability for full color and mixed materials is limited to photocurable resins. These resins have been shown to have poor chemical compatibility, especially with organic solvents and can be cytotoxic. They also exhibit poor physical characteristics, often brittle, and easily deformable at temperatures as low as 50°C.

The future applications of 3D printing will be oriented more towards research applications. In the past, most 3D printing machines have been used or developed for the purpose of rapid prototyping design elements, or to demonstrate function or fitting of parts that will need to be machined at a later date. With more researchers and chemists getting

involved in the development of 3D printers, we will see a drastic increase in resolution, material capabilities, and function over the next few years.

1.5 Motivation for Dissertation

The incorporation of 3D printing in to research settings has neither been quick nor widely accepted. When the Spence group started utilizing 3D printing technology in the late 2000's, commercial 3D printing was still in it's infancy. However, since then, there has been a massive boom in both 3D printing technology and application. The use of 3D printers has pushed innovation in the Spence group, drastically decreasing fabrication times and decreasing the need to remake devices. The Spence group has pushed the use of 3D printers for blood-based analysis and cell to cell communication. The work herein will expand on these applications with each chapter broken into new potential applications. Chapter 2 will focus on a new platform for selective cell-to-cell communication. By utilizing 3D printing multiple cell types can be incorporated into a single device to mimic interactions within the body. Chapter 3 will focus on utilizing 3D printed devices for the determination of ligand-protein binding constants. Commercially available devices exist for use in determining binding between proteins and smaller molecules, however, these devices can be expensive and selection is often a limiting factor. Chapter 4 will focus on the use of 3D printing for functional applications and teaching applications. Specifically, the chapter will highlight the construction of a 3D printed multi-channel peristaltic pump and the use of the 3D printed organ models for surgical aids. The chapter 5 will give guidance on possible future directions for 3D printed devices for studying blood flow under a variety of conditions.

REFERENCES

REFERENCES

(1) Schmuckler, J. S. Homemade Lab Equipment. J. Chem. Educ. **1984**, 61 (4), 1984.

(2) Whitesides, G. M. The Origins and the Future of Microfluidics. Nature **2006**, 442 (7101), 368–373.

(3) Han, Y.; Kingston, H. M.; Richter, R. C.; Pirola, C. Dual-Vessel Integrated Microwave Sample Decomposition and Digest Evaporation for Trace Element Analysis of Silicon Material by ICPMS: Design and Application. Anal. Chem. **2001**, 73 (6), 1106–1111.

(4) Mahadeva, S. K.; Walus, K.; Stoeber, B. Paper as a Platform for Sensing Applications and Other Devices: A Review. ACS Appl. Mater. Interfaces **2015**, 7 (16), 8345–8362.

(5) Gravesen, P.; Branebjerg, J.; Jensen, O. S. Microfluidics-a Review. J. Micromechanics Microengineering **1993**, 3 (4), 168–182.

(6) Sackmann, E. K.; Fulton, A. L.; Beebe, D. J. The Present and Future Role of Microfluidics in Biomedical Research. Nature **2014**, 507 (7491), 181–189.

(7) Whitesides, G. M. Solving Problems. Lab Chip **2010**, 10 (18), 2317.

(8) Kim, L.; Toh, Y. C.; Voldman, J.; Yu, H. A Practical Guide to Microfluidic Perfusion Culture of Adherent Mammalian Cells. Lab Chip **2007**, 7 (6), 681–694.

(9) No Title webofknowledge.com (accessed Jun 8, 2018).

(10) Gross, B. C.; Erkal, J. L.; Lockwood, S. Y.; Chen, C.; Spence, D. M. Evaluation of 3D Printing and Its Potential Impact on Biotechnology and the Chemical Sciences. Anal. Chem. **2014**, 86 (7), 3240–3253.

(11) Schubert, C.; Van Langeveld, M. C.; Donoso, L. A. Innovations in 3D Printing: A 3D Overview from Optics to Organs. Br. J. Ophthalmol. **2014**, 98 (2), 159–161.

(12) Hull, C. United States Patent 4,575,330, 1986.

(13) Manzanares Palenzuela, C. L.; Pumera, M. (Bio)Analytical Chemistry Enabled by 3D Printing: Sensors and Biosensors. TrAC - Trends Anal. Chem. **2018**, 103, 110–118.

(14) Ngo, T. D.; Kashani, A.; Imbalzano, G.; Nguyen, K. T. Q.; Hui, D. Additive Manufacturing (3D Printing): A Review of Materials, Methods, Applications and Challenges. Compos. Part B Eng. **2018**, 143 (December 2017), 172–196.

(15) Gross, B.; Lockwood, S. Y.; Spence, D. M. Recent Advances in Analytical

Chemistry by 3D Printing. Anal. Chem. **2017**, 89 (1), 57–70.

(16) Melchels, F. P. W.; Feijen, J.; Grijpma, D. W. A Review on Stereolithography and Its Applications in Biomedical Engineering. Biomaterials **2010**, 31 (24), 6121–6130.

(17) Xue, Y.; Gu, P. A Review of Rapid Prototyping Technology and Systems. Comput. Aided Des. **1996**, 28 (4), 307–318.

(18) Beauchamp, M. J.; Nordin, G. P.; Woolley, A. T. Moving from Millifluidic to Truly Microfluidic Sub-100-Mm Cross-Section 3D Printed Devices. Anal. Bioanal. Chem. **2017**, 409 (18), 4311–4319.

(19) Bhattacharjee, N.; Urrios, A.; Kang, S.; Folch, A. The Upcoming 3D-Printing Revolution in Microfluidics. Lab Chip **2016**, 16 (10), 1720–1742.

(20) Hiller, J.; Lipson, H. Design and Analysis of Digital Materials for Physical 3D Voxel Printing. Rapid Prototyp. J. **2009**, 15 (2), 137–149.

(21) Chia, H. N.; Wu, B. M. Recent Advances in 3D Printing of Biomaterials. J. Biol. Eng. **2015**, 9 (1), 1–14.

(22) Shirazi, S. F. S.; Gharehkhani, S.; Mehrali, M.; Yarmand, H.; Metselaar, H. S. C.; Adib Kadri, N.; Osman, N. A. A. A Review on Powder-Based Additive Manufacturing for Tissue Engineering: Selective Laser Sintering and Inkjet 3D Printing. Sci. Technol. Adv. Mater. **2015**, 16 (3), 1–20.

(23) Ligon, S. C.; Liska, R.; Stampfl, J.; Gurr, M.; Mülhaupt, R. Polymers for 3D Printing and Customized Additive Manufacturing. Chem. Rev. **2017**, 117 (15), 10212–10290.

(24) Hofmann, M. 3D Printing Gets a Boost and Opportunities with Polymer Materials. ACS Macro Lett. **2014**, 3 (4), 382–386.

(25) Chen, C.; Mehl, B. T.; Munshi, A. S.; Townsend, A. D.; Spence, D. M.; Martin, R. S. 3D-Printed Microfluidic Devices: Fabrication, Advantages and Limitations - a Mini Review. Anal. Methods **2016**, 8 (31), 6005–6012.

(26) Stratasys. No Title http://www.stratasys.com/materials.

(27) Richards, D.; Stratasys. Lancaster University Pushes Design Limits with GrabCAD Voxel Print Technology. 2017.

(28) Jariwala, S. H.; Lewis, G. S.; Bushman, Z. J.; Adair, J. H.; Donahue, H. J. 3D Printing of Personalized Artificial Bone Scaffolds. 3D Print. Addit. Manuf. **2015**, 2 (2), 56–64.

(29) Kolesky, D. B.; Homan, K. A.; Skylar-Scott, M. A.; Lewis, J. A. Three-Dimensional Bioprinting of Thick Vascularized Tissues. Proc. Natl. Acad. Sci. **2016**, 113 (12),

3179–3184.

(30) Homan, K. A.; Kolesky, D. B.; Skylar-Scott, M. A.; Herrmann, J.; Obuobi, H.; Moisan, A.; Lewis, J. A. Bioprinting of 3D Convoluted Renal Proximal Tubules on Perfusable Chips. Sci. Rep. **2016**, 6, 1–13.

(31) Jose, R. R.; Rodriguez, M. J.; Dixon, T. A.; Omenetto, F.; Kaplan, D. L. Evolution of Bioinks and Additive Manufacturing Technologies for 3D Bioprinting. ACS Biomater. Sci. Eng. **2016**, 2 (10), 1662–1678.

(32) Wang, K.; Ho, C. C.; Zhang, C.; Wang, B. A Review on the 3D Printing of Functional Structures for Medical Phantoms and Regenerated Tissue and Organ Applications. Engineering **2017**, 3 (5), 653–662.

(33) Xu, T.; Jin, J.; Gregory, C.; Hickman, J. J.; Boland, T. Inkjet Printing of Viable Mammalian Cells. Biomaterials **2005**, 26 (1), 93–99.

(34) Wilson, W. C.; Boland, T. Cell and Organ Printing 1: Protein and Cell Printers. Anat. Rec. - Part A Discov. Mol. Cell. Evol. Biol. **2003**, 272 (2), 491–496.

(35) Carvalho, C.; Bernum, R. Van; Siblani, A.; Gmbh, E. Generation 3D-Bioplotter To Satisfy the Ever-Increasing Requirements of Tissue Engineering Processes, a Major Step in the Development of the 3D-Bioplotter Has Been Taken. The 4. **2008**, 5027.

(36) Landers, S.; Pfister, A.; Hubner, U.; John, H.; Schmelzeisen, R.; Muhlaupt, R. Fabrication of Soft Tissue Engineering Scaffolds by Menas of Rapid Prototyping Techniques. J. Mater. Sci. **2002**, 37: 3107-3, 3107–3116.

(37) Mannoor, M. S.; Jiang, Z.; James, T.; Kong, Y. L.; Malatesta, K. A.; Soboyejo, W. O.; Verma, N.; Gracias, D. H.; McAlpine, M. C. 3D Printed Bionic Ears. Nano Lett. **2013**, 13 (6), 2634–2639.

(38) Murphy, S. V.; Atala, A. 3D Bioprinting of Tissues and Organs. Nat. Biotechnol. **2014**, 32 (8), 773–785.

(39) Hiller, J. D.; Lipson, H. STL 2.0: A Proposal for a Universal Multi-Material Additive Manufacturing File Format. Proc. 20th Solid Free. Fabr. Symp. **2009**, No. 1, 266–278.

(40) Seitz, H.; Rieder, W.; Irsen, S.; Leukers, B.; Tille, C. Three-Dimensional Printing of Porous Ceramic Scaffolds for Bone Tissue Engineering. J. Biomed. Mater. Res. - Part B Appl. Biomater. **2005**, 74 (2), 782–788.

(41) Stratasys. Using VRML Files For Color 3D Printing; 2015; pp 1–6.

(42) Taubin, G.; Horn, W. P.; Lazarus, F.; Rossignac, J. Geometry Coding and VRML. Proc. IEEE **1998**, 86 (6), 1228–1243.

(43) Ming, L. W.; Gibson, I. Specification of VRML in Color Rapid Prototyping. Int. J. CAD/CAM **2002**, 1 (1), 1–9.

(44) Chen, T.-H.; Lee, S.; Flood, A. H.; Miljanić, O. Š. How to Print a Crystal Structure Model in 3D. CrystEngComm **2014**, 16 (25), 5488–5493.

(45) Doubrovski, E. L.; Tsai, E. Y.; Dikovsky, D.; Geraedts, J. M. P.; Herr, H.; Oxman, N. Voxel-Based Fabrication through Material Property Mapping: A Design Method for Bitmap Printing. CAD Comput. Aided Des. **2015**, 60, 3–13.

(46) Goyanes, A.; Det-Amornrat, U.; Wang, J.; Basit, A. W.; Gaisford, S. 3D Scanning and 3D Printing as Innovative Technologies for Fabricating Personalized Topical Drug Delivery Systems. J. Control. Release **2016**, 234, 41–48.

(47) Remondino, F.; El-Hakim, S. Image-Based 3D Modelling: A Review. Photogramm. Rec. **2006**, 21 (115), 269–291.

(48) Blais, F. Review of 20 Years of Range Sensor Development. J. Electron. Imaging **2004**, 13 (1), 231.

(49) Ventola, C. L. Medical Applications for 3D Printing: Current and Projected Uses. P T **2014**, 39 (10), 704–711.

(50) Gong, H.; Bickham, B. P.; Woolley, A. T.; Nordin, G. P. Custom 3D Printer and Resin for 18 Mm × 20 Mm Microfluidic Flow Channels. Lab Chip **2017**, 17 (17), 2899–2909.

Chapter 2 – Novel Platform for Cell-to-Cell Communication

2.1 Background

2.1.1 Introduction to Diabetes

Diabetes mellitus is a disease characterized by the body's inability to produce or respond to insulin, resulting in elevated blood glucose levels.[1] While different forms of this disease exist, the two most prominent forms are type 1 and type 2. Data from 2015 estimates that 30.3 million Americans have some form of diabetes.[2] Of these 30.3 million Americans, an estimated 23.8% are living with undiagnosed diabetes, which translates to $245 billion in total direct and indirect health-related costs in the United States.[2] The health-related costs equate to about $13,700 per year for the average person with diabetes.[2] Of course, these are just the numbers in the United States for 2017; the values globally are much higher and projected to increas.[3,4]

2.1.2 Types of Diabetes and Treatment

2.1.2.1 Type 1 Diabetes

Type 1 diabetes (T1D) typically develops during early childhood and is also known as juvenile diabetes.[5–7] T1D affects about 1.25 million Americans, or about 0.3% of the United States population.[1] It is caused by a lack of insulin production, which is brought on by the destruction of the β-cells in the pancreas, where insulin is produced.[5–7] Cell death can occur rapidly or slowly and varies greatly from case to case.[7] While younger patients who develop T1D typically show symptoms rapidly, some patients may retain partial β-cell function for years and remain moderately healthy without immediate treatment.[7] Due to the destruction of β–cells, people with T1D require exogenous insulin

for survival. Typically, people with T1Dhave a genetic predisposition for the disease, but it can be triggered by certain environmental factors that are not well characterized.[7] Failure to properly regulate the blood sugar or the symptoms caused by the disease can lead to death.

2.1.2.2 Type 2 Diabetes

Type 2 diabetes (T2D), also known as adult onset diabetes, typically occurs later in life and is defined by insulin resistance; that is, the body still produces insulin, but it is not having beneficial effects in vivo.[5,6,8,9] T2D is the predominant form of diabetes, affecting 90-95% of all people with diabetes.[7,8] In this form of the disease, β-cell destruction does not typically occur.[9] Instead, T2D is often caused by obesity, or in some cases excess fat around the abdominal region.[1,2,5,6,10] This type of diabetes can go undiagnosed for years because the symptoms develop gradually and may not be severe enough for patients to notice any immediate changes in their health. Once T2D is diagnosed, treatment comes in the form of recommended lifestyle changes. T2D can be mitigated for years and in some cases reversed with strict diet monitoring and exercise.[1,5,7] If diet and exercise fail, T2D can be regulated by medications.[11–13] When T2D is not treated appropriately, the results can be just as severe as T1D.

2.1.3 Diabetic Complications

While several forms of diabetes exist, the long-term complications do not differ greatly because the root cause of the complications is the same. These long-term complications include retinopathy, nephropathy, neuropathy, and macrovascular complications.[14–16] Retinopathy, disease of the eye, can lead to blurred vison or even

blindness. Nephropathy is damage to the kidneys and can range from impaired ability to filter blood to as severe as full kidney failure and cell death.[5,8,10,14,17] Neuropathy is characterized by nerve damage. This can manifest as pain in various areas of the body or a complete loss of feeling in the extremities.[8,14,17] Diabetes can cause wound healing to occur more slowly and leads to high infection rates.[1,8,10] Infections, combined with loss of feeling, can lead to amputation of extremities due to the patient not seeking care. The above is characterized as microvascular disease. The last major complication for diabetics comes in the form of macrovascular complications such as heart attacks and strokes.[7,8,16,18] All of these complications can be related back to blood flow problems.

2.1.4 A Molecular Level View of Diabetes

2.1.4.1 Insulin

Glucose is largely regulated by insulin, which is secreted from pancreatic β-cell vesicles through a series of steps in the body. However, when someone has diabetes, insulin is either absent (T1D) or does not appropriately regulate the blood glucose levels(T2D). While the fasting plasma glucose level for a healthy individual is less than 5.6 mM, these levels are often greater than 7.0 mM for people with diabetes.[19,20] This increased glucose concentration is known as hyperglycemia.

Insulin, first discovered in 1921, is produced in the β-cells of the pancreas.[21–24] Insulin is first synthesized as proinsulin, an 86-amino acid hormone consisting of three distinct chains, located within the endoplasmic reticulum, namely the A chain, B chain, and C-chain. The C-chain connects the A and B chains (**Fig 2.1**) and is often known as C-peptide.[21,23,25] During insulin synthesis, C-peptide is holds the A and B chains in the

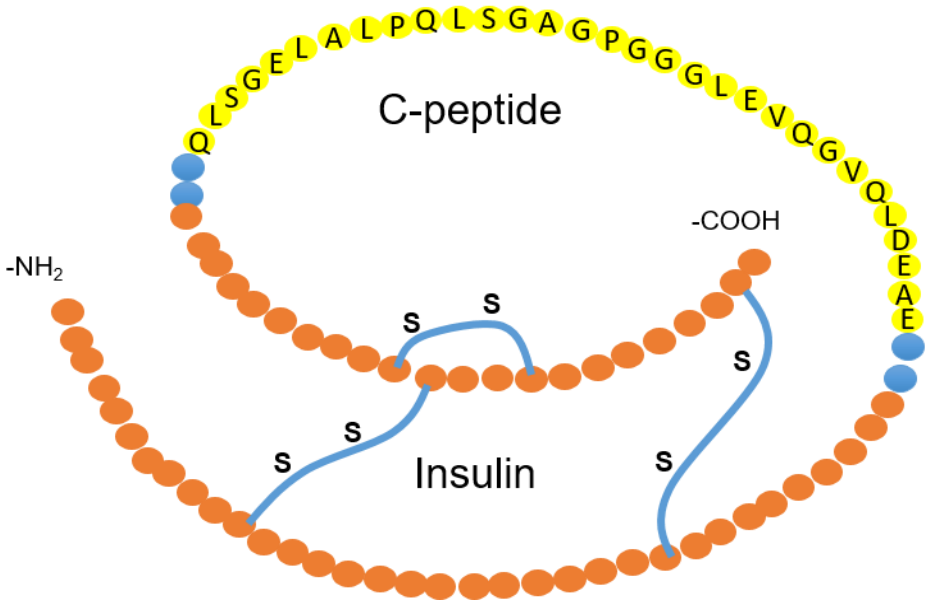

Figure 2.1: Structure of proinsulin with insulin shown in orange and C-peptide shown in yellow.[25]

right conformation for disulfide bond formation. The proinsulin is then transported to the Golgi apparatus where it is packaged into a vesicle.[21] Within the vesicle, the 31-amino acid chain of C-peptide is cleaved to produce the 51-amino acid mature form insulin. After cleavage of C-peptide, insulin is stored within the granules as a hexamer with two to four zinc ions bound to it.[26,27] When the insulin is needed, the granule migrates to the membrane of the β-cell (**Fig 2.2**), fuses with the membrane and releases insulin, C-peptide, zinc, and any remaining proinsulin into the bloodstream.[21–23]

Once released into the bloodstream, insulin moves throughout the body interacting with many cell types including fat, liver, and muscle cells. Insulin interacts with these cells in three main steps. First, insulin activates the GLUT4 transporter on the muscle and fat cells, increasing the amount of glucose available for glycolysis.[21,28,29] Insulin stimulates the liver cells to begin glycogenesis, which is the synthesis of a glucose polymer that is used to store glucose. Finally, insulin stops the production of glucagon from α-cells in the

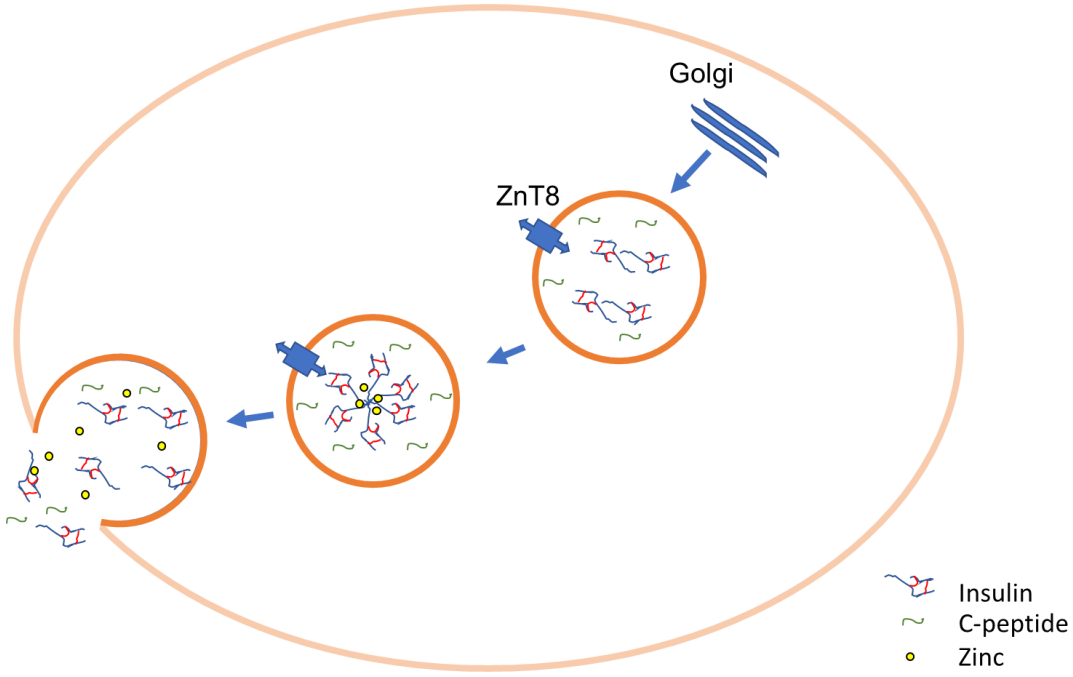

Figure 2.2: Pancreatic β-cell with the synthesis of insulin. Proinsulin is packaged into secretory vesicles within the golgi apparatus. Once in the vesicles the pH drops, and the proinsulin is cleaved into insulin and C-peptide. The ZnT8 transporter on the vesicle then bringing in Zn^{2+} where it is used to form insulin hexamers. The insulin hexamer binds up to 4 zinc atoms and exists in a crystal form with in the vesicle. Once the vesicle is called to the surface the pH increases rapidly to 7.4 at which time the insulin hexamer dissolves, dissociates, and is released into the bloodstream.

pancreas.[21,29] When insulin is not present (such as in T1D), these pathways cannot be activated and the glucose concentration in the body remains elevated. The glucose concentration also remains high when there is an insulin resistance in the body and the insulin cannot initiate these pathways.

2.1.4.2 C-peptide

C-peptide is produced during the natural synthesis of insulin and secreted at the same time in equimolar amounts. While most people believe C-peptide to be inactive in the body, there are studies, such as the Joslin Medalist Study in 2010, that suggest otherwise.[30,31] In this study, researchers looked at the presence of C-peptide in people

with type 1 diabetes who lived 50 years or more with the disease. Results showed that 67% of the patients tested had detectable levels of C-peptide.[30] This is important because the patients do not retain enough β-cell function to stop taking exogenous insulin but it is implied that the β-cell function that is retained is enough to increase quality of life. Other studies have also shown that the presence of C-peptide decreases the possibility of vascular disease in type 1 diabetics.[9,18,32]

While these are some of the more recent studies performed, researchers have hypothesized a biological function outside of the pancreas since C-peptide was discovered in 1967.[33] There are now two competing theories of how C-peptide works in the body. One suggests direct signaling at endothelial cells. The other is signaling at red blood cells (RBCs) to increase adenosine triphosphate (ATP) release. Both lead to increased vasodilation and improved blood flow.[17,32,34]

Early work with C-peptide focused on the direct release of nitric oxide (NO) from endothelial cells as the mechanism of increased blood flow.[35–37] The researchers

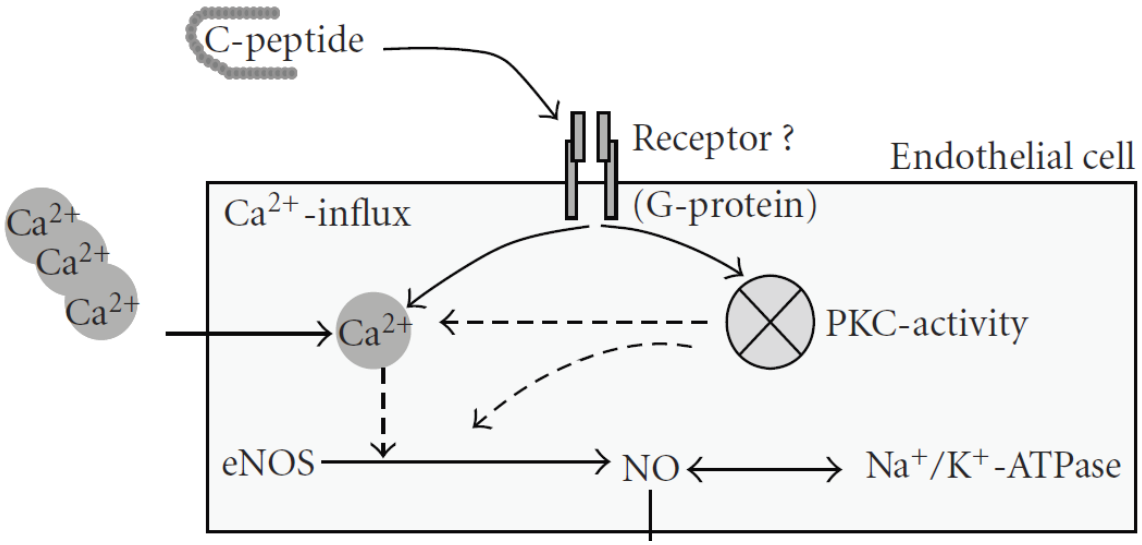

Figure 2.3: Proposed mechanism for direct C-peptide stimulation of nitric oxide from endothelial cells.[35]

hypothesize that there is a receptor located on the endothelial cell specific to C-peptide. This receptor is believed to activate the G-protein within the endothelial cell, which leads to increased calcium flux and an increase in NO production (**Fig 2.3**).[35–37] This pathway has been supported by other studies that specifically look at calcium influx in the presence of C-peptide.[37] However, reproducing these results between groups is inconsistent, even though there are animal and human trials that suggest there are positive effects in the function of microvasculature with the addition of C-peptide.[38–40] An alternative hypothesis for the mode of action for C-peptide may explain these trials.

An alternate hypothesis claims that C-peptide interacts with RBCs in the body, leading to an increase in ATP release from these cells. The released ATP then diffuses to the endothelial cells and stimulates NO production and release, subsequently increasing blood flow through vasorelaxation (**Fig 2.4**). One study that investigated NO production by an endothelium in the presence and absence of C-peptide utilized a membrane embedded in a polydimethylsiloxane device to separate flowing RBCs from

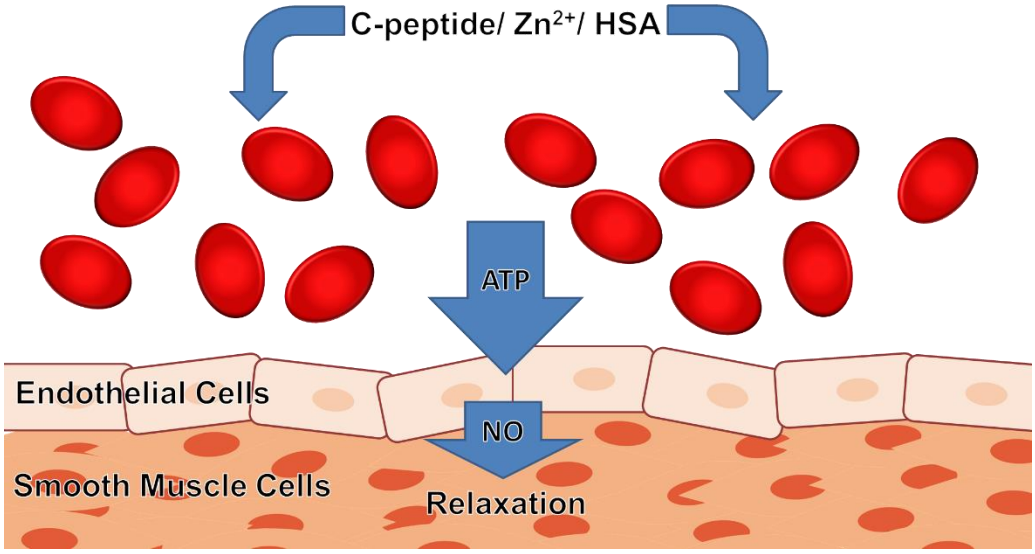

Figure 2.4: Proposed mechanism for releasing indirect release of nitric oxide through C-peptide interaction with RBCs and subsequent increase of ATP.

bovine endothelial cells.[41] **Figure 2.5** shows the relative fluorescent signals for flowing RBCs, flowing RBCs with Zn^{2+} and C-peptide, and buffer with Zn^{2+} and C-peptide (but no RBCs). It was reported that endothelial cells release the same amount of NO if there are only RBCs or only Zn^{2+} and C-peptide. An increase in NO release was only measured in the presence of RBC with Zn^{2+} and C-peptide. Direct ATP measurement experiments in a 3D-printed flow device confirmed these results.[17] However, a better understanding of

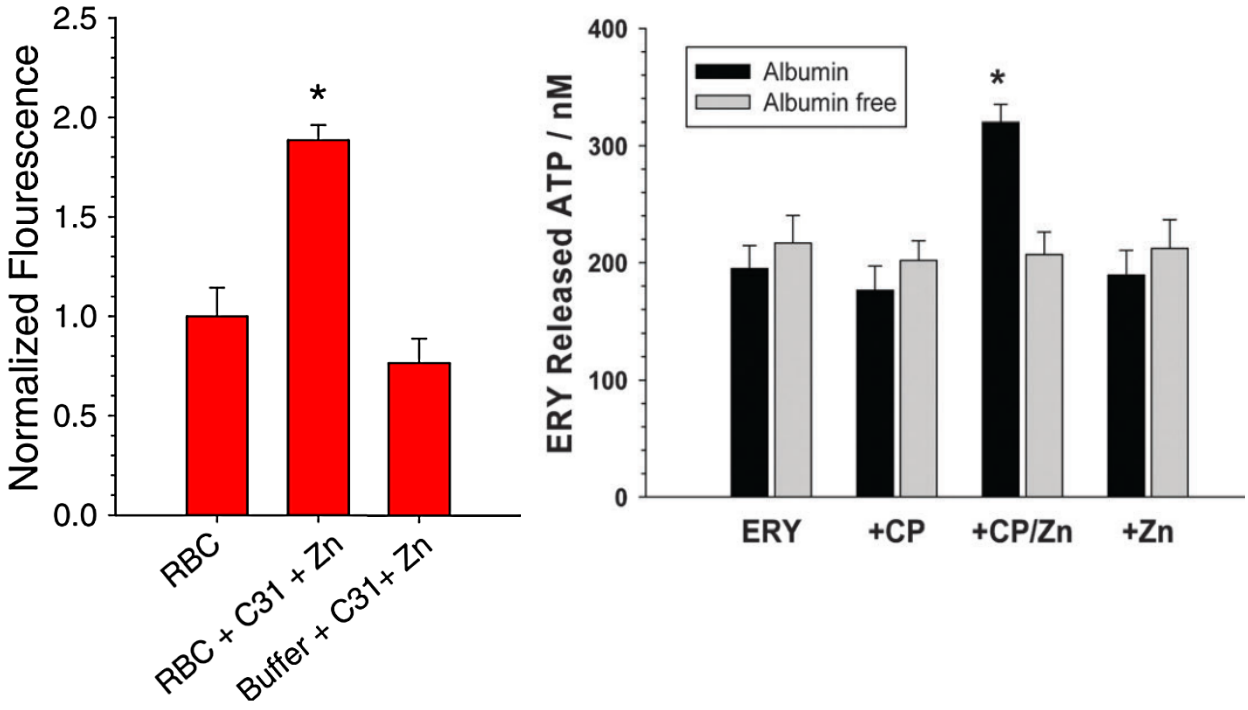

Figure 2.5: (Left) Relative fluorescent signals relating to the nitric oxide production from endothelial cells in a PDMS device with RBCs, RBCs plus C-peptide (C31) and zinc, and just buffer with C-peptide and zinc. (Right) Concentration of ATP released from RBCs under varying conditions of albumin, zinc, and C-peptide (CP).[15,38]

how C-peptide interacts with RBCs is required.

To investigate the role of C-peptide and Zn^{2+} in ATP release and NO production, binding experiments were performed. It was determined that C-peptide requires a metal, or more specifically zinc, to upregulate ATP from with RBCs.[17] Varying amounts of C-

peptide were added to a 7% suspension of RBCs to determine that there was an uptake of ~1800 C-peptide molecules per RBC. It was also found that RBCs do not specifically bind Zn^{2+} without the addition of C-peptide and that Zn^{2+} binding saturates in a 1:1 mole ratio with C-peptide (**Figure 2.6**).[17]

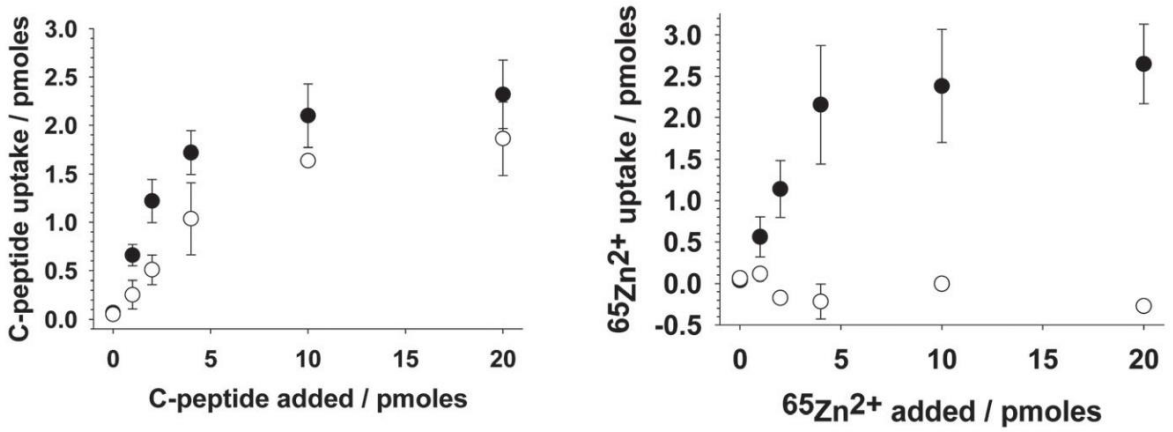

Figure 2.6: (Left) Binding curve of C-peptide and RBCs with zinc (filled circles) and without zinc (open circles). (Right) Binding curve of zinc with RBCs with C-peptide (filled circles) and without C-peptide (open circles).[15]

2.2 Motivation for This Work

The work mentioned above (**Figure 2.5**) was performed with the 3D printed flow device shown in F**igure 2.7**.[17] The device utilizes commercially available transwell inserts (polycarbonate membranes) to section off cells and samples wells from the flowing RBCs. This device was used to stimulate pancreatic β-cells, and the resulting C-peptide and zinc interacted with the RBCs, thus increasing ATP production, which diffused up to the endothelial cells to release NO. While this is a helpful system for exploring cell-to-cell communication, there are limitations. Specifically, this device allows the entirety of the

cell secretions to interact with all of the various cell types within the system, which leaves a few questions as to which cell secretions are stimulating the ATP release and subsequent NO production. In other words, one could still argue that insulin, or some other β-cell derived secretion, could be stimulating the effects measured from the RBC.

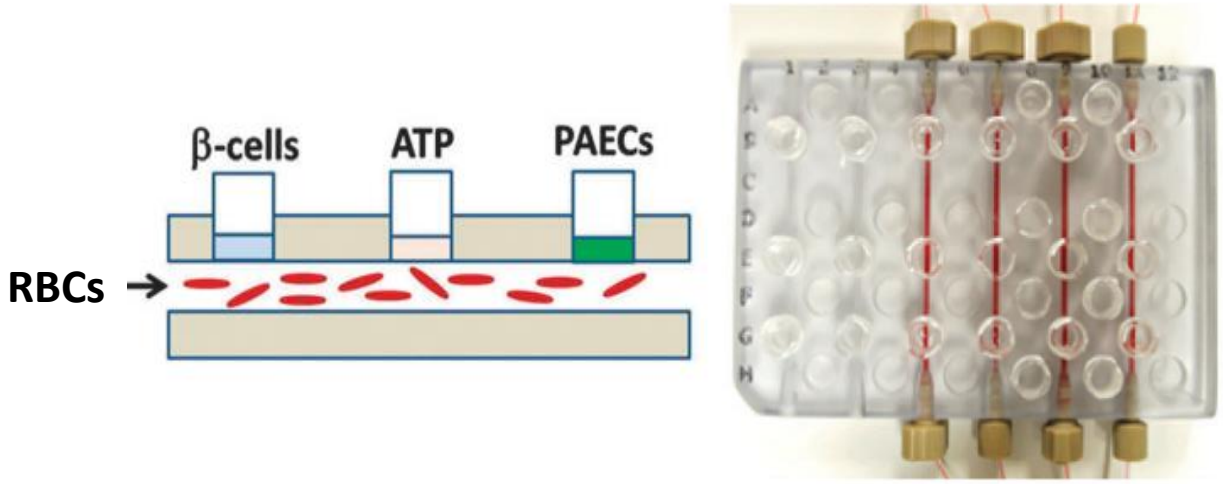

Figure 2.7: Cell to cell communication device to direct and indirect measurement of pancreatic β-cells effect on red blood cells. This device utilizes membranes in order to section of pancreatic β- cells and endothelial cells (PAECs) from flowing red blood cells mimicking the communication between the pancreas, RBCs, and blood vasculature.[15]

Therefore, additional approaches are required to confirm that C-peptide and Zn^{2+} secretions are the major stimuli for the RBC-derived ATP release.

To isolate various cell signaling pathways, researchers often develop knockdown/knockout versions of various cell lines. For example, if a specific protein is suspected in a particular cellular pathway, one can simply knockdown the protein expression through genetic engineering of the cell. For work related to the effects of Zn^{2+} and C-peptide on the body, a ZnT-8 knockdown of the rat INS-1 cell line was developed. The objective was to reduce the amount of Zn^{2+} entering the INS-1 cells. Upon secretion, C-peptide would not be able to stimulate ATP release because of the lack of Zn^{2+} secreted

from the same cells. However, the modification of the ZnT-8 transporter also down regulated C-peptide and insulin production, thus the ability to differentiate the importance of each species involved in the activation of C-peptide would be difficult and studying zinc and C-peptide independently utilizing this method will not work.

It is the goal of the work presented in the rest of this chapter to develop an improved platform for isolating the effects of various molecule and ion secretions from the INS-1 cell line. To accomplish this goal, we developed 3D printing techniques and tools to answer more complex questions about diabetic complications and develop a more robust cell-to-cell communication model. Such a system would be able to selectively capture the cell secretions one at a time, thus isolating various portions of the cell signaling mechanism to better understand the entire system. Importantly, unlike knockdowns, we are not manipulating the cells of interest (the INS-1 cells). Rather, the secreted molecules and ions are captured prior to interacting with the RBCs.

Figure 2.8 illustrates a new platform for selective cell-to-cell communication modified from a version of the device shown in **Figure 2.7** that could lead to answers. The cell systems (cells grown on wells or cells flowing in the channel) are separated by membranes and an additional sample reservoir. The membranes prevent bulk transport of the cells, while simultaneously separating magnetic beads from the cells. These magnetic beads can be modified with antibodies or chelating compounds to selectively pull out peptides, proteins, hormones, or metal ions. With this platform, beads could be loaded into both reservoirs, neither reservoir, or either reservoir with any combination of modified beads enabling selective control of areas of access for multiple analytes within the device.

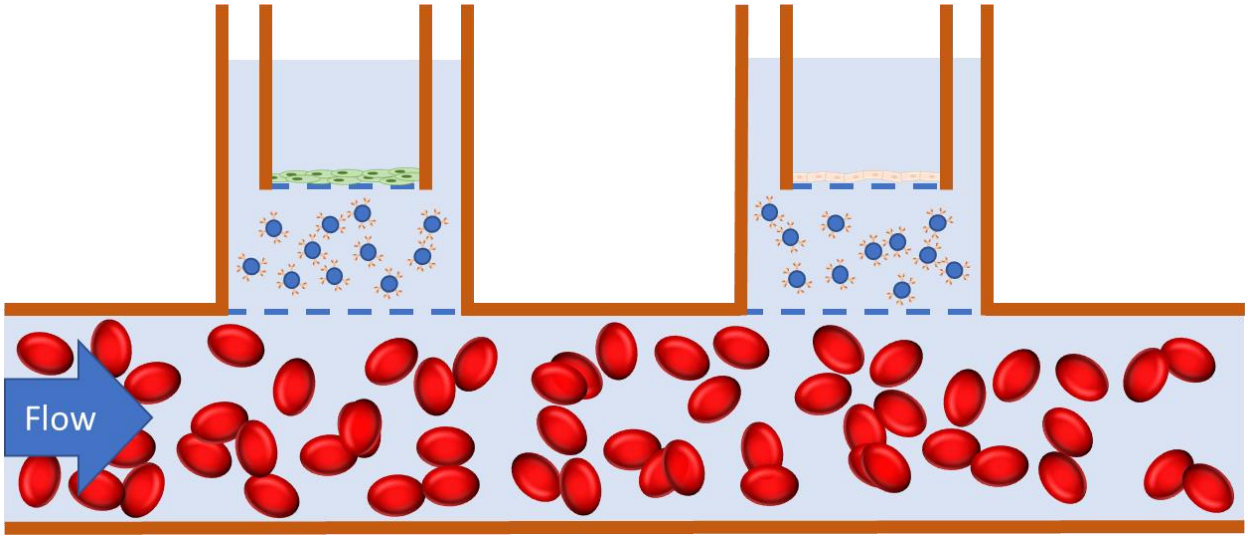

Figure 2.8: Concept for a new platform for cell-to-cell communication. Cells can be grown to confluency above the membranes or suspended in the reservoir above the membrane. Additional cell lines could be flowed in the channel sectioned off by another membrane system. Between the two membrane layers, modified beads large enough not to traverse the membrane can be used to selectively pull out various cell secretions.

2.3 Methods

2.3.1 INS1 Cell Culture

Rat INS1 cells were obtained from Dr. Karl Olsen's group at Michigan State University. Cells were cultured in either T75 culture flasks or 12-well flat bottom cell culture plates. Cell were grown in a 5% CO_2 incubator at 37°C using a modified RPMI-1640 medium according to **Table 2.1**. The cells were allowed to grow to confluence, usually for 10 to 14 days, changing the media every 48 hours. Once confluence was reached, the cells were stimulated or split to be regrown for later use. A 0.25% trypsin-EDTA (1X) (Gibco, Dublin, Ireland) solution was introduced to the cells for 5 minutes to detach the cells from the flask. The cells were resuspended in the growth medium then centrifuged at 1500g for 5 minutes. The pelleted cells were resuspended in the growth

media and counted by hemocytometer (Reichert, Buffalo, NY). The cell density was diluted as needed.

RPMI1640- (-) glutamine	**1L**
Penicillin	100 U/mL
Streptomycin	100 µg/mL
β-mercaptoethanol	55 µM
Fetal Bovine Serum	10%
L-glutamine	2 mM
HEPES	10 mM
Sodium Pyruvate	1 mM

Table 2.1: Components and concentrations for modified RPMI-1640 for INS1 cell growth

2.3.2 INS1 Cell Stimulation

The INS1 cells were stimulated to produce C-peptide with a low glucose storage media that was prepared in the same way as the growth media in **Table 2.1,** except RPMI1640 without glutamine and without glucose was purchased. However, the glucose was added in later to bring the concentration to 4.0 mM. A stimulation buffer was prepared according to **Table 2.2**. All components, except the glucose and bovine serum albumin (BSA), were dissolved in 18 MΩ water and warmed to 37°C. The solution pH was adjusted to 7.4 with dilute HCl or NaOH, as needed. The glucose and BSA were added to the prewarmed solution and allowed to dissolve in a CO_2 incubator at 37°C. Cells to be used for C-peptide secretion were washed three times with low glucose RPMI, then stored in the media for 12 hours. The cells were then washed three times with the stimulation buffer, and then 9 mL of the stimulation buffer were left on the cells for 4 hours.

NaCl	120 mM
KCl	2.4 mM
KH_2PO_4	1.2 mM
$MgSO_4 \cdot 7H_2O$	1.1 mM
CaCl2	2.5 mM
HEPES	10 mM
$NaHCO_3$	25 mM
BSA	0.1%
Glucose	16.7 mM
pH	7.4

Table 2.2: Components and concentrations for INS1 cell stimulation buffer

2.3.3 3D Printed Holder for Membrane Modification

A device to hold the membrane for modification was 3D printed in VeroWhite based on dimensions taken from a device machined out of Teflon used by Merlin Bruening's research group. **Figure 2.9** shows the dimensions of the 3D printed version. Membranes were cut to 15 mm using a 15 mm hole punch, then the membrane and a 15 mm Viton O-ring are sandwiched between the top piece and the bottom piece. Solution was loaded into the top well, which can hold 10 mL at one time. Solution was pulled through the membrane by a piece of HPLC tubing threaded into the device with commercial fitting (P-202X male nut 1/16 in, IDEX). The HPLC tubing was then connected to a PVC tubing on a peristaltic pump.

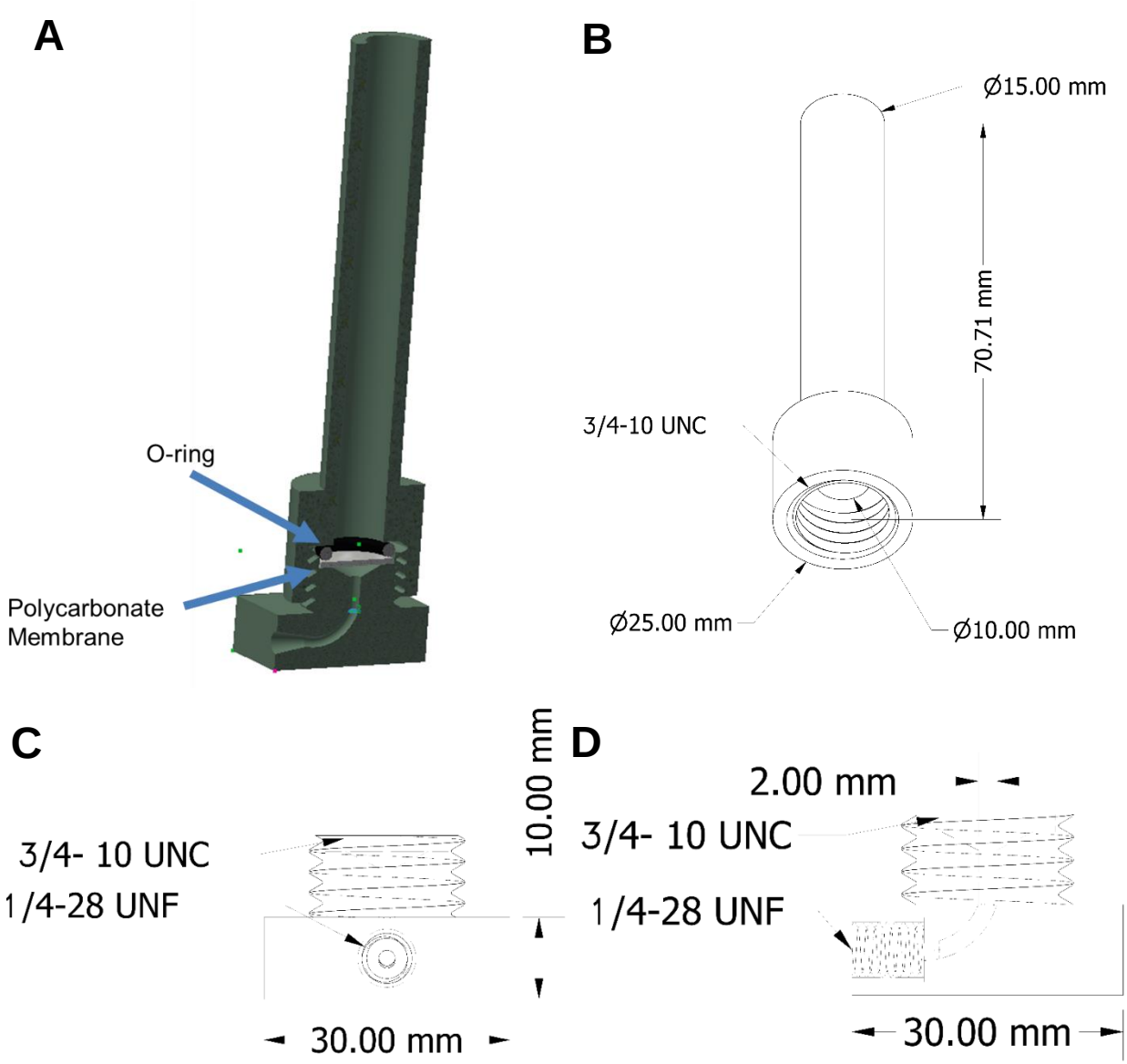

Figure 2.9: CAD representation of the 3D printed holder for membrane modification. (A) is the rendered image with the membrane and the commercially available 15 mm Viton O-ring in place. (B-D) show the dimensions of each piece.

2.3.4 Membrane Modification for Zn^{2+} Capture

Poly(N,N-dicarboxymethylallylamine) (PDCMAA) was obtained from the Bruening group to be used as a metal chelator. The PDCMAA was dissolved in 0.5 M NaCl such that the monomeric concentration is 0.01 M. The pH of the solution was increased (pH ~11) to fully dissolve the solution then the solution was filtered to remove any undissolved

particles or polymer aggregates. The pH was adjusted to pH 3 with the addition of dilute HCl. The membrane was washed with 18 MΩ water for 10 min at a flow rate of 1 mL/min using a peristaltic pump. Next, 10 mL of the 0.01 M PDCMAA solution were circulated through the membrane for 30 minutes. The membrane was then washed with 10 mL of DI water. The membrane was removed and placed into a different 3D printed holder that had not been exposed to the PDCMAA.

2.3.5 EDTA Coated Magnetic Beads

BcMag EDTA coated beads were purchased from Bioclone, Inc. These beads were washed with 18 MΩ water 3 times and then washed with the INS1 stimulation buffer three times. The beads were resuspended based on mass.

2.3.6 Anti-C-peptide Magnetic Beads

Dynabeads MyOne Carboxylic Acid magnetic beads were purchased from ThermoFisher Scientific. The beads were washed three times with 20 mM phosphate buffer containing 150 mM NaCl at pH 4.5. The solution was decanted from the beads and a 500 µL aliquot containing 0.4 mg/mL of anti-C-peptide was added for each 10 mg of beads. This solution was allowed to incubate for 30 minutes. 15 mM 1-Ethyl-3-(3-dimethylaminpropyl) carbodiimide HCl (EDC) was prepared in 20 mM phosphate buffer with 150 mM NaCl at pH 4.5. 1 mL of EDC solution was added to the beads and they were refrigerated overnight. The following day, the beads were washed three times with the stimulation buffer mentioned in section 2.3.2 and then resuspended such that the bead density was 2 mg/mL.

2.3.7 Selective Cell-to-Cell Communication Flow Device

A custom multi-well blood flow device was printed on a Stratasys J750 PolyJet printer, utilizing its multi-material printing capabilities. The flow device was designed to incorporate two nested, custom-made 3D printed membrane inserts. An expanded and assembled CAD representation of the device can be seen in **Figures 2.10** and **2.11** respectively. **Figure 2.12** shows the annotated dimension of the base of the device, while, **Figure 2.13** shows the annotated dimensions of the insert components. The flow device was printed in VeroClear for a transparent model, and flow characteristics could be observed. Within the device wells, directly above the channel, three layers of Agilus30, Stratasys' synthetic rubber, were laid down in order to provide a sealing surface for the first membrane. The membranes used were 0.45 µm Polyethersulfone (PES) purchased from Sterlitech (Kent, WA). The membranes were cut in an octagon shape using an H-Series 5th Gen CO_2 Desktop Laser cutter (Full Spectrum Laser, Las Vegas, NV) available at the MSU library (Power=22%, Speed=100%). An octagon membrane compression ring with 10 mm inside diameter was used to compress the membrane to the bottom of the flow device wells. On top of the octagon-shaped holder, a threaded insert was screwed into the flow device to apply permanent pressure to the membrane, ensuring a good seal. This threaded insert was printed using the Vero line of materials with a thin layer (0.1 mm) of Agilus30 on the bottom to seal to the octagon piece. Within the threaded insert, there was a groove for the second insert to rest. For the second insert, the printer was set to print without the use of support material via accessing the Stratasys Parameters Manager page on the computer embedded within the printer. Here, the following parameters were changed from their previous values to zero millimeters: Carpet_height,

Carpet_protectorZ, and ImproveSupport_thickOfPedestal. Utilizing these settings, 0.1 mm of the second insert was printed, then the printer was paused while the membrane was placed into the device before the print job was resumed. Parts printed with support material were cleaned with a high-pressure water jet system (Powerblast, Balco, UK) and soaked in a 2% sodium hydroxide solution until clean.

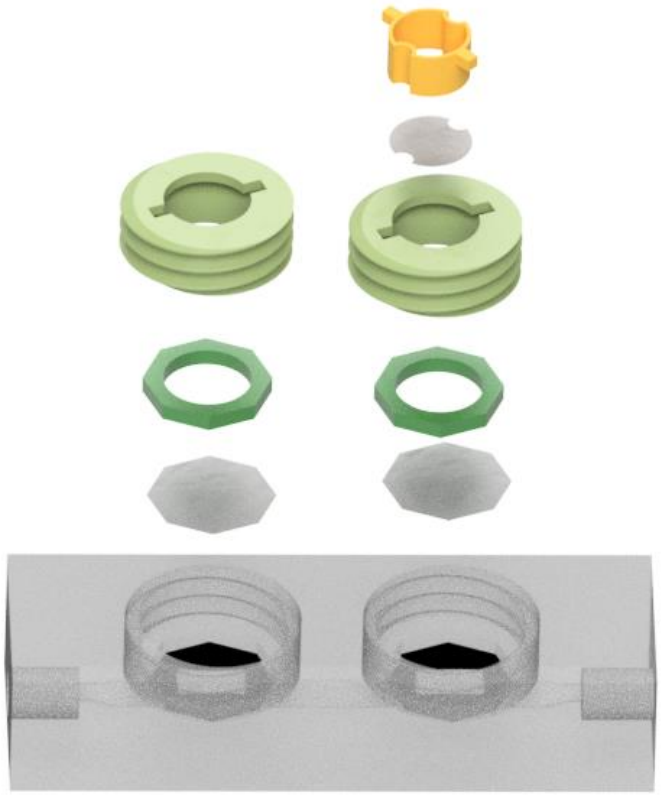

Figure 2.10: CAD representation of the components used in the flow device. Moving from top to bottom the components are: cell insert, membrane, threaded insert, octagon membrane holder, membrane, flow device. All pieces except the PES membranes were 3D printed on a Stratasys J750.

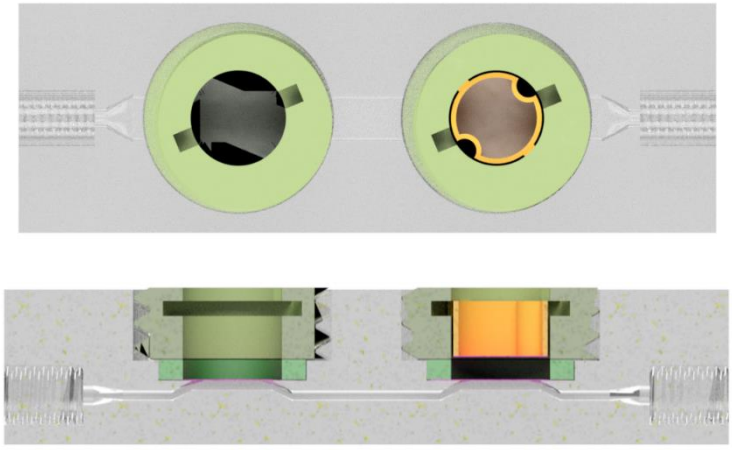

Figure 2.11: CAD representation of the assembled flow device (top) and a cut view of the assembled flow.

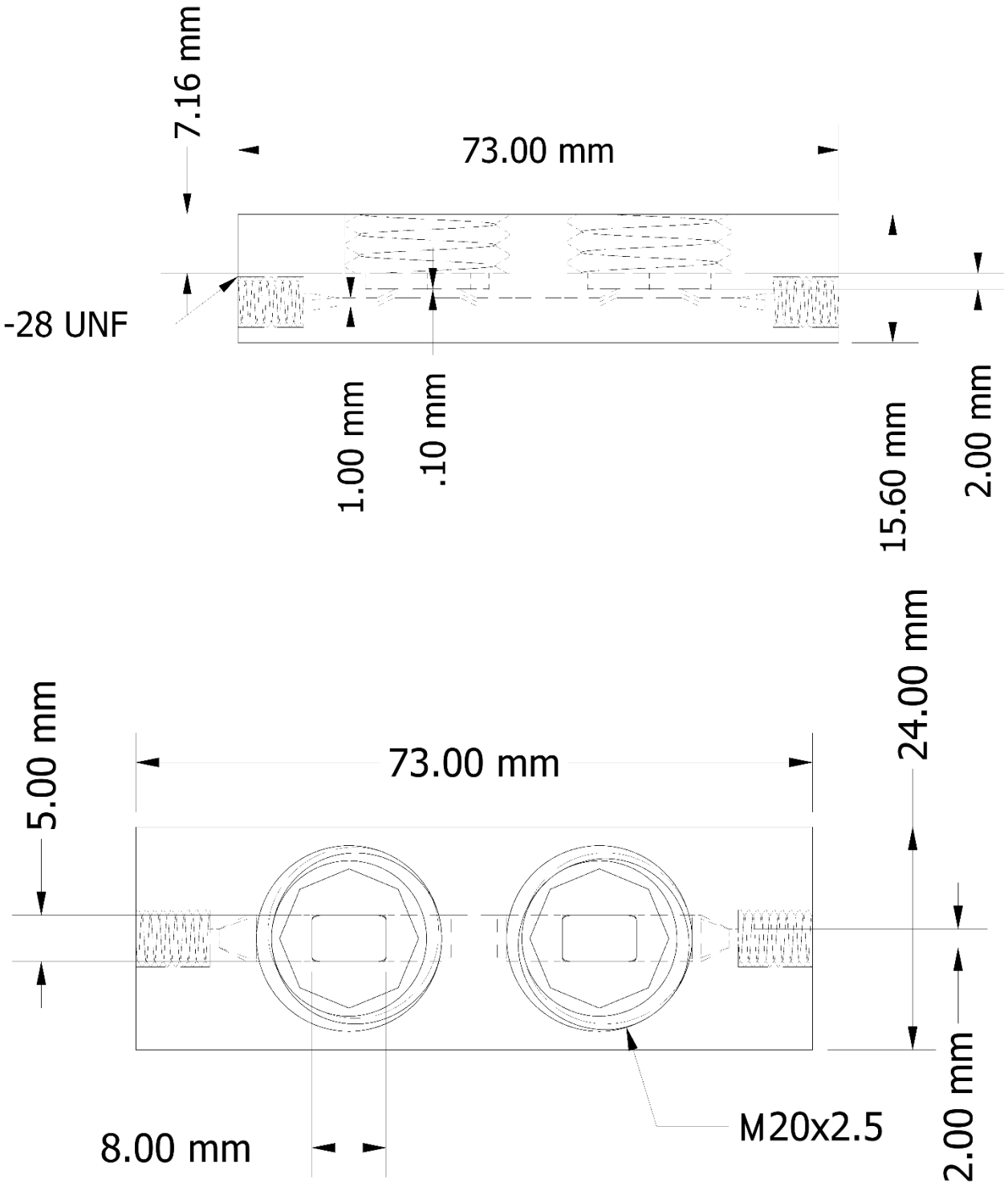

Figure 2.12: Annotated dimensions for the cell to cell communication flow device. This device is made to hold up to 4 inserts, two per well. Peristaltic pump tubing is connected to the device with commercial HPLC fittings P-202X

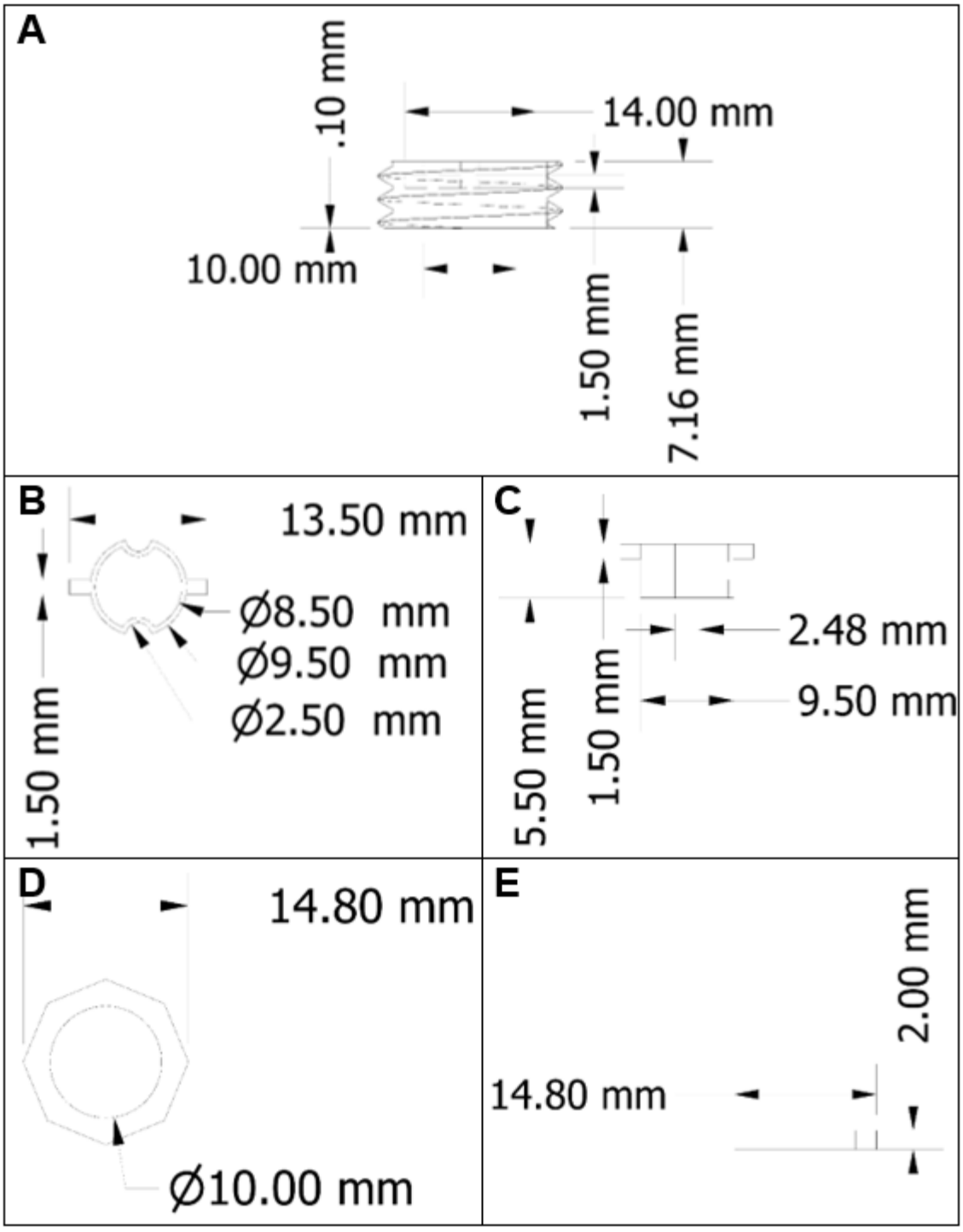

Figure 2.13: Annotated dimensions for the various components for the flow device. (A) Threaded insert. (B- C) Cell insert. (D-E) octagon membrane compression ring.

2.3.8 Flow Device Characterization

Adenosine triphosphate (ATP) (Sigma, St. Louis, MO) was dissolved in a physiological salt solution (PSS) with the composition shown in **Table 2.3**. A stock was diluted with the PSS to make standards ranging from 0 to 800 nM ATP. Approximately 750 µL of PSS were then loaded in to the channels of the device using a peristaltic pump (IDEX Corporation, Lake Forest, Il) at a flow rate of 200 µL/min. Once the channel was fully loaded, the inlet tubing was connected to outlet tubing on the device, thereby closing the system. After the system was closed off, 300 µL of each standard were loaded into well A and 300 µL of PSS were loaded into well B. Solution was pumped from well A to well B. The device was covered with a plate printed in Agilus30 to seal the top of the wells and prevent evaporation. The entire device and pump was place in a humidified oven at 37°C and circulated for 2 hours at a flow rate of 200 µL/min.

Potassium Chloride	4.7 mM
Calcium Chloride	2.0 mM
Sodium Chloride	140.5 mM
Magnesium Sulfate	12 mM
Tris(hydroxymethyl) aminomethane	21.0 mM
Dextrose	5.5
Bovine Serum Albumin	0.5 %
pH	7.4

Table 2.3: Composition and concentration of PSS components.

2.3.9 ATP Measurements

The firefly luciferase assay was used for ATP determination. Potassium luciferin (Goldbio, St. Louis, MO) solution was made in albumin-free PSS to a concentration of 2

mg/mL. Five mL of the potassium luciferin solution were added to 100 mg of firefly lantern extract (Sigma, St. Louis, MO). This solution was then diluted 1:10 in albumin-free PSS. A FlexStation 3 Multi-Mode Microplate Reader (Molecular Devices, San Jose, CA) was utilized for ATP measurements. Using the plate reader, 50 µL of the luciferin solution were added to 100 µL of sample and immediately read for 500 ms per sample.

2.3.10 Preparation of Red Blood Cells

Whole blood was collected either in heparin tubes (if the blood was to be used on the same day as the draw) or citrate tubes (if used at a later date; refrigerated citrate tubes could be used up to 48 hours later). The blood was centrifuged at 500g for 10 minutes. The plasma and buffy coat were removed, and the packed RBCs were transferred to a 15 mL centrifuge tube. Fresh PSS, made as described above, was added to the RBCs and mixed by inverting several times. The cells were washed in this manner three times, removing the PSS and adding fresh aliquots each time. After the final wash, the PSS was removed, and the hematocrit was measured using a hematocrit centrifuge (StatSpin CritSpin, Beckman Coulter, Brea, CA). Typically, this was around 70%. The cells were then diluted to a 7% hematocrit for experiments.

2.3.11 ATP Release from Flowing RBCs

The channels of the device were loaded with ~750 µL of 7% RBCs. After the channels were loaded, a 100 nM Zn^{2+} and 100 nM C-peptide solution was prepared in PSS by first preparing an 800 nM Zn^{2+}/C-peptide solution in water and then diluting this mixture with PSS. 300 µL of the Zn^{2+}/C-peptide solution were loaded into well A, and 300 µL of fresh PSS were loaded in to well B. The device was covered and placed inside the humidified oven at 37°C and allowed to pump at 0.5 mL/min for 3 hours

2.4 Results

2.4.1 Membrane Zinc Capture

Five, 15 mm diameter polycarbonate membranes (0.4 µm pores) were modified as described above. 500 µL aliquots of 15 nM $ZnCl_2$ in 20 mM phosphate buffer with 150 mM NaCl (pH=7.4) were pumped through either the empty device, polycarbonate membrane, or the PDCMAA modified PC membrane. Results showed significant nonspecific binding to the device, but there was a statistical increase in the amount captured by the modified membrane (**Fig 2.14**). 1 mL of the Zn^{2+} solution was able to be flowed through the device before all the available sites on the membrane were saturated. This equates to 8.1 ± 1.8 picomoles of Zn^{2+} bound. However, when the solution was switched to the stimulation buffer listed previously described, the capture efficiency dropped to 2.93 ± 0.13 picomoles. Assuming the cells release Zn^{2+} in equimolar concentrations, the cells would be seeded in such a way as to release enough Zn^{2+} such that the concentration was 40 nM in 300 µL of solution, which equates to 12 picomoles of Zn^{2+}secreted. This means that this membrane system does not have the capture efficiency required for these experiments.

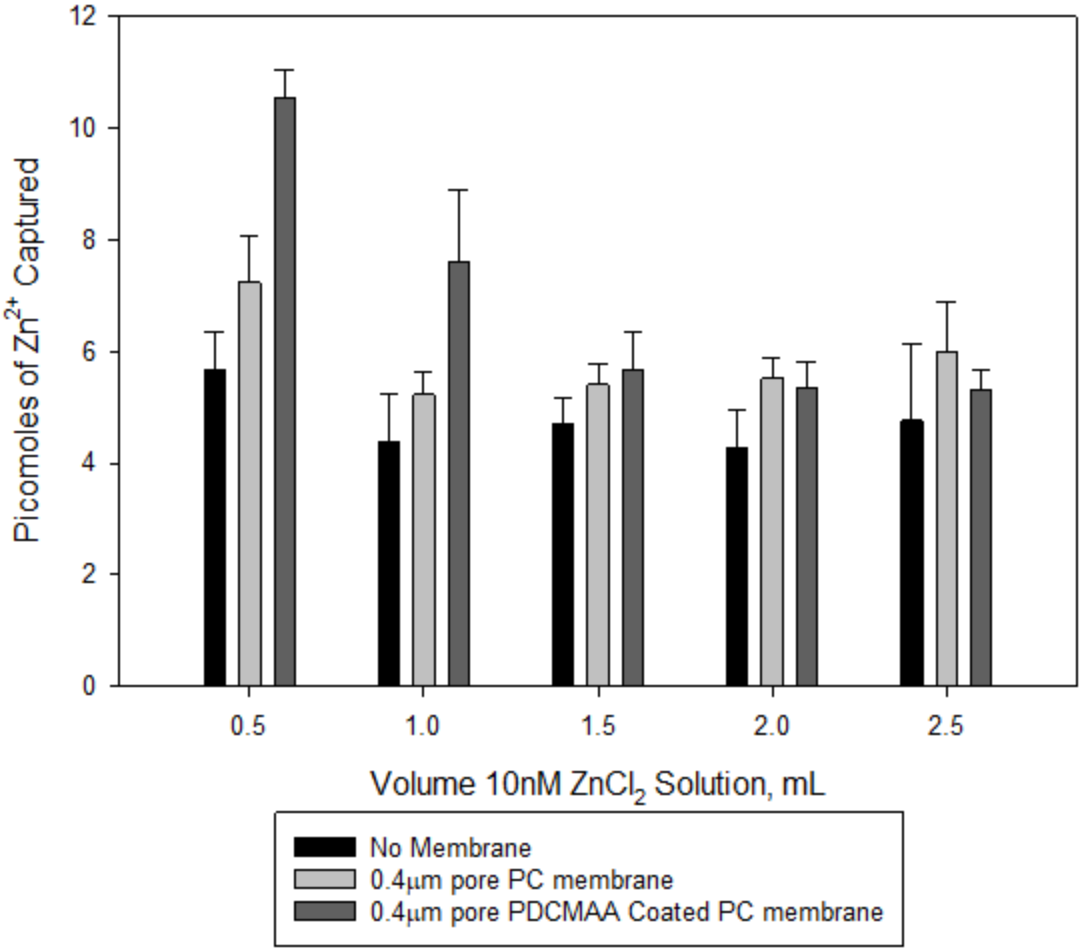

Figure 2.14: When 500 µL aliquots of 15 nM $ZnCl_2$ were flowed through the membrane system, unmodified PC membrane, and PDCMAA coated PC membrane 8.1 ± 1.8 picomoles of Zinc was captured before the sites on the membrane were saturated.

2.4.2 Zinc Capture by Magnetic Beads

The membranes could not capture enough Zn^{2+} with the dimensions used and making the device larger is not desirable, so commercially available EDTA coated beads were explored. For this experiment, radioactive $^{65}Zn^{2+}$ was spiked into the stimulation buffer at a concentration of 47.5 nM. The concentration of the Zn^{2+} remaining in solution was quantified at 3, 7, 15, 30, 45, and 60 min (**Fig 2.15**). After 15 minutes the beads are fully saturated, equating to 22.7 ± 2.0 picomoles of capture for 7.9 mg of beads after subtracting possible adsorption onto the walls of the 1.7 mL centrifuge tube. Under these conditions, 7.9 mg of beads would capture all of the secreted Zn^{2+}.

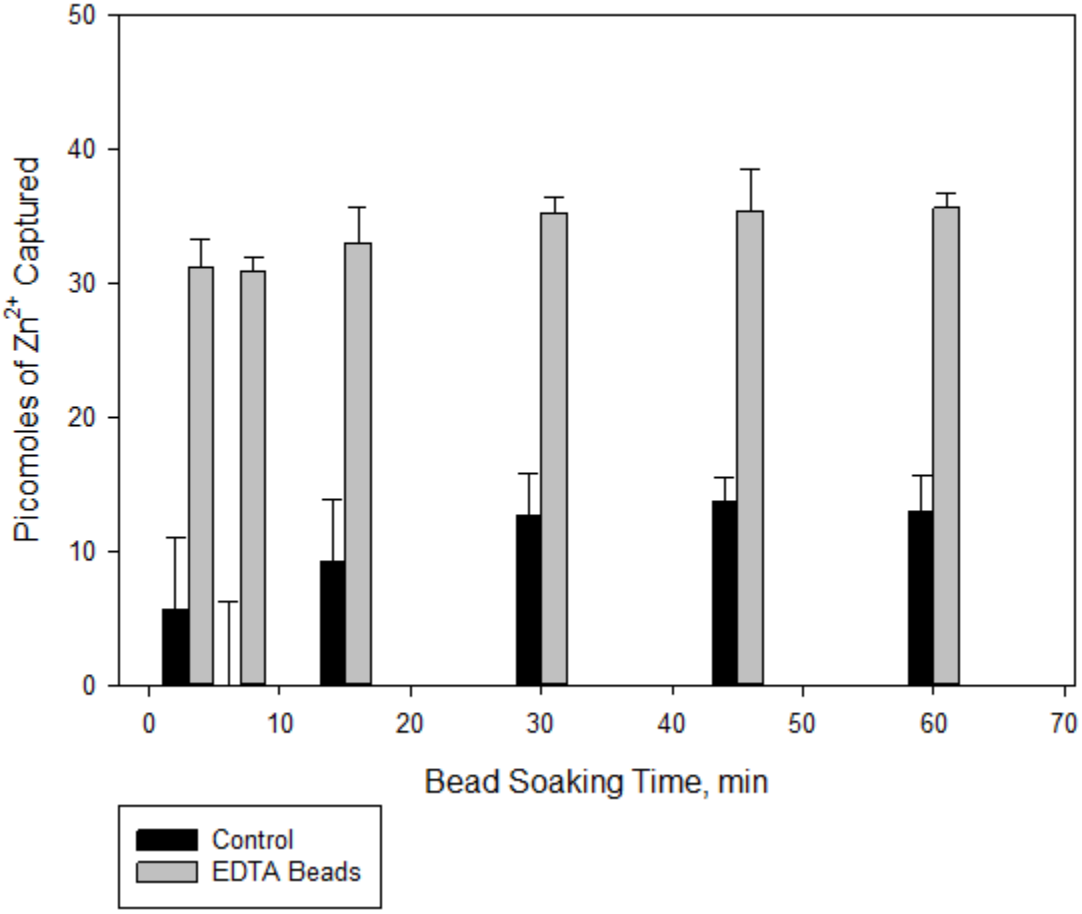

Figure 2.15: Commercially available EDTA coated magnetic beads were used to pull radioactive $^{65}Zn^{2+}$ from the INS1 stimulation buffer. This plot shows that after 10 minutes of incubation with the beads at room temperature, the beads have been saturated. The saturation point under these conditions is at 2.88 ± 0.26 picomoles of zinc per mg of beads.

2.4.3 C-peptide Capture by Magnetic Beads

C-peptide secreted from rat INS1 cells was directly captured by anti-C-peptide coated beads (**Fig 2.16**). The cells were grown in a 12-well cell culture plate and allowed to grow to confluence. The stimulation solution was prepared as described previously, with the exception of the addition of anti-C-peptide coated beads at a concentration 2 mg/ mL. Next, 1 mL of stimulation solution was added to 3 wells of cells and 1 mL of stimulation solution with beads was added to 3 different wells. The cells were allowed to incubate at 37°C in a CO_2 incubator for 3 hours.

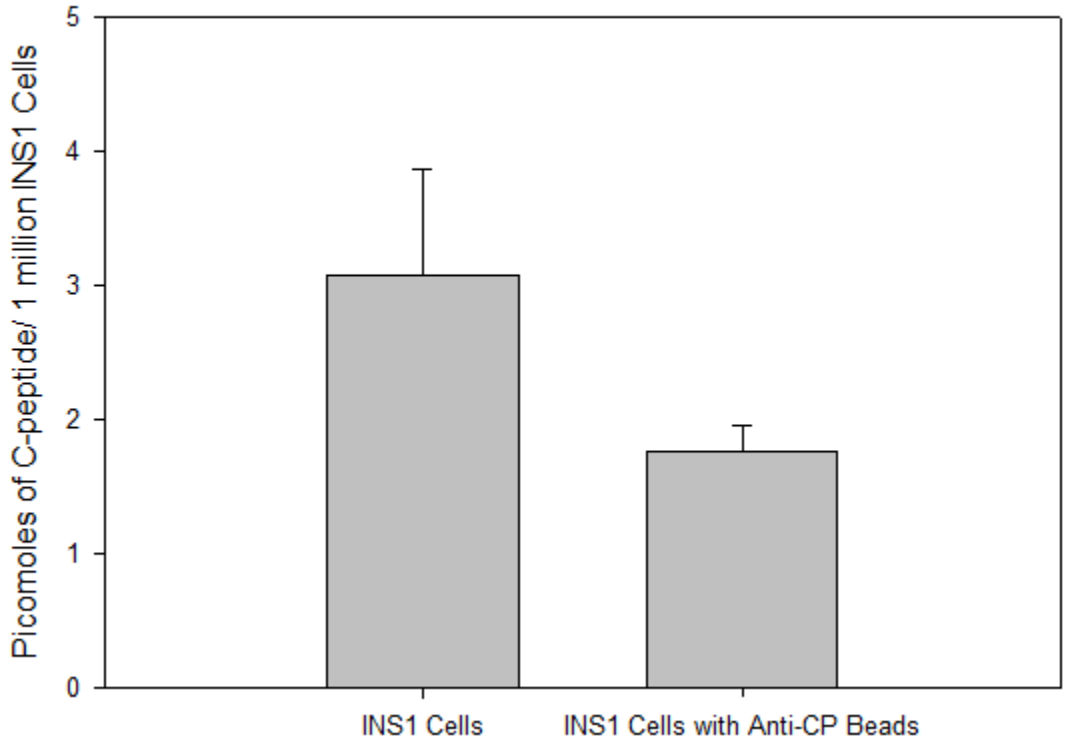

Figure 2.16: Commercially available carboxylic acid coated magnetic beads were modified with anti-C-peptide and used to capture C-peptide during the stimulation of INS1 cells. Under these conditions the beads were saturated at 0.65 ± 0.40 picomoles of C-peptide per mg of bead. $p< 0.05$, n=3, error= s.d.

After incubation, the stimulation buffer was removed. The cells were detached from the bottom of the wells with 0.25% trypsin-EDTA and counted by a hemocytometer (Reicher, Buffalo, NY). The concentration of C-peptide was quantified by an ELISA kit (Millipore Sigma, Burlington, MA) and normalized to the number of cells. For 2 mg of anti-C-peptide coated beads, 1.3 ± 0.8 picomoles was captured. This could easily be scaled up for the flow device to include more beads to capture more of the secreted C-peptide.

2.4.4 Characterization of Flow Device

First, the device was characterized by flowing standards through the channels of 2 different 6 channel devices. Standards from 0 - 527 nM ATP were prepared in PSS as described above. These standards were first run on the FlexStation3 plate reader (**Fig 2.17**). After confirming a linear response for the range in question, the standards were flowed through the device. Standards were loaded into the channels (~750 µL) as described previously. Then, 300 µL of PSS were placed into the wells above the channel. The entire device and pump was placed into the 37°C oven and allowed to circulate at 0.5 mL/min for 2 hours. After the 2-hour period, the samples within the wells were analyzed using the FlexStation3 Plate reader. A plot of concentration added to the channels vs the counts for the wells was plotted (**Fig 2.18**). Both devices showed a similar response. Device 1 had a slope and intercept of 0.26 ± 0.11 and 6.1 ± 2.7, while device 2 had a slope and intercept of 0.26 ± 0.12 and 1.2 ± 3.0. This indicates that the 12 channels used perform in similar manners.

Finally, the concentration of ATP in the channel was quantified. The concentration in the channel vs the concentration in the well was plotted to determine if equilibrium was reached (**Fig 2.19**). The equations for the linear fit for device 1 and device 2 were y =

0.847(±0.005)x + 2.5(±0.4) and y = 0.884(±0.012)x + 3.2(±1.12) respectively. Since the slope is not equale to 1 this reveals that the ATP concentration did not reach equilibrium in the two-hour period.

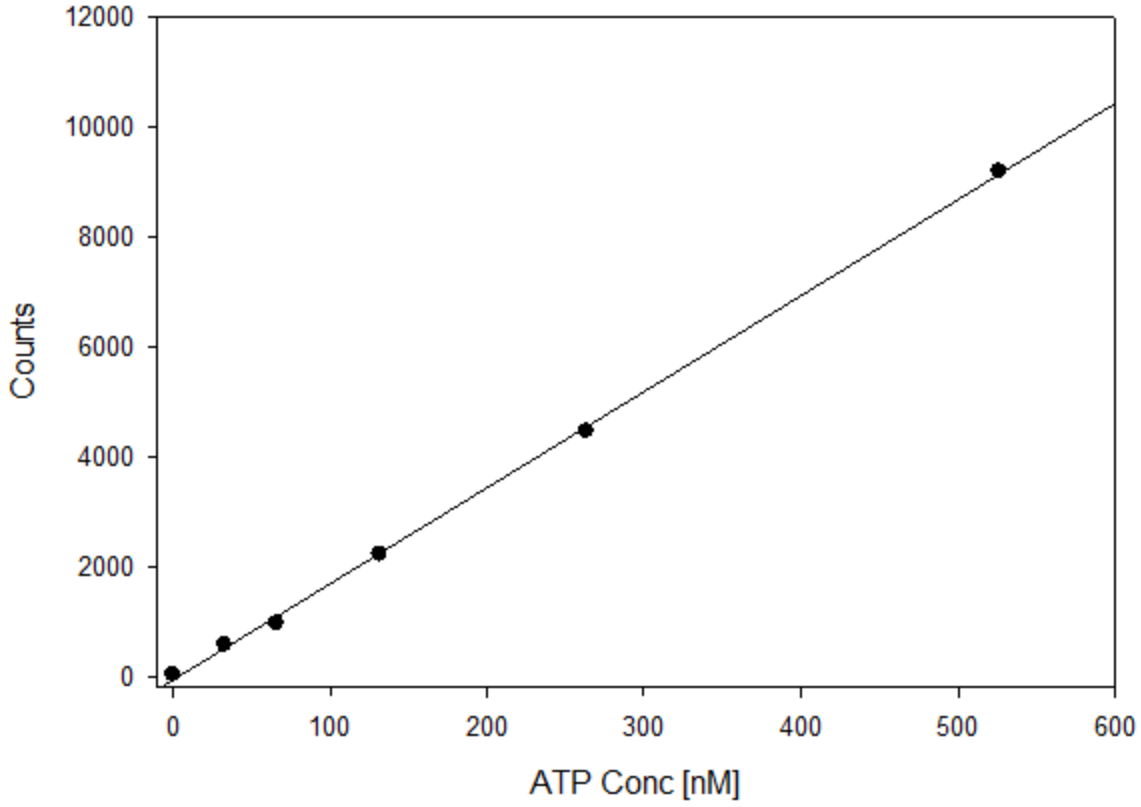

Figure 2.17: ATP calibration curve utilizing the Luciferin Luciferase Assay. y = 17.5(±0.2) x - 69.4(±55.1) R^2=0.9994

Next, the diffusion of C-peptide from the well to the channel was quantified. For this experiment, a 40 nM solution of FITC-C-peptide in PSS was prepared. 300 µL of the FITC-C-peptide was loaded into well A and the concentration of the C-peptide was measured at 10, 30, 60, and 120 minutes. **Figure 2.20** shows these results. After a two-hour period, the concentration with in the channel was up to 3.09 ± 0.18 nM, if this system had reached equilibrium the concentration would have plateaued at 8.88 nM.

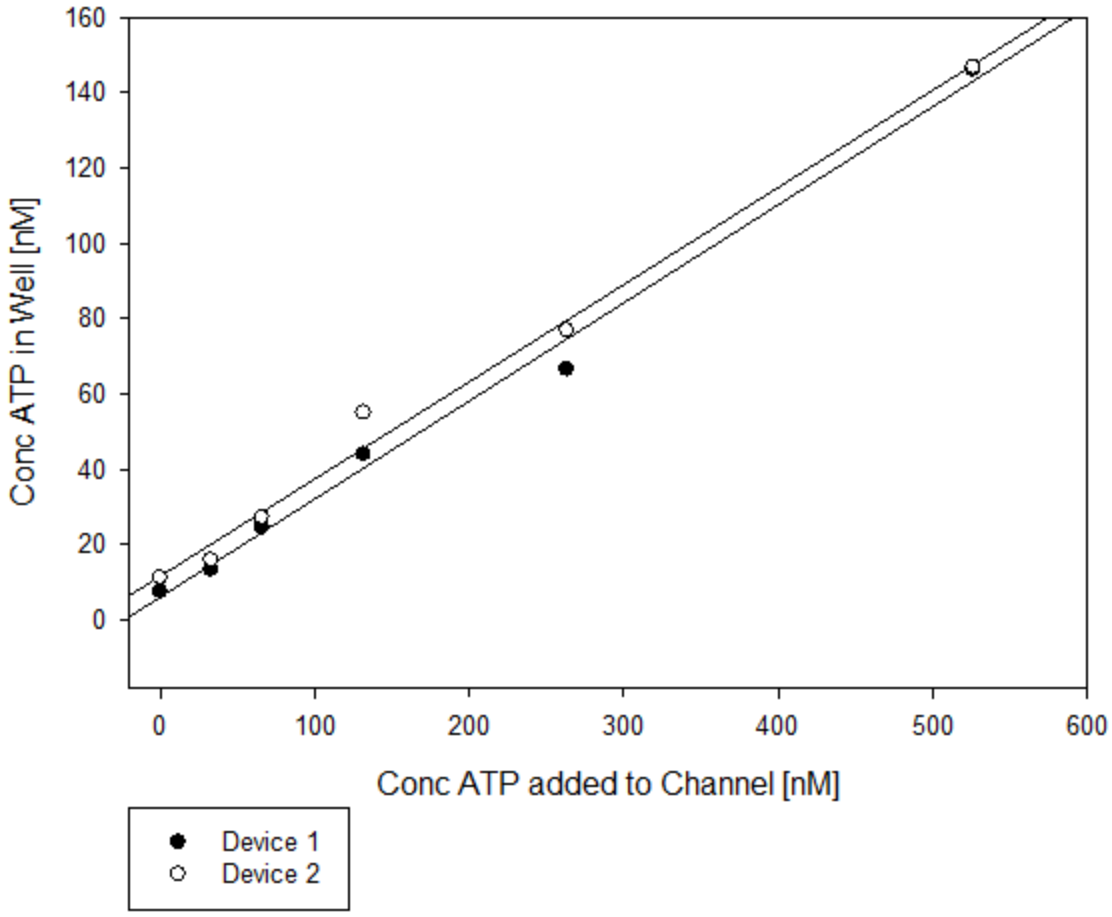

Figure 2.18: Plot of the measured concentration of ATP in the well as a function of the added concentration in the channel. Both devices showed a good correlation between the concentration added to the channel and what diffused into the well. Device 1 gave an R^2= 0.9932 and device 2 gave an R^2= 0.9912.

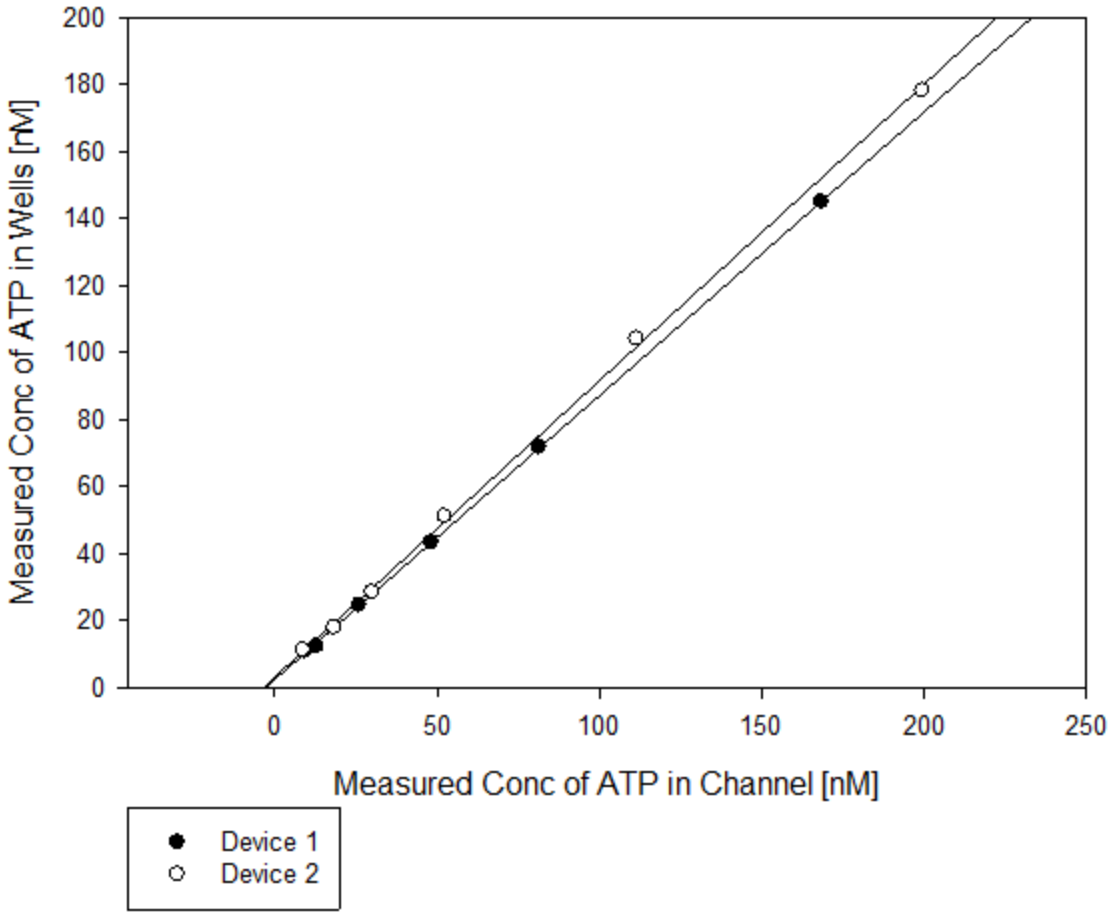

Figure 2.19: Plot of the measured concentration of ATP in the well as a function of the measured concentration of ATP in the channel after two hours of flow. The slopes of these two devices are (0.847 and 0.884) meaning that equilibrium was not reached in the two-hour window. If these samples were at equilibrium the slope would be 1.

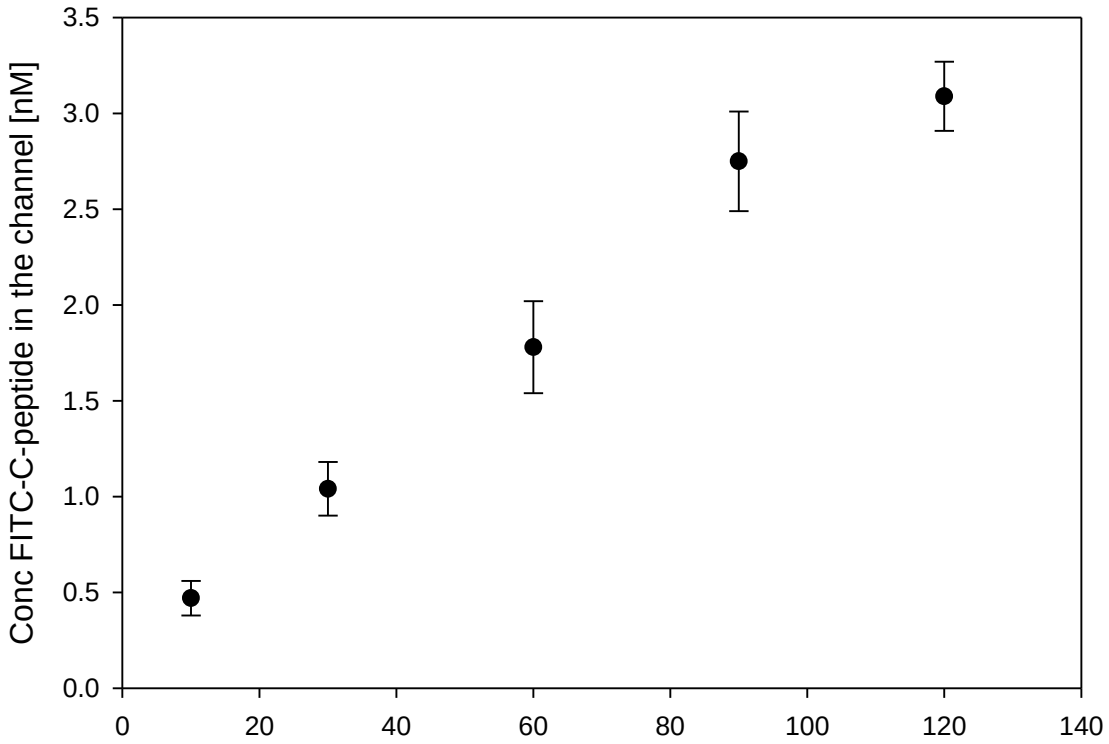

Figure 2.20: Plot of the concentration of C-peptide that transverse the membrane from the well to the channel as a function of time. This plot shows that after 2 hours the concentration of C-peptide in the channel was 3.09 ± 0.18 nM (n≥3). The data shown here did not reach equilibrium; the equilibrium concentration would be 8.88 nM.

2.4.5 ATP Release from Flowing RBCs

RBCs were collected and washed as described previously. The 7% RBC suspension was then loaded into the channels of the device a circulated for 3 hours. Results shown in **Figure 2.21** illustrate that a statistical difference was seen in the ATP signal within the wells, as expected: higher for the Zn/C-peptide treated cells (1691 ± 217, n=6) and lower for the non-treated control RBCs (1143 ± 101, n=6). However, there was no statistical difference between the channels. This could be due to the difference in the sample matrix or from the fact that the cells were centrifuged before analysis.

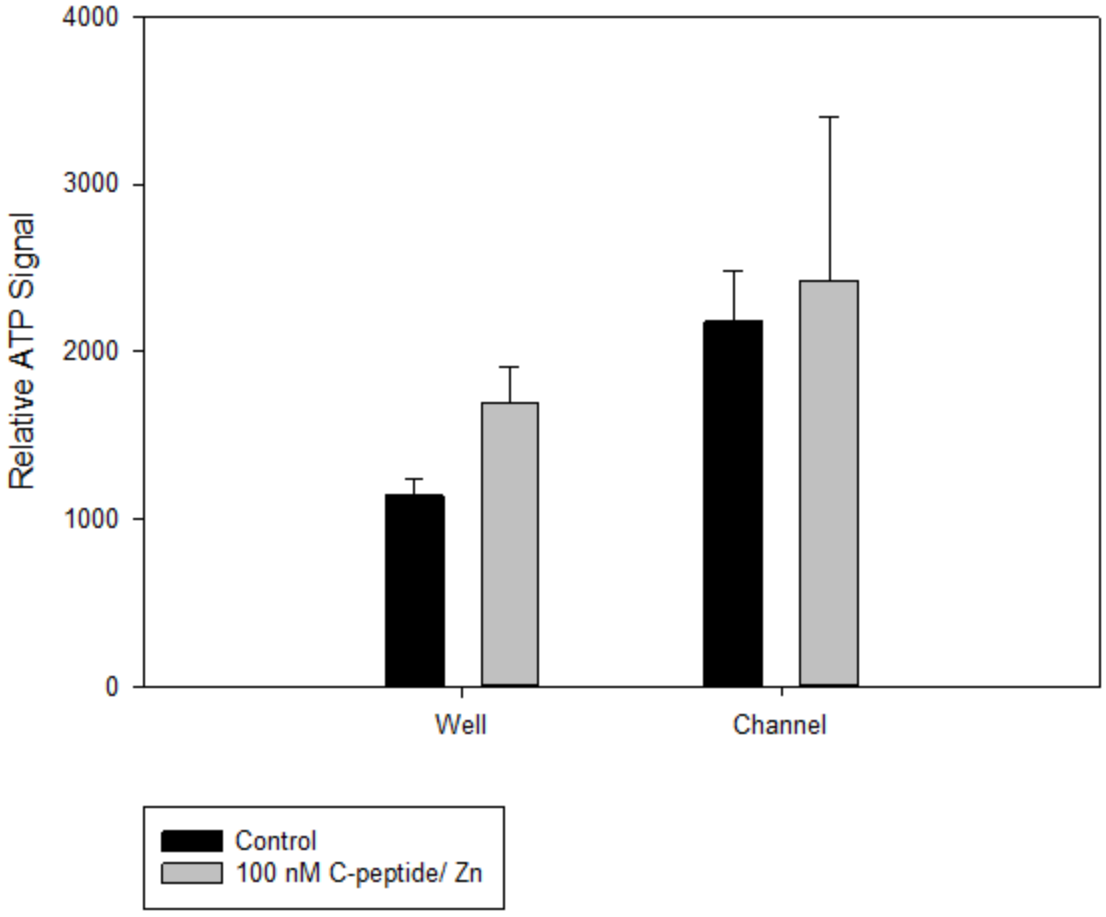

Figure 2.21: Relative ATP signal as measured in the wells and the channels when 100 nM Zn/C-peptide was placed in a well A and 7% RBCs were flowed in the channels. The ATP was determined and showed statistically higher signal in the well ($p<0.05$) when Zn/C-peptide was added to the system. However, a statistical difference was not seen in the channel. This could be due to the difference in the background matrix or the need to centrifuge the sample before the measurement is made.

2.5 Discussion

Herein, the components for making a flow device for selective cell-to-cell communication were discussed. It has been shown that both Zn^{2+} and C-peptide, secretions important to diabetic research, can be selectively captured in quantities appropriate for secretions from rat INS1 cells. While this cannot be easily accomplished at this time with modified membrane systems, it can be accomplished with commercially available magnetic beads. The magnetic beads can be purchased directly coated with EDTA for the Zn^{2+} capture, or carboxylic acid coated and derivatized with antibodies for C-peptide capture.

While the device as reported does not yield any novel findings, it does confirm that a device with fully customizable membrane inserts can function to give the same data as 3D printed devices with commercially available membrane inserts. The ability to utilize custom made inserts allows researchers to mimic more complex biological systems by layering and combining inserts in unique ways. By utilizing these segmented compartments new experiments can be run to selectively capture signaling molecules directly after secretion. Capturing the cell secretions at different location within the device allows for complete control over the system. While the device shown here only utilizes two wells and one set of nested inserts one could envision an entire array of nested inserts and many more wells to better mimic any number of cell-cell-cell communication networks.

Here has been reported a novel platform for cell-to-cell communication. While this device was fabricated for use in exploring signaling between cell lines important to diabetic complications, specifically red blood cells, pancreatic beta cells, and endothelial

cells, applications are not limited to this system. Future applications of this device could include other complex cell interactions, some of which may include bacterial infection and treatment with medications, medication metabolism and downstream metabolite interactions, and others. By utilizing the 3D printing technology discussed and the devices reported in this chapter, this platform could be easily transferred to numerous labs across the world for use in understanding complex cell interactions under any condition of interest.

REFERENCES

REFERENCES

(1) American Diabetes Association www.diabetes.org (accessed Jun 14, 2018).

(2) Centers for Disease Control and Prevention. National Diabetes Statistics Report , 2017 Estimates of Diabetes and Its Burden in the Epidemiologic Estimation Methods. US Dep. Heal. Hum. Serv. **2017**, No. Cdc, 2009–2012.

(3) Rahbar, S. The Discovery of Glycated Hemoglobin: A Major Event in the Study of Nonenzymatic Chemistry in Biological Systems. Ann. N. Y. Acad. Sci. **2005**, 1043, 9–19.

(4) Anguizola, J.; Matsuda, R.; Barnaby, O. S.; Hoy, K. S.; Wa, C.; DeBolt, E.; Koke, M.; Hage, D. S. Review: Glycation of Human Serum Albumin. Clin. Chim. Acta **2013**, 425, 64–76.

(5) Skyler, J. Diabetes Mellitus: Pathogenesis and Treatment Strategies. J. Med. Chem. **2004**, 47, 4113–4117.

(6) Hu, F. B. Globalization of Diabetes: The Role of Diet, Lifestyle, and Genes. Diabetes Care **2011**, 34 (6), 1249–1257.

(7) Association, A. D. Diagnosis and Classification of Diabetes Mellitus. Diabetes Care **2010**, 33 (SUPPL. 1), S62–S69.

(8) Michael J. Fowler, M. Microvascular and Macrovascular Complications of Diabetes. Clin. Diabetes **2008**, 26 (2), 77–82.

(9) Steffes, Mi.; Sibley, S.; Jackson, M.; Thomas, W. β-Cell Function and the Development of Diabetes-Related Complications in the Diabetes Control and Complications Trial. Diabetes Care **2003**, 26 (3), 832–836.

(10) Meyer, J. A.; Spence, D. M. A Perspective on the Role of Metals in Diabetes: Past Findings and Possible Future Directions. Metallomics **2009**, 1 (1), 32–41.

(11) Inzucchi, S. E.; Bergenstal, R. M.; Buse, J. B.; Diamant, M.; Ferrannini, E.; Nauck, M.; Peters, A. L.; Tsapas, A.; Wender, R.; Matthews, D. R. Management of Hyperglycaemia in Type 2 Diabetes: A Patient-Centered Approach. Position Statement of the American Diabetes Association (ADA) and the European Association for the Study of Diabetes (EASD). Diabetologia **2012**, 55 (6), 1577–1596.

(12) Gonzalez, J.; Safren, S.; Cagliero, E.; Wexler, D.; Delahanty, L.; Wittenberg, E.; Blais, M.; Meigs, J.; Grant, R. Deperssion, Self-Care, and Medication Adherence in Type 2 Diabetes. Diabetes Care **2007**, 30 (9), 2222–2227.

(13) Bolen, S.; Feldman, L.; Vassy, J.; Wilson, L.; Yeh, H.; Marinopoulos, S.; Wiley, C.; Selvin, E.; Wilson, R.; Bass, E. B.; et al. Systematic Review: Comparative Effectiveness and Safety of Oral Medications for Type 2 Diabetes Mellitus. Ann. Intern. Med. **2007**, 147 (6), 386.

(14) Baynes, J.; Thorpe, S. Perspectives in Diabetes. J. Natl. Med. Assoc. **1962**, 54 (1), 476–478.

(15) Giugliano, D.; Ceriello, An.; Paolisso, G. Oxidative Stress and Diabetic Vascular Complications. Diabetes Care **1996**, 19 (3), 257–267.

(16) Brownlee, M. Biology of Diabetic Complications. Nature **2001**, 414 (December), 813–820.

(17) Liu, Y.; Chen, C.; Summers, S.; Medawala, W.; Spence, D. M. C-Peptide and Zinc Delivery to Erythrocytes Requires the Presence of Albumin: Implications in Diabetes Explored with a 3D-Printed Fluidic Device. Integr. Biol. (United Kingdom) **2015**, 7 (5), 534–543.

(18) Panero, F.; Novelli, G.; Zucco, C.; Fornengo, P.; Perot, M. Fasting Plasma C-Peptide and Micro- and Macrovascular Complications in a Larg ... **2009**, 32 (November).

(19) Genuth, S.; Alberti, K. G. M. M.; Bennett, P.; Buse, J.; DeFranzo, R.; Kahn, R.; Kitzmiller, J.; Knowler, W.; Lebovitz, H.; Lernmark, A.; et al. Follow-up Report on the Diagnosis of Diabetes Mellitus. Diabet. Care **2003**, 26 (11), 3160–3167.

(20) Alberti, K. G. M. M.; Zimmet, P. Z. Definition, Diagnosis and Classification of Diabetes Mellitus and Its Complications. Part 1: Diagnosis and Classification of Diabetes Mellitus. Provisional Report of a WHO Consultation. Diabet. Med. **1998**, 15 (7), 539–553.

(21) Fu, Z.; Gilbert, E.; Liu, D. Regulation of Insulin Synthesis and Secretion and Pancreatic Beta-Cell Dysfunction in Diabetes. Curr Diabetes Rev **2009**, 19 (1), 389–399.

(22) Gilis-Januszewska, A.; Piątkowski, J.; Skalniak, A.; Piwońska-Solska, B.; Nazim, J.; Pach, D.; Przybylik-Mazurek, E.; Sowa-Staszczak, A.; Starzyk, J.; Hubalewska-Dydejczyk, A. Noninsulinoma Pancreatogenous Hypoglycaemia in Adults- a Spotlight on Its Genetics. Endokrynol. Pol. **2015**, 66 (4), 344–354.

(23) Flatt, P. R.; Bailey, C. J. Molecular Mechanisms of Insulin Secretion and Insulin Action. J. Biol. Educ. **1991**, 25 (1), 9–14.

(24) Free, A. H. Analytical Chemistry in the Conquest of Diabetes. **1984**, 56 (6), 664–684.

(25) Janes, T. Investigating Red Blood Cells in Autoimmune Diseases, 2018.

(26) Weiss, M. A. Chapter 2: The Structure and Function of Insulin; 2009; Vol. 6729, pp 33–49.

(27) Smith, G. D.; Swenson, D. C.; Dodson, E. J.; Dodson, G. G.; Reynolds, C. D. Structural Stability in the 4-Zinc Human Insulin Hexamer. Proc. Natl. Acad. Sci. U. S. A. **1984**, 81 (22), 7093–7097.

(28) Kelley, D. E.; Reilly, J. P.; Veneman, T.; Mandarino, L. J. Effects of Insulin on Skeletal Muscle Glucose Storage, Oxidation, and Glycolysis in Humans. Am. J. Physiol. **1990**, 258 (6 Pt 1), E923–E929.

(29) Saltiel, A. R.; Kahn, C. R. Insulin Signalling and the Regulation of Glucose and Lipid Metabolism. Nature **2001**, 414 (6865), 799–806.

(30) Keenan, H. a; Sun, J. K.; Levine, J.; Doria, A.; Aie, L. P. Residual Insulin Production and Pancreatic Beta-Cell Turnover After 50 Year ... Diabetes **2010**, 59 (11), 2846–2853.

(31) Sima, A. A. F. Diabetes & C-Peptide; Sima, A. A. F., Ed.; Humana Press: Totowa, NJ, 2012.

(32) Wahren, J.; Larsson, C. C-Peptide: New Findings and Therapeutic Possibilities. Diabetes Res. Clin. Pract. **2015**, 107 (3), 309–319.

(33) Rubenstein, A.; Clark, J.; Melani, F.; Steiner, D. Secretion of Proinsulin C-Peptide by Pancreatic β Cells and Its Circulation in Blood. Nature **1969**, 224, 177–178.

(34) Meyer, J. A.; Subasinghe, W.; Sima, A. A. F.; Keltner, Z.; Reid, G. E.; Daleke, D.; Spence, D. M. Zinc-Activated C-Peptide Resistance to the Type 2 Diabetic Erythrocyte Is Associated with Hyperglycemia-Induced Phosphatidylserine Externalization and Reversed by Metformin. Mol. Biosyst. **2009**, 5 (10), 1157–1162.

(35) Forst, T.; Kunt, T.; Wilhelm, B.; Weber, M. M.; Pf, A. Role of C-Peptide in the Regulation of Microvascular Blood Flow. Exp. Diabetes Res. **2008**, 2008.

(36) Forst, T.; Hach, T.; Kunt, T.; Weber, M. M.; Pfützner, A. Molecular Effects of C-Peptide in Microvascular Blood Flow Regulation. Rev. Diabet. Stud. **2009**, 6 (3), 159–167.

(37) Wallerath, T.; Kunt, T.; Forst, T.; Closs, E. I.; Lehmann, R.; Flohr, T.; Gabriel, M.; Schäfer, D.; Göpfert, A.; Pfützner, A.; et al. Stimulation of Endothelial Nitric Oxide Synthase by Proinsulin C-Peptide. Nitric Oxide - Biol. Chem. **2003**, 9 (2), 95–102.

(38) Cotter, M. A.; Ekberg, K.; Wahren, J.; Cameron, N. E. Effects of Proinsulin C-Peptide in Experimental Diabetic Neuropathy. Diabetes **2003**, 52 (March), 1812–1817.

(39) Kamiya, H.; Zhang, W.; Ekberg, K.; Wahren, J.; Sima, A. A. F. C-Peptide Reverses Nociceptive Neuropathy in Type 1 Diabetes. Diabetes **2006**, 55 (12), 3581–3587.

(40) Johansson, B. L.; Borg, K.; Fernqvist-Forbes, E.; Kernell, A.; Odergren, T.; Wahren, J. Beneficial Effects of C-Peptide on Incipient Nephropathy and Neuropathy in Patients with Type 1 Diabetes Mellitus. Diabet Med **2000**, 17, 181–189.

(41) Giebink, A.; Vogel, P.; Medawala, W.; Specne, D. C-Peptide-Stimulated Nitric Oxide Production in a Cultured Pukmonary Artery Endothelium Is Erythrocyte Mediated and Requires Zn2+. Diabetes. Metab. Res. Rev. **2014**, 32 (30), 13–23.

Chapter 3 – Protein Binding Under Diabetic Conditions

3.1 Background

3.1.1 Diabetes

Diabetes is a disease characterized by either an inability to produce insulin in vivo, type 1 diabetes (T1D), or a significant resistance to endogenous insulin, type 2 diabetes (T2D).[1] While the etiology of each form of diabetes is unique, hallmark features of both forms of diabetes are elevated glucose concentrations in the bloodstream and associated complications such as neuropathy (nerve damage), retinopathy (vision), and nephropathy (kidney failure).[1] Recently, reports have suggested that many of these complications are linked to overall poor blood flow in the circulation of people with diabetes.[2–4]

The inability to produce endogenous insulin in T1D necessitates the administration of exogenous insulin through a pump or syringe.[5] However, in relation to the aforementioned blood flow complications, insulin has no direct effect on most bloodstream cells. Specifically, insulin stimulates glucose transport through cells that contain the GLUT4 glucose transporter; the majority of cells in the bloodstream, such as red blood cells (RBCs), neutrophils, macrophages, T-cells, etc., contain the GLUT1 glucose transporter. In addition, the half-life of insulin in the circulation is only 3-4 minutes, thus its role in direct control over bloodstream properties, such as overall blood flow, may be minimal, suggesting roles for other pancreatic β-cell secretions.

C-peptide is a 31-amino acid peptide that is co-secreted in equimolar amounts with insulin from the pancreatic β-cells.[6–9] In contrast to insulin, C-peptide has a half-life in the bloodstream of approximately 30 minutes and has been shown to improve blood flow in

human and animal models.[7,10,11] Recently, the Spence group reported that C-peptide binding to cells requires delivery by albumin, one of the most abundant proteins in the human bloodstream.[12] Collectively, these reports suggest a potential role for C-peptide and zinc in the maintenance of blood flow.[13,14] Unfortunately, recent human trials involving C-peptide as a replacement therapy alongside insulin for T1D have proven unsuccessful.[15]

3.1.2 Advanced Glycation End Products

Poor regulation of both Type 1 and Type 2 diabetes leads to elevated blood glucose levels also known as hyperglycemia. Glucose in the body can modify proteins in two routes: glycosylation and glycation.[16] Glycosylation is the enzymatic route for the addition of a sugar molecule to other organic moieties. Glycation is the non-enzymatic addition of a sugar molecule. Glycation will be the focus of this section.

Glycation occurs over a series of complex steps (**Figure 3.1**).[16–18] First the glucose in the linear chain form reacts with a free amino group on the protein to form a highly unstable Schiff base products. This Schiff base can rearrange to form the Amadori product, another unstable form. From the Amadori product the molecule can be oxidized to form the irreversible Advanced Glycation End Products (AGEs).[16,17]

The glycation reaction was first observed in 1912, but did not have medical relevance until 1963 when an unknown variant of hemoglobin was discovered.[16,17] It took until 1967 for this new hemoglobin (Hb) species to be correlated with diabetes and characterized as glycated hemoglobin. Finally, in 1968 it was confirmed in people with

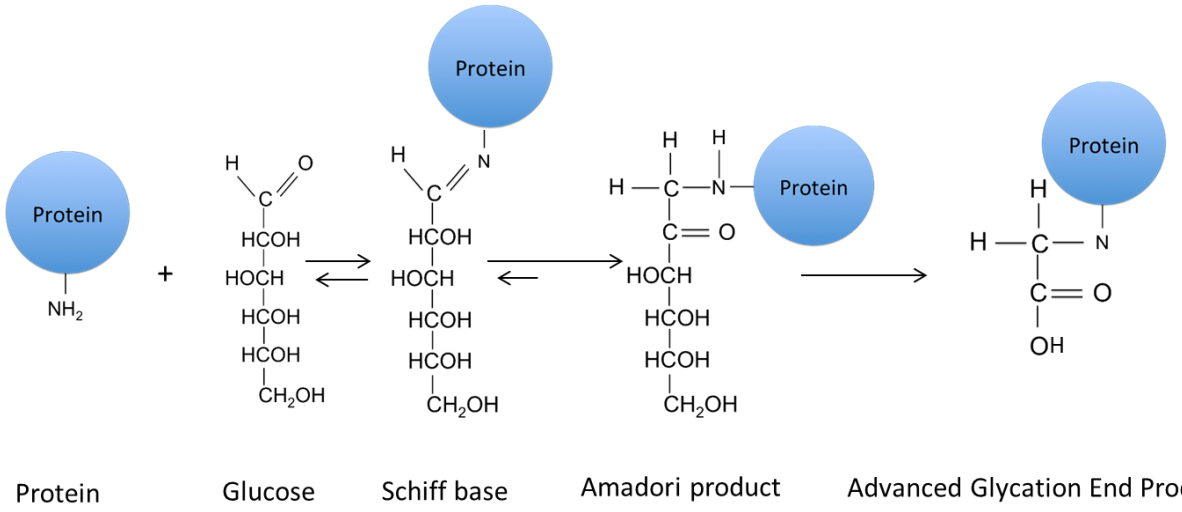

Figure 3.1: Route for production of Advanced Glycation End Products within the body. Linear glucose molecule binds with primary amine forming the highly unstable Schiff base. From there a rearrangement occurs forming the Amadori product, another reversible form. Finally, the Amadori product can be oxidized to form the AGE.

diabetes that this, now named HbA_{1C}, variant of hemoglobin was present in elevated levels.[17] Since that time, a full characterization of the $HbA_{1C,}$ or A1C for short, levels in the body has been performed on both heathy and diabetic individuals. The A1C concentration is now used as a marker for the long term, ~3 months, regulation of blood glucose levels in people with diabetes.

After the discovery of HbA_{1C} and the subsequent acceptance that non-enzymatic glycation can occur under physiological conditions, a new push was made to understand the effect of AGEs on the body. AGEs have been found in a wide variety of body tissues including muscle, lung, liver, coronary, etc.[19–21] In addition to cells being directly affected by being modified through glycation, some cells have AGE specific receptors known as RAGE. These RAGE have been linked to compromised function of endothelial cells and ultimately microvascular deterioration.[21–23] In addition to compromised cell function, glycated proteins, specifically albumin for our consideration, are reported to have compromised binding under glycation conditions.[24–29]

3.1.3 Motivation for this Work

To gain a better understanding of the binding relationship between albumin, C-peptide, and Zn^{2+}, the Spence group recently developed a 3D-printed membrane dialysis system to quantitatively characterize binding constants.[30] While this method provided many benefits over existing dialysis methods (cost, customized membrane integration and throughput), it still required nearly 6 hours to reach equilibrium in this diffusion-driven model. Here, we employ ultrafiltration through membranes integrated into 3D-printed devices. Ultrafiltration uses high pressure or centrifugal force to drive solution and low molecular weight compounds through a membrane while retaining high molecular weight compounds, as depicted in **Figure 3.2**. Ultrafiltration requires a small amount of sample

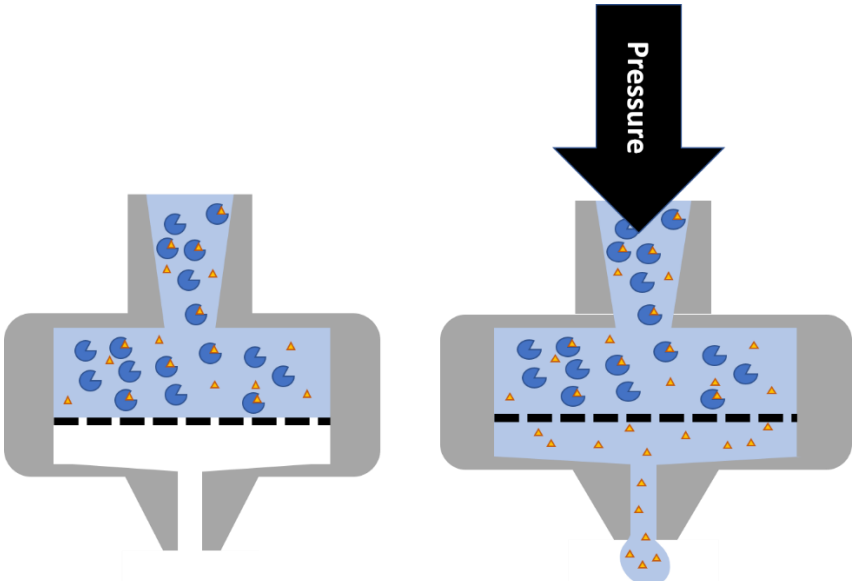

Figure 3.2: Illustration of the principle of ultrafiltration binding studies. A sample containing a combined mixture of protein and ligand is loaded into a device containing a size-exclusion membrane with pores small enough to block the protein and protein-ligand complex from passing through. Pressure is used to drive a small aliquot of solution containing the unbound-ligand through the membrane pores. The concentration of unbound-ligand eluted through the membrane represents the concentration of unbound ligand in the original sample.

be separated from the bulk solution for analysis.[31] The equilibrium of the binding system is not affected by ultrafiltration when the separated portion is low in volume (2-10% of the total volume), therefore the concentration of ligand in the ultrafiltrate represents the concentration of free-ligand in the bulk sample.[31] Commercial devices exist for the determination of protein binding by ultrafiltration, however we propose that customized filtration devices provide a cost effective, versatile, and contaminate-free membrane system. Thus, we have developed a 3D–printed, syringe-compatible device for the determination of protein binding to ligands. We employ this system here to investigate the binding of Zn^{2+} and C-peptide to albumin, and a glycated form of albumin that may be found in people with T1D, to determine if modified forms of albumin affect this protein's ability to bind C-peptide and Zn^{2+}.

3.2 Methods

3.2.1 Membrane Preparation

Cellulose dialysis membranes (12-14 kilodalton MW cut off) were purchased in flat sheets from Spectrum Laboratories, Inc. (Rancho Dominguex, CA). Slide-a-Lyzer dialysis cassettes (20 kilodalton MW cut off) were purchased from ThermoFisher Scientific (Waltham, MA), and used as received after the membrane portion was removed with a razor blade. The membrane sheets were placed between two sheets of wax paper and cut in 15-mm diameter circles with an H- Series 5th Gen CO2 Desktop Laser cutter (Full Spectrum Laser, Las Vegas NV). For this laser cutter, the power was set to 22% and a speed of 100%.

3.2.2 Support- Free Printing for Direct Membrane Integration

An O-ring was designed using CAD software (Autodesk Inventor Professional, San Rafael, CA) and submitted to a J750 Multi-Material Polyjet 3D-printer (Stratasys, Eden Prairie, MN) as a .STL file. The exact dimensions of this O-ring can be found in **Figure 3.3(A-C)**. **Figure 3.3(A & B)** shows the dimensions of the O-ring in which the membrane is imbedded from a side view and a top down view. **Figure 3.3C** shows a cut out of the O-ring.

In order to get the printer to print the models completely support free, certain requirements must be met. First, the thinnest wall that can be printed in the XY plane is 1 mm. Anything under 1 mm requires support material. The second requirement is that there can be no material changes in the Z axis. This means that the O-ring could not have a full layer of Tango+, followed by a full layer of VeroClear on top. The final design incorporates VeroClear material for rigidity as well as Tango+ material for its rubbery, O-ring like properties

The printer was set to print without the use of support material by accessing the Stratasys Parameters Manager page on the computer embedded within the printer. Here, the following parameters were changed from their previous values to zero millimeters: Carpet_height, Carpet_protectorZ, and ImproveSupport_thickOfPedestal. Changing these values instructs the printer to not add any support bed to the final device, in this case, the O-ring. However, these settings do not preclude the printer from adding support to devices with more complex geometries, such as channels and overhangs. The reason for this strategy is shown in **Figure 3.4A** where support material is covering the

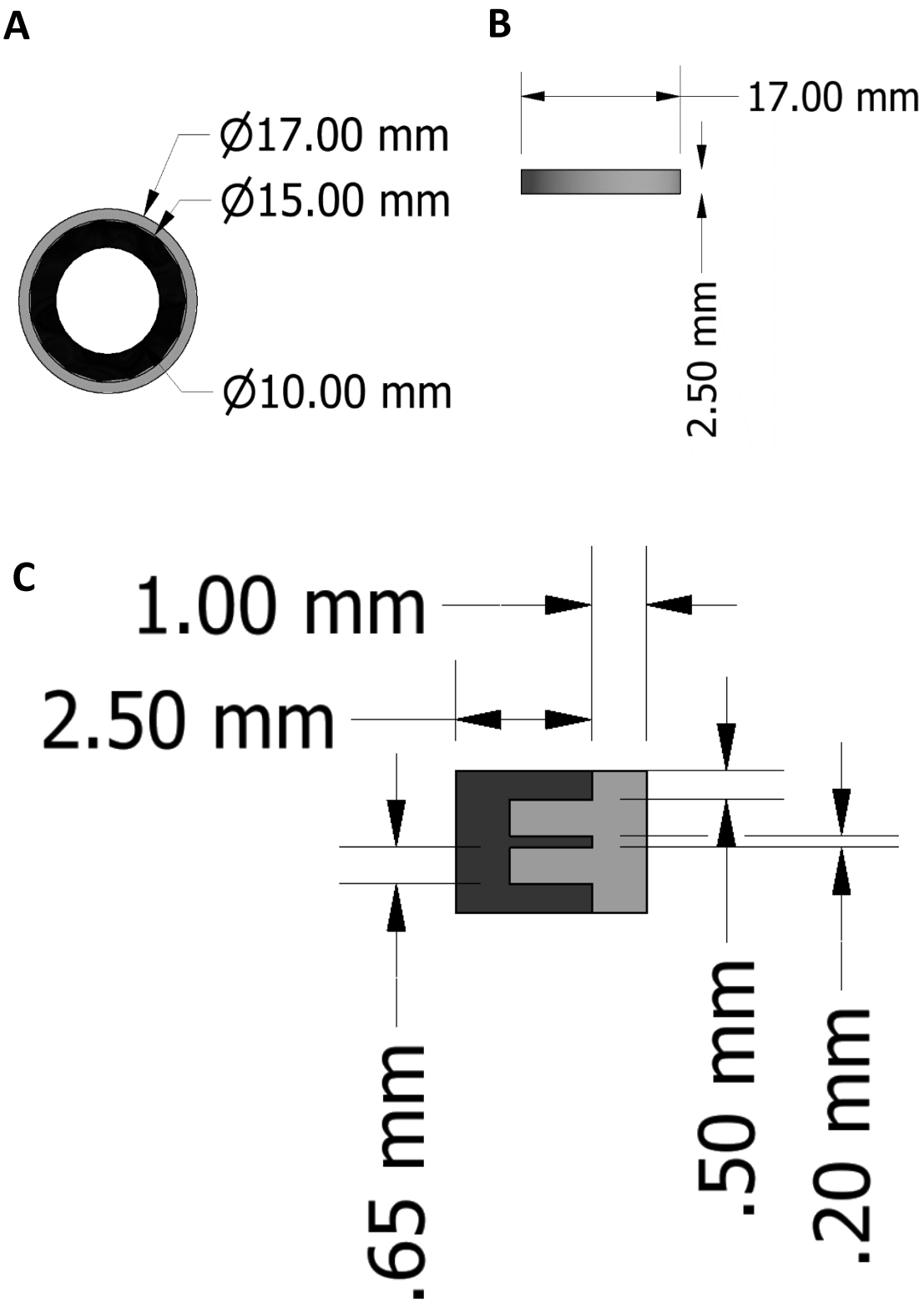

Figure 3.3: Dimensions of the membrane-holder O-ring. Black areas denote Tango+ material, whereas grey areas denote VeroClear.(A) Top view, (B) Side view, and (C) Cross-section of the ring.

membrane and **Figure 3.4B** where the device was printed support free. In order to seamlessly seal the membrane into the device without the use of glue or adhesives, the membranes were integrated into the device by a Print-Pause-Print technique previously reported by our group.[30] Halfway through the print-job, the printer was paused and the freshly cut membranes were laid on the center of the O-rings. Then, the printing process was resumed, layering material over the edges of the membrane, and curing the material with UV-light thereby sealing the membrane into the device. The final product without any post-processing is shown in **Figure 3.4B**.

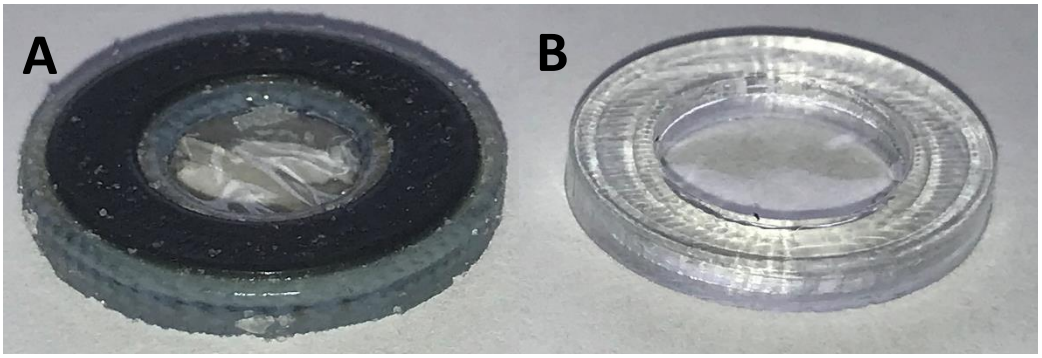

Figure 3.4: (A) support covered membrane-holding O-ring, and (B) support-free membrane holding O-ring. The problematic debris left behind from the support material can be seen in 3A. Whereas the picture in 3B shows a device made when the printer has been modified to print without a support base and without support surrounding the model, leaving a clean uncontaminated membrane surface.

3.2.3 Design of a 3D-Printed Syringe Device for Ultrafiltration

A custom ultrafiltration device was fabricated to house any membrane, and to fit on the end of a 1 mL plastic syringe (**Figure 3.5**). The membrane holder has four major components: the top, the bottom, the membrane support, and the membrane O-ring. The four parts, shown in **Figure 3.5A**, are assembled by threading the top into the bottom, thereby holding the O-ring and support in between.

The membrane support, top, and bottom utilize the ability of the 3D printer to print multiple materials that have rubber-like properties (Tango+) or hard plastic properties (VeroClear). The top has a Tango+ gasket in which the syringe is inserted, resulting in a sealed connection. The device has 3D printed threads with a standard metric thread size/pattern of M20x1 RH. Inside the top and bottom, another Tango component was incorporated to provide a gasket to give a water tight seal around the membrane O-ring. The membrane support is printed out of hard plastic and features a 1 mm x 1 mm grid to prevent the membrane from stretching or deforming during the separation. The assembled device is shown in **Figure 3.5B**. Annotated dimensions of the top, bottom, and support can be seen in **Figures 3.6, 3.7, and 3.8** respectively

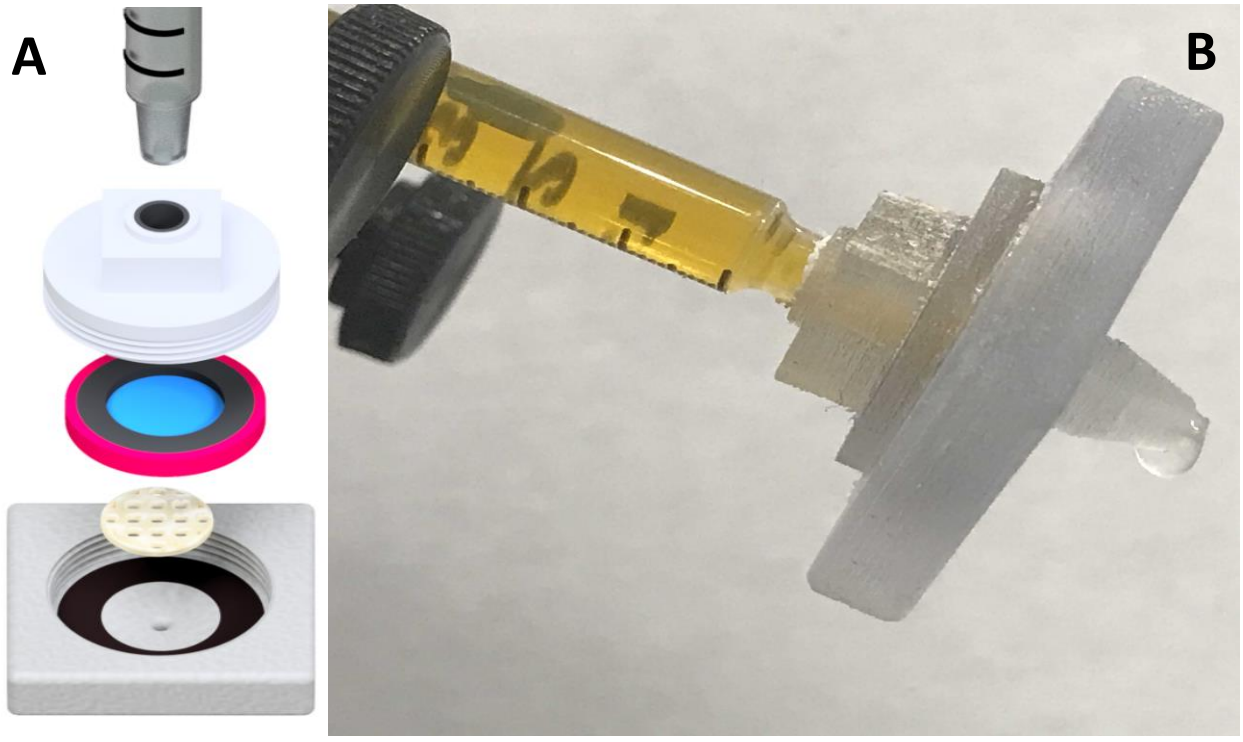

Figure 3.5: (A) CAD representation of full device, and (B) photograph of assembled device with an orange-colored protein solution in the syringe which cannot pass through the membrane, and therefore a clear drop of buffer is eluted from the device.

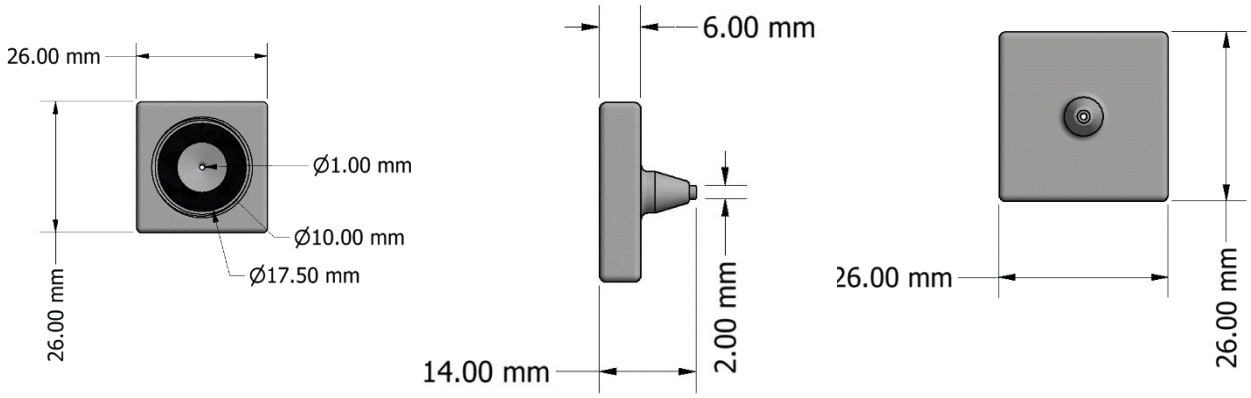

Figure 3.6: Annotated CAD representations of the bottom component. Black areas denote Tango+ material, whereas grey areas denote VeroClear.

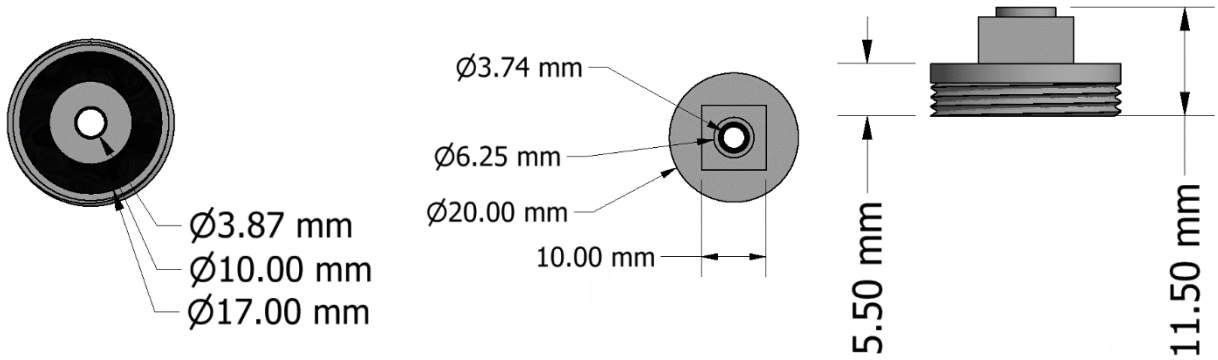

Figure 3.7: Annotated CAD representations of the top of the membrane holder device. Black areas denote Tango+ material, whereas grey areas denote VeroClear.

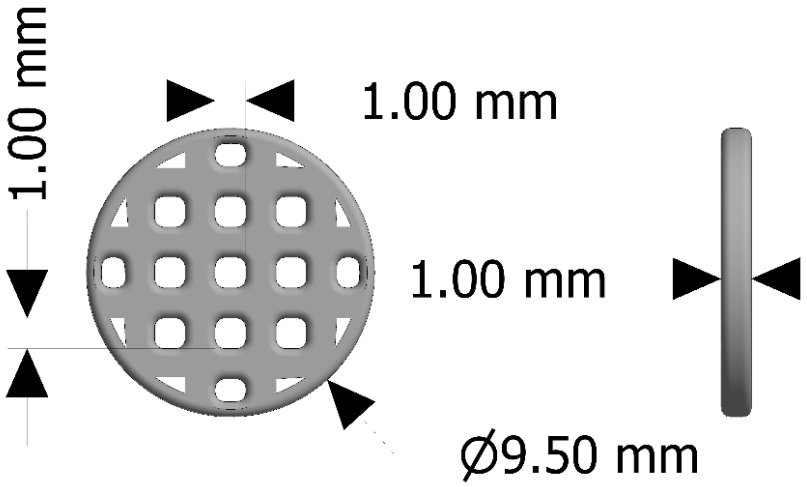

Figure 3.8: Annotated CAD representation of the membrane support structure.

3.2.4 Design of a 3D- Printed Centrifugation Filter System

A 3D print centrifugation filter was designed to fit inside of a 1.7 mL Posi-Click Tube (Denville Scientific, Holliston, MA). The device was printed on a Stratasys J750 set in support free mode. The device was designed in five components: support, three layers of sealing rubber, and the cup **(Figure 3.9)**. Each component was a separate print job with the stage height being adjusted in between prints so as to layer the components directly on top of each other. In between the rubber sealing layers membranes were inserted. A 0.1 µm pore size polycarbonate membrane was placed first to act as extra support to either 12-14 kDa cutoff or 20 kDa cutoff cellulose membranes, the same as

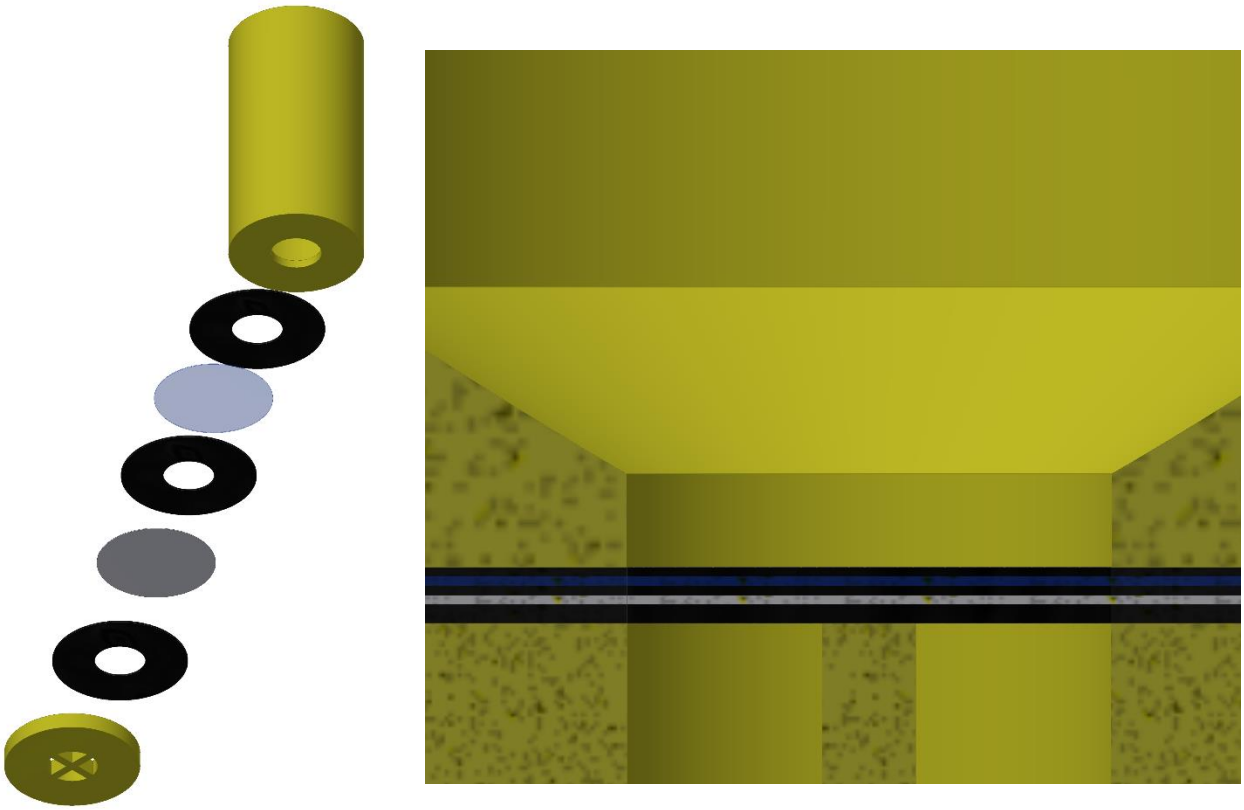

Figure 3.9: (Left) CAD representation of the centrifuge filter system. With hard plastic (Vero) in yellow, Tango+ in black, Polycarbonate membrane in gray, and cellulose membrane in clear blue. (Right) Cross section of assembled centrifuge filter system with same color scheme. The membranes can be sandwiched between layers of Tango+.

mentioned in section 3.2.1. Due to the design considerations, and the layering of the print jobs this device was printed completely support material free. Dimensions of the device are annotated in **Figure 3.10**.

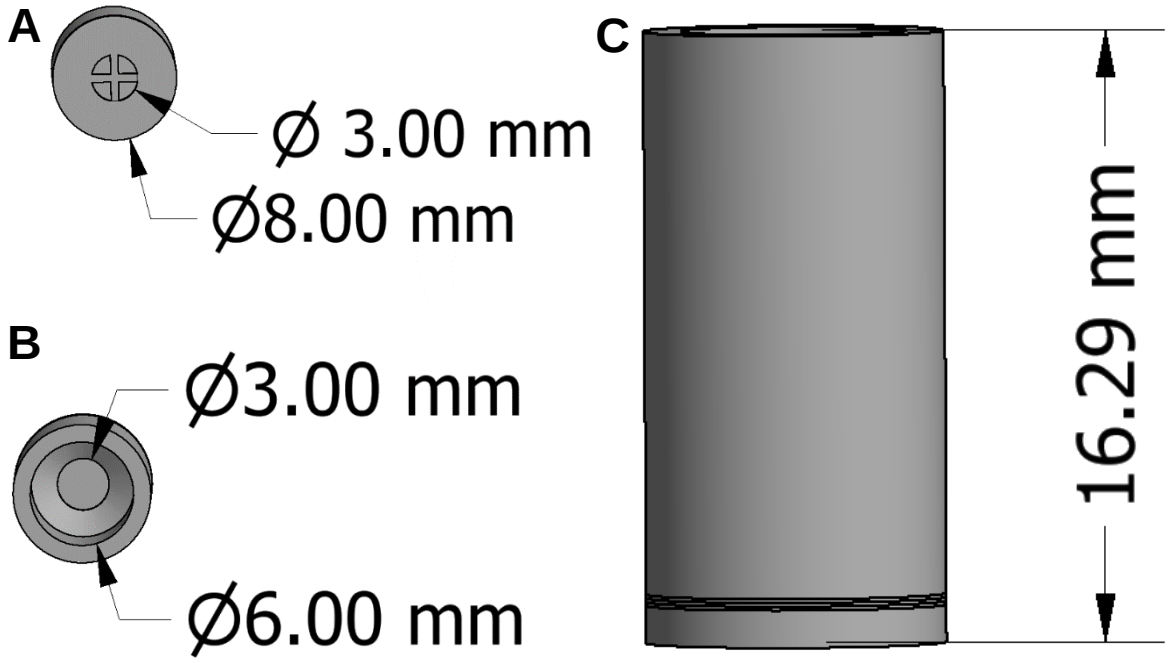

Figure 3.10: Annotated CAD representation of the assembled centrifuge filter system. (A) bottom up view, (B) Top down view, and (C) Side View.

3.2.5 Sample Preparation

A 10.5 mM Tris buffer (pH 7.4) with 150 mM NaCl was prepared. 10 mg of either human serum albumin (nHSA) (Sigma Aldrich, St. Louis MO) or glycated human serum albumin (gHSA) (Sigma Aldrich) were diluted to 1 mL with the Tris-NaCl buffer, and sterile filtered through Millex-GV 0.22 micron filter units from Merck Millipore (Burlington, MA). The protein concentration was then quantitatively determined using the Pierce

bicinchoinic acid (BCA) assay (ThermoFisher Scientific). The homogeneity and relative extent of glycation of commercially purchased nHSA and gHSA were determined by time-of-flight mass spectrometry with electrospray ionization via a Xevo G2-XS TOF-MS from Waters (Milford, MA) and MassLynx (Waters) software at the Michigan State University Mass Spectrometry and Metabolomics Core Facility. An aliquot of the sample was injected via an autosampler onto a UPLC desalting column coupled to the electrospray mass spectrometer, with a gradient mobile-phase consisting of 0.1% formic acid in water and acetonitrile. The LC gradient gradually increased the amount of acetonitrile in the mobile phase over the course of 15 minutes. The spectrum deconvolution and data analysis were carried out with the MaxEnt tool in the MassLynx software before being exported into spreadsheet software for analysis. The extent of glycation was assessed by centroiding the peaks on the spectrum, comparing the ion counts of the peaks shifted +162 Daltons higher than the main albumin peak at 66,437 Da (**Figure 3.11**), and dividing the counts of these peaks by the total-ion-count of the full spectrum.

For Zn^{2+}-protein binding experiments, a solution containing 10 µM albumin and 80 µM radioactive 65ZnCl2 stock (PerkinElmer) was prepared in the Tris-NaCl buffer, such that the final Zn^{2+} concentrations ranged from 1.5 µM to 32.5 µM. In order to assess the interference of glucose with Zn^{2+} binding to albumin, a separate Tris/NaCl buffer containing 20 mM glucose was prepared to make a final sample containing 182 µM glucose, 10 µM albumin, and 5 µM Zn^{2+}. After quantifying the amount of free-Zn^{2+} in the sample, the amount of Zn^{2+} bound to protein was calculated using Equation 1, and the percentage of the ligand bound to protein was calculated using Equation 2.

$$(1): \quad [\text{Bound Ligand}] = [\text{Total ligand}] - [\text{Free ligand}]$$

$$(2): \quad \text{Percent Protein Bound} = \frac{[\text{Bound ligand}]}{[\text{Total ligand}]}$$

Crude C-peptide was purchased from Peptide 2.0 (Chantilly, VA) and purified to > 99% by HPLC. To measure the binding of C-peptide to albumin, a C-peptide stock of approximately ~100 μM was prepared in distilled and deionized water (DDW). An aliquot of the peptide was then mixed with either nHSA or gHSA in Tris/NaCl as 0.7 mL samples with a final albumin concentration of 10 μM and varying C-peptide concentrations from 1-30 μM.

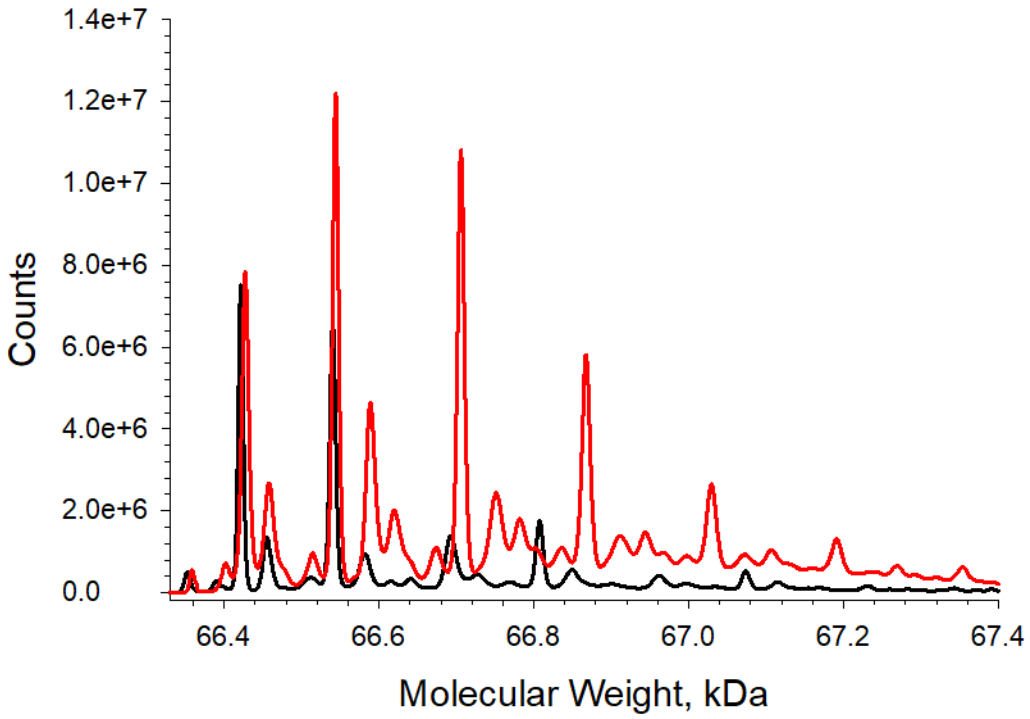

Figure 3.11: Time of Flight Mass Spectrometry analysis of intact normal (black) and glycated (red) human serum albumin. This data was used to estimate the relative extent of glycation of each protein by comparing peaks shifted +162 daltons from the main peak at 66,437 daltons to the total ion counts of the full spectrum.

3.2.6 Syringe Device Setup

Parts that contained support material had bulk support removed by hand. The parts were then soaked overnight in a 500-mL solution that was over-saturated with sodium bicarbonate. The sodium bicarbonate increases the pH of the solution and also acts as a mild abrasive, which helps to solubilize and remove the remaining support-material. The parts were then thoroughly rinsed with distilled water to remove the remaining support-material and dried with compressed air. A 1-mL syringe was then inserted firmly into the top component and subsequently filled with a 1-mL aliquot of sample containing albumin with either Zn^{2+}. The membrane O-ring was then placed into the top portion followed by the membrane support (which was shown assembled in Figure 2C) and then the device was threaded together until tight. The entire device was then vortexed for approximately one second, which helps to move any trapped air-bubbles above the membrane to the top of the syringe. The syringe with device attachment was then placed into an upright syringe pump and set to a flow rate of 500 µL/ min to push a 12-15 µL aliquot of sample through the membrane.

3.2.7 Sample Analysis of Zn^{2+} For Syringe Device

A 12-15 µL drop was collected in a 1 mL centrifuge tube. Next, 10 µL of sample were pipetted into a 96-well scintillation plate and mixed with 100 µL of scintillation cocktail. A calibration curve was prepared with external standards to quantitatively determine signals obtained from samples. Each standard was determined by adding a 10 µL aliquot of each standard into the plate wells and mixed with the scintillation cocktail. The plate was inserted into a Scintillation Counter (PerkinElmer MicroBeta TriLux 1450) with a delay of 30 minutes for measurement.

3.2.8 Centrifuge Filter System Sample Setup

Devices were removed from the print tray and stored in a sealed container at room temperature until used. Using forceps, one device was placed in a 1.7 mL Posi-Click Tube (Denville Scientific, Holliston, MA). 200 µL of the $^{65}Zn^{2+}$/ HSA solution was pippeted into the device and the decvice was carefully capped an placed into a Sorvall Biofuge Stratos Centrifuge (ThermoFisher Scientific, Waltham, MA) equipped with a Heraeus #3331 24 tube rotor. Samples were then spun at 10000xg for 2 hours.

3.2.9 Sample Analysis of Zn^{2+} For Centrifuge Filter System

A 11-12 µL drop was collected in the bottom of the 1.7 mL tube. Next, 10 µL of sample were pipetted into a fresh 1.7 mL tube. A calibration curve was prepared with external standards to quantitatively determine signals obtained from samples. Each standard was determined by adding a 10 µL aliquot of each standard into a fresh 1.7 mL tube. Each tube was placed into the autosampler of a Wizard^2 2480 Automatic Gamma Counter and read for 20 minutes at 1116 keV.

3.2.10 Calculations and Data Analysis

The concentration of free ligand in the sample was determined by quantifying the amount of ligand eluted through the membrane. The concentration of bound ligand was determined by subtracting the concentration of free ligand from that of the total ligand in the sample. The free vs. bound ligand was plotted to create a saturation binding-curve, which was then analyzed by non-linear regression software (SigmaPlot 13.0) for the calculation of a binding (Kd) and stoichiometry (n) constant.

3.3 Results

A commercially available dialysis membrane was integrated directly into a 3D-printed device for protein-binding experiments. Novel 3D-printing techniques were employed to incorporate the membrane into the device without the use of support material. Polyjet 3D printers rely on a soft, sacrificial material to support the model during the print process. When incorporating a membrane into the printing process, the printer would normally lay support material onto the membrane, therefore contaminating the membrane and clogging its pores. The printer parameters were altered, and the device geometry was optimized so that the printer laid no support material when printing the membrane-holding O-ring, which is fabricated with two materials and contains an embedded cellulose membrane. The rubber-like material (Tango+) is used to provide a water tight seal, which is essential to ensure that all bulk solution transport across the membrane occurs through the pores of the membrane, as opposed to going around the membrane. The Tango+ material is not rigid enough to support the integrated membrane; thus, a hard-plastic (VeroClear) component was incorporated to add rigidity to the system. The final result is the membrane holding O-ring featured in Figure 2B. The ability to imbed the membranes directly into the 3D-printed device, while also printing completely support-free results in no requisite post processing, limiting the chance for the membrane to be contaminated and enabling earlier use of the device.

Device utility was characterized by measuring the binding affinity of Zn^{2+} to nHSA **(Figure 3.12)**, followed by comparison with literature values. The experimentally determined binding constant (Kd = 5.77 ± 0.19 x 10-7 M) and stoichiometry (n = 2.0 ± 0.2) are statistically equal to literature values by equilibrium dialysis (Kd = 5.62 ± 0.93 x 10-7

M, n = 1.6 ± 0.2). Collection of a 12-15 µL drop of sample through a 12-14 kilodalton MWCO membrane required an average of 36.0 ± 5.1 minutes (n=4) using the flow rate described above.

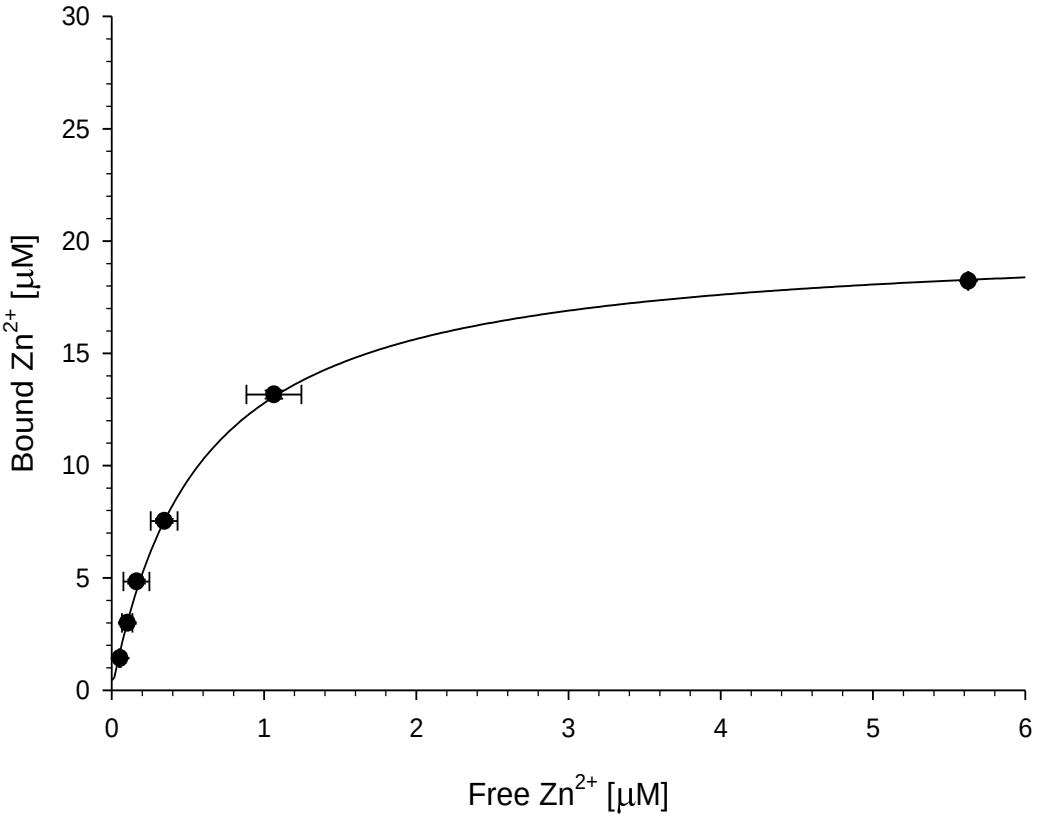

Figure 3.12: Non-linear regression software (SigmaPlot) was used to plot the concentration of free zinc vs the concentration of bound zinc, this graph was used to calculate the binding affinity (K_d= 5.77 ± 0.19) × 10^{-7} M) and the binding stoichiometry (n=2.0 ± 0.2) of Zn^{2+} to human albumin, the goodness of fit of the curve was calculated to be. R2 = 0.9989. n=4, error= standard deviation.

As shown in **Figure 3.13**, a significantly different saturation binding curve was obtained when the Zn^{2+} binding to a commercially available gHSA was determined. From the non-linear regression binding-analysis, the binding constant (Kd) and stoichiometry (n) were determined to be 3.62 ± 0.89 x 10-7 M and 0.53 ± 0.24, respectively, (R2 = 0.961), which suggests binding of 1 atom of Zn^{2+} per 2 molecules of gHSA. The mass

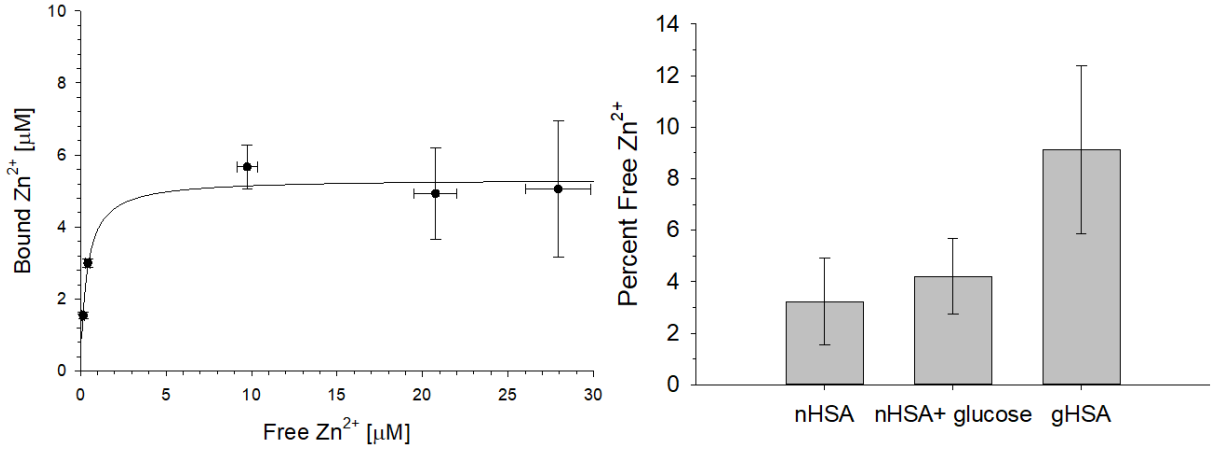

Figure 3.13: Saturation binding curve analysis of glycated human albumin to zinc (n=4). The relative amount of zinc bound to normal albumin with and without glucose in the buffer, and to glycated human albumin (error =s.d. n=4).

spectrometry analysis (**Figure 3.11**) shows that each albumin sample is heterogeneous in that there are several peaks shifted higher in mass than the nominal 66,437 Dalton peak. Notably, a peak shifted +162 daltons corresponds to a glycation event, or the addition of a covalently attached glucose molecule.[24,25] The peaks corresponding to an additional glucose molecule, or multiple glucose molecules, comprised approximately 14 % of the total ion counts for the nHSA, compared to 67% of the gHSA.

To determine if glucose added directly to the protein sample is sufficient to reduce its ability to bind Zn^{2+}, an experiment was performed where the Zn^{2+} and albumin concentrations were held constant between 3 samples, while varying the glucose concentration. Each sample contained 10.0 µM nHSA or gHSA and 5.0 µM Zn^{2+}, while one of the nHSA samples contained a glucose concentration of 182 µM, which is approximately equal to the concentration ratio of glucose-to-albumin in the bloodstream of people with diabetes (8-11 mM glucose: 0.63 mM albumin). The unbound, or free-zinc was determined and the percentage of free and bound Zn^{2+} was calculated according to

Equation 2 and shown in **Figure 3.13**. The percentage of free Zn^{2+} in the nHSA sample and glucose-containing nHSA sample were not statistically different (3.2 ± 1.7 %, and 4.2 ± 1.4%, respectively). However, the percentage of free Zn^{2+} in the gHSA sample was approximately 2-3 fold higher than the nHSA sample (9.1 ± 3.2 %, n=5). Therefore, the percentage of protein-bound Zn^{2+} in the final samples were as follows: nHSA (96.7 ± 1.7%), nHSA with added glucose (95.8 ± 1.4%), and gHSA without added glucose (90.9 ± 3.2%).

In order to increase throughput and reliability, a 3D printed centrifuge filter system was explored. Reproducibly of the device was characterized with both 12kDa and 20 kDa cutoff cellulose membranes, **Figure 3.14A** and **3.14B**. It was determined that there was a higher failure rate at 15000xg so 10000xg was the highest spin rate that could be reliably used. For the analysis by either the Scintillation counter or the gamma counter, a

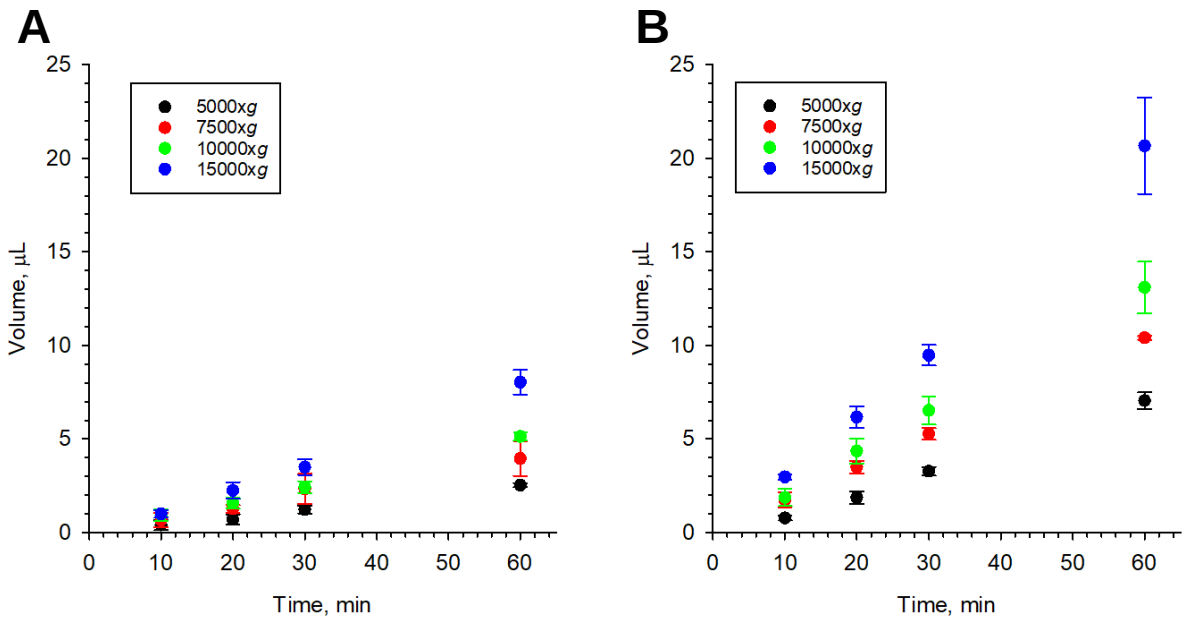

Figure 3.14: Characterization of the volume of effluent as a function of time at various spin rates for the centrifugation filter system with 12 kDa cutoff cellulose membranes (A) and 20 kDa cutoff cellulose membranes (B).(error=s.d., n ≥ 3)

minimum of 10 µL of sample was needed for the concentration range used. To get 10 µL with the 20 kDa membranes the device had to be centrifuged at 10000xg for 60 minutes **(Figure 3.14B)**. To get 10 µL with the 12 kDa membranes the data was extrapolated assuming a linear correlation and 120 minutes was required.

For further characterization, Zn^{2+}/ HSA binding was again measured **(Figure 3.15)**. The amount of free Zn^{2+} was measured at a single Zn/ HSA ratio, 5 µM Zn^{2+} and 10 µM HSA. It was determined that percentage free zinc as determined by the centrifuge filter method was not statically different from that determined by the syringe method, 3.3 ± 1.3 % and 3.2 ± 1.7 % respectively.

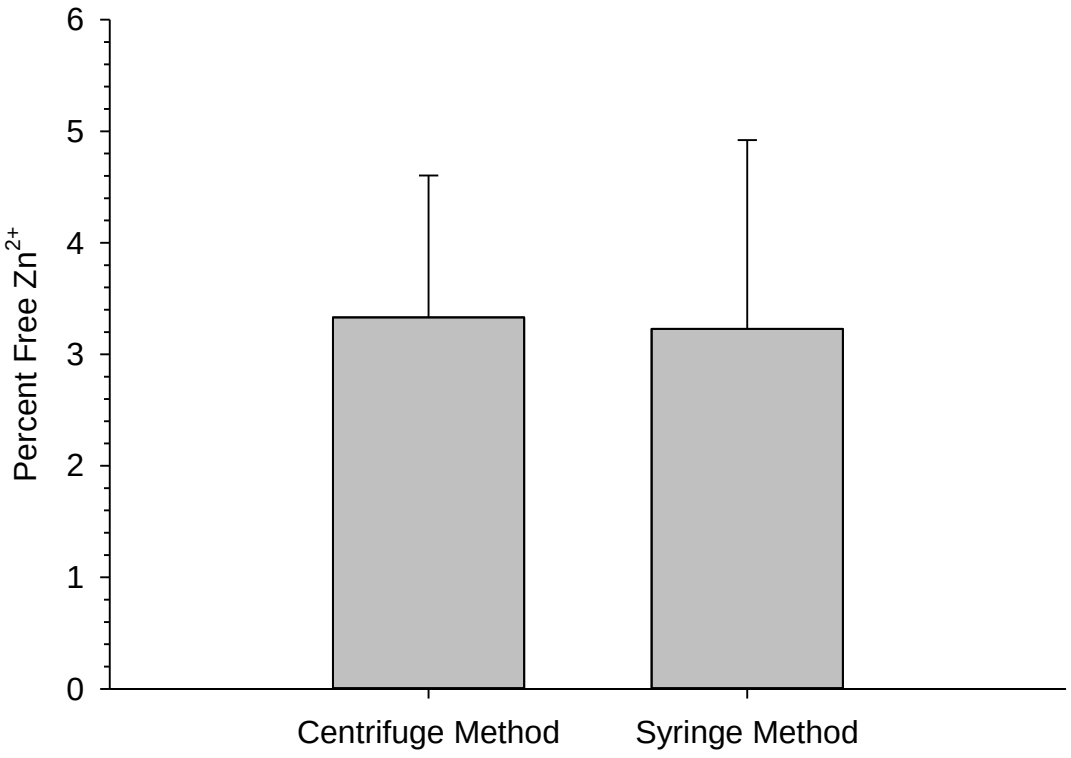

Figure 3.15: Relative amount of free zinc in a solution of 5 µM Zn^{2+} and 10 µM HSA as determined by both the centrifuge method and the syringe method (error =s.d. n=4).

3.4 Discussion

Here, we developed a new 3D printed platform for performing ultrafiltration binding experiments. The device utilizes a novel printing process that allows the user to integrate any commercially available membrane onto the end of a syringe. In the device shown, the membranes used were size-exclusion dialysis membranes with molecular weight cutoffs of 12 and 20 kilodaltons. These sizes were chosen in order to block proteins from passing through the pores, but still allowing smaller molecular weight species and buffer to pass through. These printing techniques allow the user to better control experimental factors such as membrane type, pore size, porosity, and potential sources of contamination. The device was characterized by measuring equilibrium binding constants for Zn^{2+} to albumin and C-peptide to albumin that agree with literature values.

Albumin is the most common protein found in the bloodstream and is well known to be a carrier-protein that helps bind and distribute ligands throughout the body. It is now well documented that the ability of albumin to bind certain ligands becomes compromised under high-glucose conditions, such as those seen in diabetes.[24–28] The high-glucose conditions of the diabetic bloodstream cause an increased amount of glucose to become covalently attached to the albumin via the Maillard reaction, forming glycated-albumin.[25,28,32] Here, we studied the difference between normal-albumin and glycated-albumin's ability to bind ligands important in diabetes, Zn^{2+} and C-peptide. The commercially purchased glycated-albumin showed approximately equal binding affinity for C-peptide as the normal-albumin. However, the binding characteristics between Zn^{2+} and glycated-albumin were significantly different than the normal-albumin.

Similarly, the Hage group has previously reported high-performance affinity chromatography methods for studying the binding of diabetic drugs to glycated-albumin in this journal.[27] The 3D-printed device described here can perform similar analyses with any receptor/ligand combination with a large enough difference in molecular weight (recommended approximately >20 fold difference), in under one hour, without the need for an HPLC.

REFERENCES

REFERENCES

(1) International Diabetes Federation Diabetes Atlas, 8th Edition; Karuranga, S., Rocha Fernandes, J. da, Huang, Y., Malanda, B., Eds.; 2017.

(2) Williams, S. B.; Cusco, J. A.; Roddy, M. A.; Johnstone, M. T.; Creager, M. A. Impaired Nitric Oxide-Mediated Vasodilation in Patients with Non-Insulin-Dependent Diabetes Mellitus. J. Am. Coll. Cardiol. **1996**, 27 (3), 567–574.

(3) McVeigh, G. E.; Brennan, G. M.; Johnston, G. D.; McDermott, B. J.; McGrath, L. T.; Henry, W. R.; Andrews, J. W.; Hayes, J. R. Impaired Endothelium- Dependent and Independent Vasodilation in Patients with Type 2 (Non-Insulin- Dependent) Diabetes Mellitus. Diabetologia **1992**, 35, 771–776.

(4) Dugan, J.; Pfotenhauer, K.; Young, Cl.; Shubrook, J. H. Diabetes Microvascular Complications. Prim. Care Reports **2017**, 23 (May), 1–28.

(5) Banting, F. G.; Campbell, W. R.; Fletcher, A. A. Further Clinical Experience with Insulin (Pancreatic Extracts) in the Treatment of Diabetes Mellitus. Br. Med. J. **1923**, 1 (3236), 8–12.

(6) Medawala, W.; McCahill, P.; Giebink, A.; Meyer, J.; Ku, C. J.; Spence, D. M. A Molecular Level Understanding of Zinc Activation of C-Peptide and Its Effects on Cellular Communication in the Bloodstream. Rev. Diabet. Stud. **2009**, 6 (3), 148–158.

(7) Sima, A. A. F. Diabetes & C-Peptide; Sima, A. A. F., Ed.; Humana Press: Totowa, NJ, 2012.

(8) Steiner, D. F.; Cunningham, D.; Spigelman, L.; Aten, B. Insulin Biosynthesis: Evidence for a Precursor. Science (80-.). **1967**, 157 (3789), 697–700.

(9) Rubenstein, A.; Clark, J.; Melani, F.; Steiner, D. Secretion of Proinsulin C-Peptide by Pancreatic β Cells and Its Circulation in Blood. Nature **1969**, 224, 177–178.

(10) Cotter, M. A.; Ekberg, K.; Wahren, J.; Cameron, N. E. Effects of Proinsulin C-Peptide in Experimental Diabetic Neuropathy: Vascular Actions and Modulation by Nitric Oxide Synthase Inhibition. Diabetes **2003**, 52 (7), 1812–1817.

(11) Sima, A. A. F.; Zhang, W.; Sugimoto, K.; Henry, D.; Li, Z.; Wahren, J.; Grunberger, G. C-Peptide Prevents and Improves Chronic Type I Diabetic Polyneuropathy in the BB/Wor Rat. Diabetologia **2001**, 44 (7), 889–897.

(12) Liu, Y.; Chen, C.; Summers, S.; Medawala, W.; Spence, D. M. C-Peptide and Zinc Delivery to Erythrocytes Requires the Presence of Albumin: Implications in Diabetes Explored with a 3D-Printed Fluidic Device. Integr. Biol. (United Kingdom)

2015, 7 (5), 534–543.

(13) Pinger, C. W.; Entwistle, K. E.; Bell, T. M.; Liu, Y.; Spence, D. M. C-Peptide Replacement Therapy in Type 1 Diabetes: Are We in the Trough of Disillusionment? Mol. Biosyst. **2017**, 13 (8), 1432–1437.

(14) Meyer, J. A.; Froelich, J. M.; Reid, G. E.; Karunarathne, W. K. A.; Spence, D. M. Metal-Activated C-Peptide Facilitates Glucose Clearance and the Release of a Nitric Oxide Stimulus via the GLUT1 Transporter. Diabetologia **2008**, 51 (1), 175–182.

(15) Wahren, J.; Foyt, H.; Daniels, M.; Arezzo, J. C. Long-Acting C-Peptide and Neuropathy in Type 1 Diabetes: A 12-Month Clinical Trial. Diabetes Care **2016**, 39 (4), 596–602.

(16) John, W. G.; Lamb, E. J. The Maillard or Browning Reaction in Diabetes. Eye **1993**, 7 (2), 230–237.

(17) Rahbar, S. The Discovery of Glycated Hemoglobin: A Major Event in the Study of Nonenzymatic Chemistry in Biological Systems. Ann. N. Y. Acad. Sci. **2005**, 1043, 9–19.

(18) Brownlee, M. Biology of Diabetic Complications. Nature **2001**, 414 (December), 813–820.

(19) Schmitt, A.; Nöller, J.; Schmitt, J. The Binding of Advanced Glycation End Products to Cell Surfaces Can Be Measured Using Bead-Reconstituted Cellular Membrane Proteins. Biochim. Biophys. Acta - Biomembr. **2007**, 1768 (6), 1389–1399.

(20) Brownlee, M.; Cerami, A.; Vlassara, H. Advance Glycosylation End Products in Tissue and the Biochemical Basis of Diabetic Complications. Semin. Med. Beth Isr. Hosp. Bost. **2010**, 318 (20), 1315–1321.

(21) Gautieri, A.; Passini, F. S.; Silván, U.; Guizar-Sicairos, M.; Carimati, G.; Volpi, P.; Moretti, M.; Schoenhuber, H.; Redaelli, A.; Berli, M.; et al. Advanced Glycation End-Products: Mechanics of Aged Collagen from Molecule to Tissue. Matrix Biol. **2017**, 59, 95–108.

(22) Goh, S.-Y.; Cooper, M. E. The Role of Advanced Glycation End Products in Progression and Complications of Diabetes. J. Clin. Endocrinol. Metab. **2008**, 93 (4), 1143–1152.

(23) Basta, G.; Schmidt, A. M.; De Caterina, R. Advanced Glycation End Products and Vascular Inflammation: Implications for Accelerated Atherosclerosis in Diabetes. Cardiovasc. Res. **2004**, 63 (4), 582–592.

(24) Barnaby, O. S.; Cerny, R. L.; Clarke, W.; Hage, D. S. Quantitative Analysis of Glycation Patterns in Human Serum Albumin Using16O/18O-Labeling and MALDI-

TOF MS. Clin. Chim. Acta **2011**, 412 (17–18), 1606–1615.

(25) Anguizola, J.; Matsuda, R.; Barnaby, O. S.; Hoy, K. S.; Wa, C.; DeBolt, E.; Koke, M.; Hage, D. S. Glycation of Human Serum Albumin. Clin. Chim. Acta **2013**, 425, 64–76.

(26) Hage, D. S. Analysis of Biological Interactions by Affinity Chromatography: Clinical and Pharmaceutical Applications. Clin. Chem. **2017**, 63 (6), 1083–1093.

(27) Matsuda, R.; Anguizola, J.; Joseph, K. S.; Hage, D. S. High-Performance Affinity Chromatography and the Analysis of Drug Interactions with Modified Proteins: Binding of Gliclazide with Glycated Human Serum Albumin. Anal. Bioanal. Chem. **2011**, 401 (9), 2811–2819.

(28) Baraka-Vidot, J.; Guerin-Dubourg, A.; Bourdon, E.; Rondeau, P. Impaired Drug-Binding Capacities of in Vitro and in Vivo Glycated Albumin. Biochimie **2012**, 94 (9), 1960–1967.

(29) Rondeau, P.; Bourdon, E. The Glycation of Albumin: Structural and Functional Impacts. Biochimie **2011**, 93 (4), 645–658.

(30) Pinger, C. W.; Heller, A. A.; Spence, D. M. A Printed Equilibrium Dialysis Device with Integrated Membranes for Improved Binding Affinity Measurements. Anal. Chem. **2017**, 89 (14), 7302–7306.

(31) Melten, J. W.; Wittebrood, A. J.; Willems, H. J. J.; Faber, G. H.; Wemer, J.; Faber, D. B. Comparison of Equilibrium Dialysis, Ultrafiltration, and Gel Permeation Chromatography for the Determination of Free Fractions of Phenobarbital and Phenytoin. J. Pharm. Sci. **1985**, 74 (6), 692–694.

(32) Barnaby, O. S.; Cerny, R. L.; Clarke, W.; Hage, D. S. Comparison of Modification Sites Formed on Human Serum Albumin at Various Stages of Glycation. Clin. Chim. Acta **2011**, 412 (3–4), 277–285.

Chapter 4 – Novel Applications of PolyJet 3D Printers

4.1 Background

4.1.1 Introduction

3D printers have become common in research, academic, and industrial settings over the last decade and are now becoming available to the public, with many printers available for use in public libraries. One printer that stands out above the rest is the PolyJet printer, which is currently made by Stratasys. Stratasys carries a wide selection of PolyJet printers ranging from desktop to large floor models. The mid- and high-grade PolyJet printers can print multiple materials and colors at resolutions down to 100 μm in the XY plane and layers as small as 14 μm in the Z-axis.[1] The PolyJet 3D printer utilizes UV curable polymers coupled with multiple print heads to combine both color and material properties into a single model.[1,2]

Users of 3D printers are utilizing these instruments to fabricate custom laboratory equipment for research purposes and as teaching aids.[3–7] These printed components come in a wide variety of complexity; for example, one of the more simple printed devices is a cap for a cell culture flask that allows for custom connections that enables cell culture media to be efficiently changed without opening the flask.[6] Another interesting application is the printing of 96-well plates with varying well geometries to test oxygen diffusion as a function of the well shape.[6] An example of more complex labware would be a plate reader compatible, 3D printed device for equilibrium dialysis (**Figure 4.1**).[8] This device was fabricated to accept interchangeable membranes based on molecular weight cut-off and can be analyzed directly in a plate reader. Researchers are utilizing 3D printers to aid in

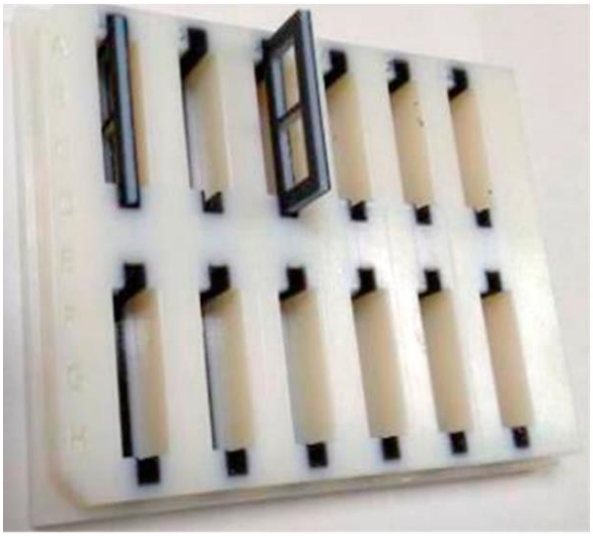

Figure 4.1: 3D printed plate for equilibrium dialysis. Incorporates custom made membrane windows that are compatible with a wide variety of membrane materials.[8]

in a variety of analytical determinations. For example, a group in the Netherlands has 3D printed a paper spray ionization cartridge to couple to a portable mass spectrometer.[9] Another system that has been 3D printed is the housing for a fluorometer.[10] The researchers were able to use an LED and a photocell coupled with a 3D printed housing to build their own fluorometer.[10] While these devices have technical applications, there is also a drive for other applications.

There have been 52 publications related to 3D printing in the Journal of Chemical Education from 2015 to present. The application of these publications range from facilitating visual instruction to hands-on devices for use in the laboratory.[10–13] One of the more notable applications is a 3D printed chromatogram that monitors the synthesis of a small molecule over time to show students how the peak disappears and a new peak fills in.[12] Additional examples include printed models that show copolymer morphologies and

potential energy diagrams.[11,13] Having students design and print these structures adds another layer to their understanding.

Outside of traditional classrooms, 3D printed models also have applications in teaching and planning in the medical field.[14–18] To this end, physicians have worked towards printing models of various regions of the body. This includes simulated bones, hearts, and tumors. Possession of a physical model prior to surgery enables physicians to practice procedures and decide on surgical plans. These models have been printed to facilitate bone reconstruction, as well as brain surgery.[6,18] The models used in these visual aids and surgery prep are exact replicas of the patient's anatomy made from scans of the patient.[14]

4.1.2 Motivation for this Work

Having access to a high end commercial grade 3D printer allows for the development of other tools and labware tangentially related to diabetes and diabetic complications. In this chapter other tools will be showcased that advance scientific endeavors. Specifically, a multi-channel 3D printed peristaltic pump will be described. Additionally, work done to advance surgical planning with congenital heart specialists at Spectrum Health Helen DeVos Children's Hospital located in Grand Rapids, MI will be discussed.

In the previous chapters, the focus has been the utilization of 3D printers to learn more about the biological activity of C-peptide. While previous work in the Spence group coupled with the work shown previously does a good job of validating C-peptide as an important molecule biologically. In discovering the how C-peptide functions throughout

the body, it was discovered that zinc is vital in the successful formulation C-peptide. In vivo, the zinc is stored and secreted at the same time and place as C-peptide. This means that tracing the zinc on a platform like that proposed in Chapter 2 will become vital. To this end, radioactive zinc (^{65}Zn) is a logical choice because it can be easily tracked and quantified both intracellularly and in solution. In order to introduce zinc into the system the Rat INS1 cells can be grown to confluence with ^{65}Zn in the growth media. These cells will then incorporate the ^{65}Zn into vesicles within the β-cells and will be released when C-peptide and insulin are released into the system.

Dealing with radioactive substances presents a new level of safety concerns. First and foremost, the exposure to the researcher should be limited. Secondly, possible contamination to expensive equipment should be minimized. To this end a system for handling radioactive solutions would be needed. The system would need to be automated or remote controlled and cheap enough to be considered disposable if contaminated. Utilizing 3D printers and commercially available microcontrollers this is both feasible and realistic and will be discussed later.

Commercial grade, high resolution, 3D printers have additional applications that are only now being realized. In collaboration with Spectrum Health Helen DeVos Children's Hospital located in Grand Rapids, MI, complex medical scan data is being converted into 3D printable data. With this, doctors can get hands on experience with the complications or defects they are about to operate on or treat. While these types of scans and printable objects are currently relegated to the microvasculature, as scanning systems and printing systems become more advanced, researchers should be able to scan and print components of the microvasculature. Since the Spence group has

expertise in growing and manipulating cell lines associated with the vasculature it is important to being involved in advancing all research that could lead to better biomimetic systems. To this end, we have joined with doctors to advance the printing of patient hearts and heart defects for surgical preparations and planning.

4.2 3D Printed Multichannel Peristaltic Pump

4.2.1 Methods

4.2.1.1 Designing Files for 3D Printing

All the devices mentioned in this section were printed on either an Objet Connex 350 (Stratasys Ltd, Eden Prairie, MN) located in the Department of Electrical and Computer Engineering at Michigan State University or a Stratasys J750 (Stratasys Ltd,) located in the Institute for Quantitative Health Science and Engineering (IQ) at Michigan State University. Designs of the peristaltic pump were drawn in Autodesk Inventor Professional 2017 (Autodesk, Inc., San Francisco, CA), a CAD software package available free to students. All of the models were printed in one of the following hard plastics: VeroClear, VeroWhite, VeroCyan, VeroYellow, VeroMageneta, or VeroBlack. The models printed on the Connex 350 utilized the Fullcure SUP705. Models printed on the J750 were printed with SUP706B, a caustic soluble support material. While all of these materials are proprietary to Stratasys, properties can be found on their website, www.stratasys.com. Each component was printed in a matte finish and coated in support material in order to provide a uniform surface finish to each piece.

The pump was designed in 4 different parts shown in **Figure 4.2** and annotated in **Figure 4.3**, namely, the pump housing, inner rotor, roller, and rotor bottom. The pump

housing was the largest component at 50 x 50 x 51.5 mm. The rotor was designed to fit loosely within the pump housing with a diameter of 44.5 mm. The rotor has 8 pins with a diameter of 6 mm to hold the rollers, and the pins are designed to pressure fit into the holes on the rotor bottom. The roller pins are designed to loosely fit over the pins. The rollers have an inside diameter of 6.5 mm and an outer diameter of 11.50 mm.

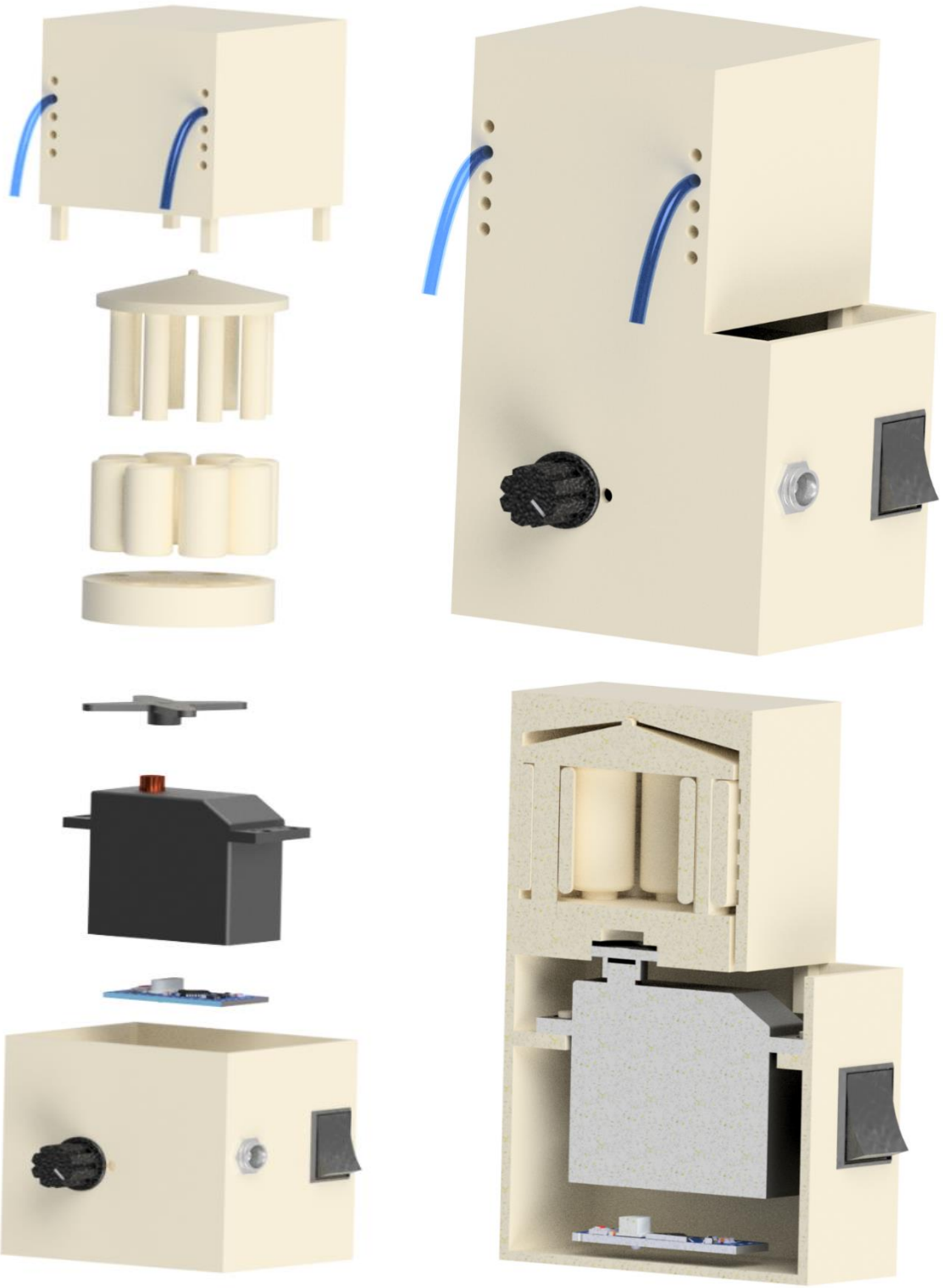

Figure 4.2: CAD illustration of the assembled peristaltic pump with servo motor and Arduino board.

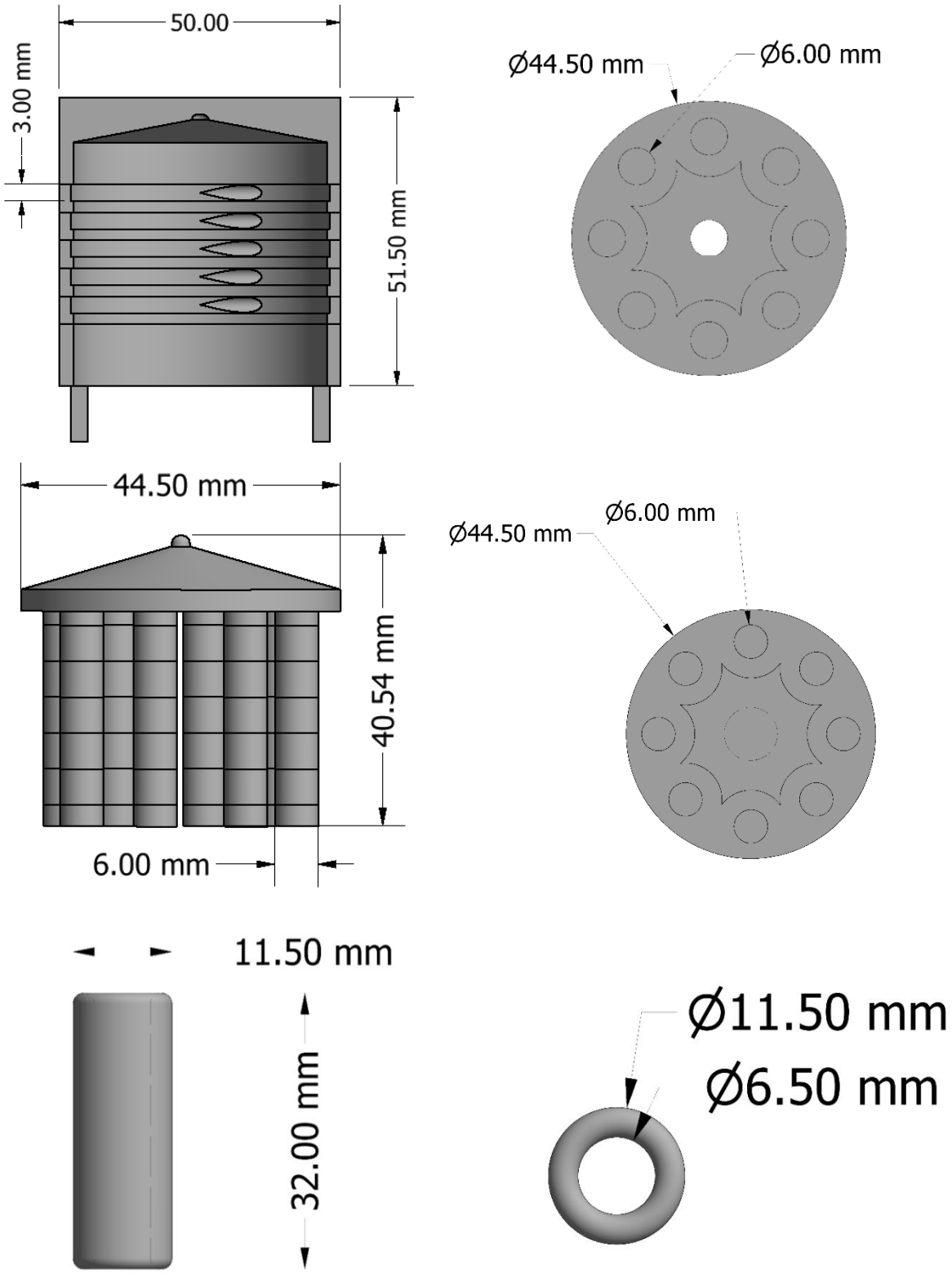

Figure 4.3: Dimensions of the 3D printed peristaltic pump.

4.2.1.2 Pump Post Processing

The parts printed on a PolyJet 3D printer used a soft support material, either SUP705 on the Objet, or the caustic soluble SUP706B on the J750. Parts printed with the SUP705 support material were cleaned by removing the bulk of the material by hand. Remaining support material was removed by a high-pressure water jet system (Powerblast, Balco, UK). The rollers, roller pins, and interior of the pump housing were then wet sanded with 1500 grit wet/dry sand paper until a glossy smooth finish was achieved. Parts printed with SUP706B underwent the same steps in addition to a one-hour soak in a 2% sodium hydroxide solution after the pressure washing step, but before the sanding procedure.

4.2.1.3 Additional Pump Components

The pump was assembled and run with a small, continuous rotation servo motor (SM-S4315R, SpringRC, China). This servo motor has a maximum torque of 15.1 kg • cm with a maximum speed of 0.21 RPM. An Arduino Pro Mini was used to control the servo motor. Both the servo and the Arduino board were powered by a 6V rechargeable battery. A DC plug was incorporated into the part with an on/off switch. For characterization purposes, the Arduino was manually programed to run at specific speeds. With this design, the Arduino board must be removed from the housing for reprograming. For functional or in-field work, a potentiometer can be wired to the Arduino board to allow for variable speed without reprogramming the board.

4.2.2 Results

4.2.2.1 Channel Reproducibility

The pump was characterized by measuring flow rate at different motor speeds. To measure the reproducibility over the five channels, water was pumped into 5 different tubes whose mass was premeasured. After 5 minutes of flow (**Fig 4.4**), a new mass measurement was obtained. This was performed five times for each channel. The data shows that there is no significant difference in flow rate across the five channels. The average flowrates (± standard deviation) at pulse widths of 1600, 1650, 1700, and 1750 µs are 0.457 ± 0.028, 1.065 ± 0.035, 1.252 ± 0.032, and 1.367 ± 0.055 mL/min,

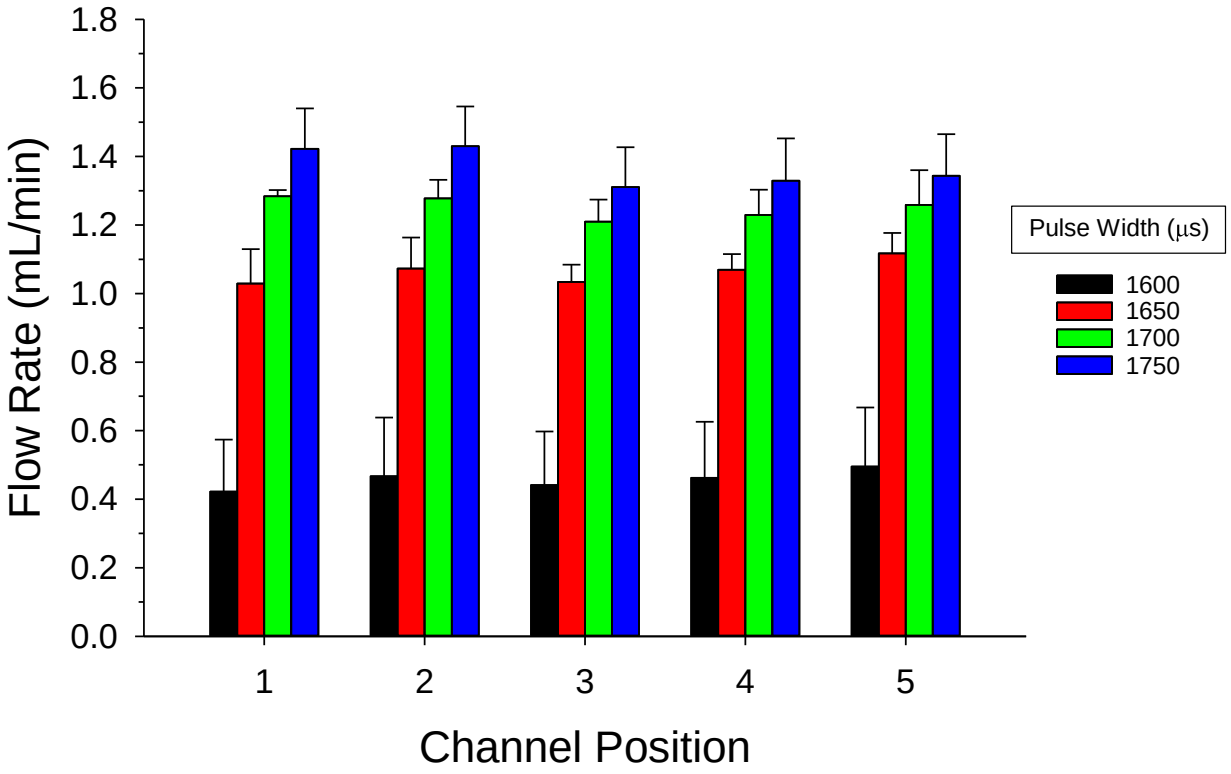

Figure 4.4: Bar plot of each channel in the pump at varying motor speeds specified by the PWM signal in microseconds. Number on the channels starts farther away from the motor and increases as it moves towards the motor. N=5 Error= Standard Deviation

respectively. There are no significant outliers across the four flow rates measured. It should be noted that the channels were numbered from the top to bottom with the top being furthest away from the servo motor.

4.2.2.2 Long Term Reliability

In order to determine the long-term stability of the pump, the pump was operated continuously, with the exception of a few seconds to replace the battery twice, for 24 hours, with a pulse width of 1625 µs. To directly measure the flow rate, a LabVIEW program was created to interface the balance with a computer and to log the mass as a function of time. To prevent damage to the balance, data was taken for 5-minute intervals

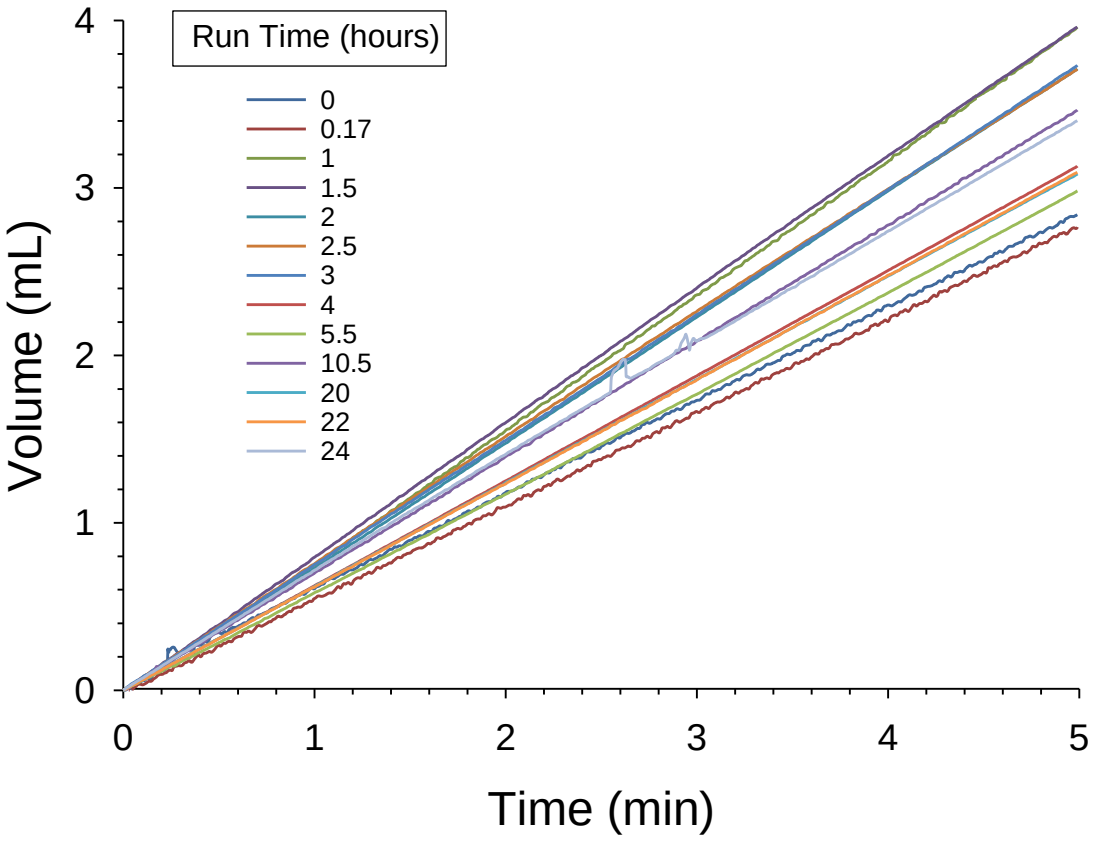

Figure 4.5: Plot of volume dispensed on a balance as a function of time for channel 3 of the 3D printed peristaltic pump.

over the course of a day (24 h). **Figure 4.5** shows the plot of the continuous 5-minute intervals for each of these time points. The slope of this data is equal to the flow rate. The average flow rate for the 24-hour tested period was 0.68 ± .05 mL/min, and the plot of the flow rate over time can be seen in **Figure 4.6**. It is interesting to note that there is a

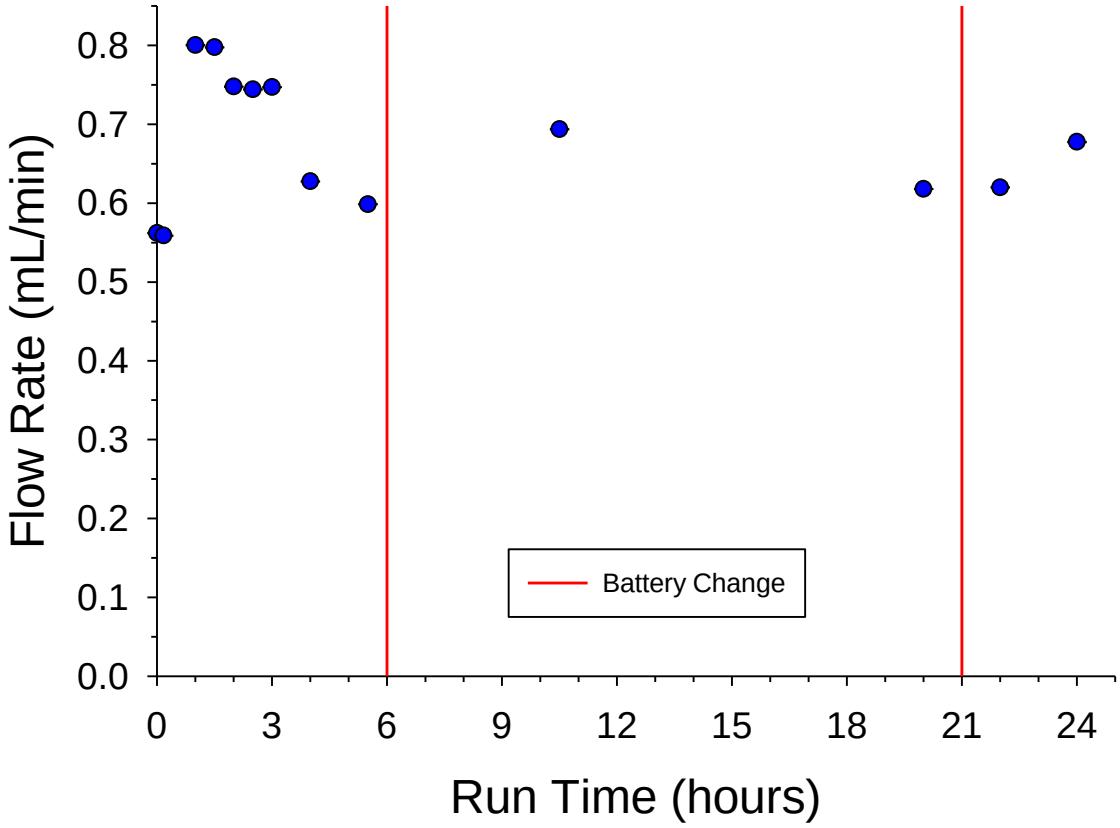

Figure 4.6: Plot of measured flow rate over 24 hours of continuous use. Note that the battery controlling the pumping system was switched out two times to ensure that no fluctuations in the measured flow rate were due to decreasing voltage of the battery.

downward trend in the first 5 hours then relative stabilization after the battery change. Since the speed of a servo motor depends on the voltage of the battery, it is plausible that the drop-off seen at that point is from a dying battery.

4.2.3 Discussion

A functional, 3D printed, multichannel, peristaltic pump is designed and fabricated that can reach flow rates of 0.4 to 1.4 mL/min. This pump, like most peristaltic pumps, could have an expanded flow rate window by changing the tubing to various different internal diameters. Additionally, this design could be expanded to include more channels. However, it should be noted that a more powerful motor would be required to run a pump with more channels. For this design, the motor was already at its upper limits of performance.

This pump worked continuously for 24 hours without showing a significant drop in flow rate for the middle channel. However, this device did not progress through that time frame without significant wear and damage. The system experiences a high degree of friction even after being polished smooth. Due to this friction, the servo motor has to work

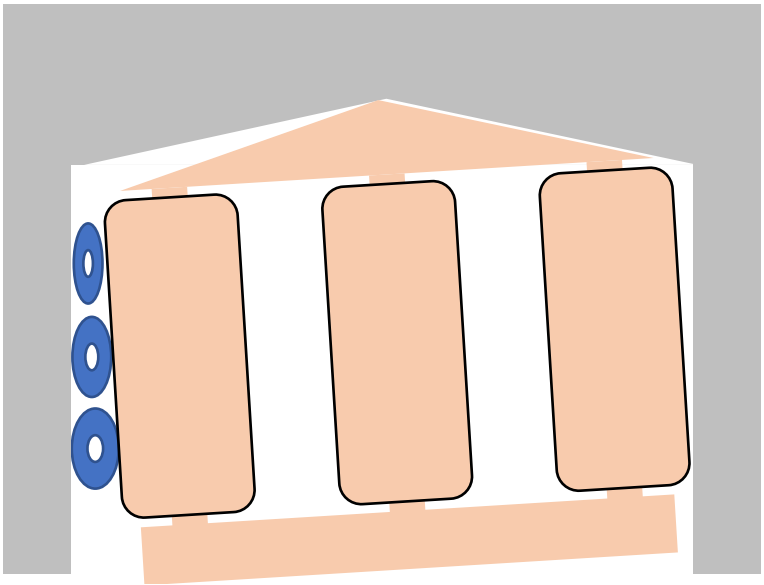

Figure 4.7: Exaggerated illustration of the way the inner roller sits within the housing when the tubing is put into the system. This misalignment causes wear to the bottom of the roller leading to loss of compression on the bottom channel.

very hard to maintain the pumping action. This leads to the servo motor creating a lot of heat. The Vero line of material, used in this pump, experiences softening at temperatures above 115°F. No temperature readings were taken during the experiment, but at the end of the 24-hour period, both the base and the main housing showed signs of warping. The warping on the base was probably due to the torque. At the end of the 24 h period, the fifth channel was no longer able to deliver fluid. This is due to excess wear on the bottom section of the rollers caused by the inner roller sitting at an angle within the housing. **Figure 4.7** shows an exaggeration of how the housing is misaligned when tubing is inserted. This misalignment leads to an inefficient occlusion for the bottom two channels, as well as increased wear to the pumping system. With this in mind, a new version of the pump was designed with the goal of preventing this wear and creating a pump with less friction. **Figure 4.8** shows the design of the new pump. This pump utilizes a planetary gear system to hold the rollers in place and prevent the misalignment seen in the old design. Due to the resolution of J750, a larger pump had to be designed. The new dimensions of the 3-port version were 70 x 70 x 47 mm. While this device did function, it did not exhibit the expected reduced friction. However, it did perform adequately for proof of concept.

This design incorporates additional design features that could be beneficial and could incorporate as few as 2 or as many as 6 rollers. The number of rollers is one factor in controlling the amount of pulsation seen within the system. More rollers equate to a smoother pumping action, but also increase the friction on the system. This pump can be easily modified for different experiments. The other advantage with this pump is the Particle Photon board that was used in place of the Arduino.

The Particle Photon is very similar to the Arduino micro in that it is a programmable microcontroller. The benefit of the Photon is the built in Wi-Fi capabilities. Along with the Wi-Fi capabilities, the Particle company also has built-in infrastructure for controlling their boards wirelessly from a desktop or a smart phone. This allows the user to remotely program the device, turn the pump on or off, or change the speed. Additional functionality could include remote cell feeding within an incubator or in high level biohazard labs. This would decrease the likelihood that researchers would be exposed to hazardous

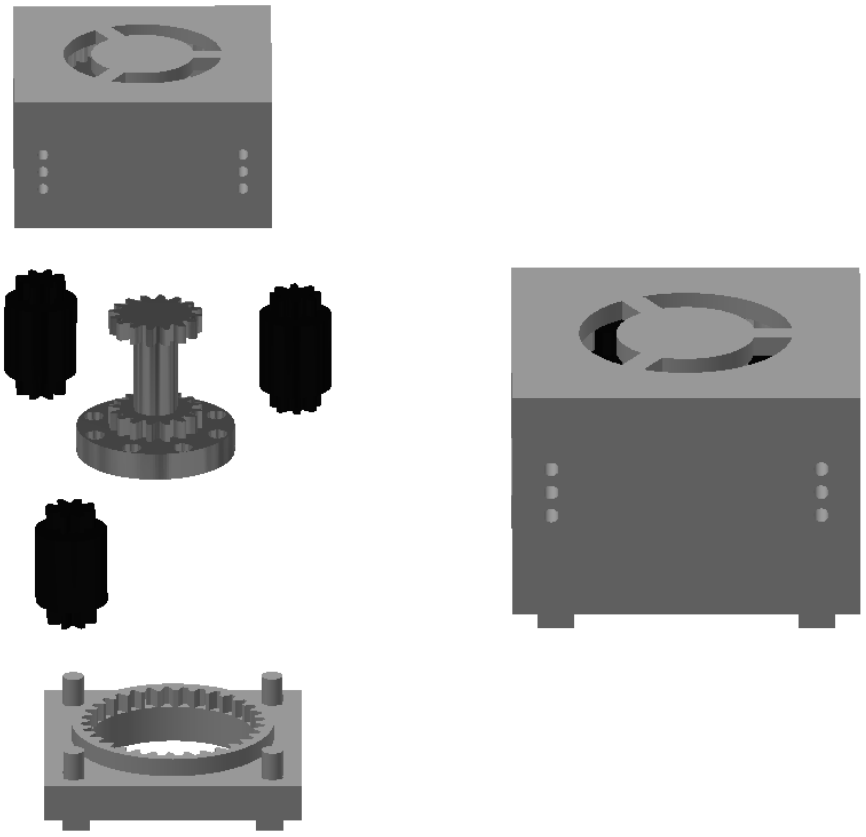

Figure 4.8: Concept for a new 3D printed peristaltic pump. This pump utilizes a planetary gear system to hold the rollers in perfect alignment regardless of pressure from the tubing. This system can also utilize varying number of rollers.

conditions, such as pathogenic organisms. Since the total cost of the pump is under $150, there is also less financial burden if the pump is contaminated and must be replaced.

4.3 3D Printing Hearts

The Stratasys J750 was utilized for collaboration with the Spectrum Health Helen DeVos Children's Hospital Catheterization Laboratory whose staff was using medical imaging techniques and data to convert images of patients' hearts into 3D printable files. For the last several years, the Spectrum staff had been printing monochromatic and translucent models and were hoping to start printing files in multiple colors and with varying material properties. To facilitate this process, it is important to understand how the files are converted to proper file formats prior to printing; these methods are discussed below in section 4.3.1.

4.3.1 Methods

4.3.1.1 3D Printing

All devices described in this section were printed on the Stratasys J750 (Stratasys Ltd) located in the IQ facility. All of the models were printed in one or more of the following hard plastics or simulated rubbers. The hard plastics consisted of either VeroClear, VeroWhite, VeroCyan, VeroYellow, VeroMageneta, VeroBlack, or MED610, while the simulated rubbers consisted of either Tango+ or Agilus30.

4.3.1.2 Converting Medical Imaging Data to 3D Printable Files

Medical imaging data, such as a CT scan, is saved as a DICOM file. The DICOM file format is the generic format used by the medical industry because it encodes data

about the patient, data about the machine used to take the image, and the images from the scan. The ability to convert the data into more visually appealing formats is a relatively new technology and has mostly existed in the realm of virtual reality. However, with the 3D printer revolution, there has been a push to 3D print these scans. The conversion process has mostly been a manual process, but researchers are working to automate the process for mainstream use. The process for converting a CT scan of an object or animal, such as a mouse, for 3D printing is a generic procedure and can be applied to almost any scan data.

The software Materialise Mimics (Materialise, Belgium) was used to perform the conversion and segmentation of the scan data. The Mimics software can read DICOM files and display the data. The interface looks similar to a typical scan display where all three axis cross sectional areas are displayed. For CT scans, the process can be slightly automated based on the Hounsfield units, which are relative attenuated intensities using pure water as the baseline.[19] Since the Hounsfield units are normalized, there are specific ranges that have been correlated to various tissue types, and even some foreign objects. The CT scans can be segmented by these values to show only the bone or soft tissue. Manually affecting the scan/file can occur if differentiating parts of the bone for colorization is desired. This requires the researcher to manually separate the two bones in every segment. Once all the desired features have been segmented, each component can be exported as a .STL file with the same origin points.

4.3.2 Results

4.3.2.1 Learning Mimics Software

To implement this process in our labs, CT files were obtained. with the goal of monitoring implants placed within the hindquarters of a mouse. **Figure 4.9** shows the results of this endeavor. **Figure 4.9(A-C)** are the CAD representation of the different segmentations. With **(A)** being the soft tissue, **(B)** the skeletal structure, and **(C)** the implants. While converting the mouse CT to this form was easy in comparison to the heart (shown later), using the software allowed us to explore options for exporting the files in

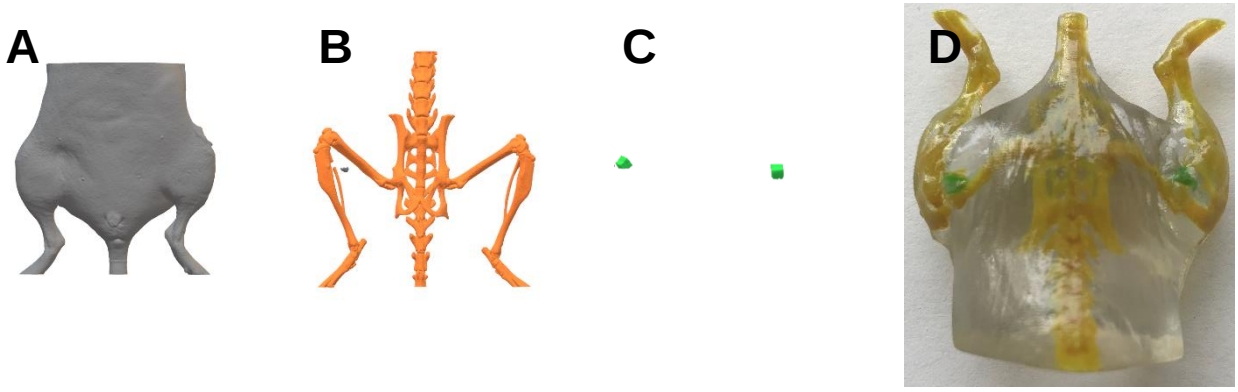

Figure 4.9: CAD representations of the segmented portions of the mouse model. (A) segmented section of the mouse's soft tissue. (B) segmented section of the mouse's skeletal system. (C) segmented section of the Tantalum implants. (D) picture of the final model.

order to print the heart models on the J750 in ways that would be beneficial to the doctors. **Figure 4.9D** is the finished product where the soft tissue was printed in clear, the skeletal system printed in yellow, and the implants printed in green

4.3.2.2 Example Hearts

Several different hearts were printed to illustrate the capabilities of the printer and to explore defects that could be detected by visual inspection with this style of printing. **Figure 4.10** shows a solid fill heart that was segmented into six parts. The lower

chambers of the heart were printed in green and purple while the heart walls associated with this area were printed in clear to enable visual inspection of the space within the heart. The important features on this heart are the pulmonary arteries, the pulmonary veins, and the aorta. These are the complex branched structures seen in the top left of the left panel of **Figure 4.10**. When these structures are printed on a PolyJet printer, they

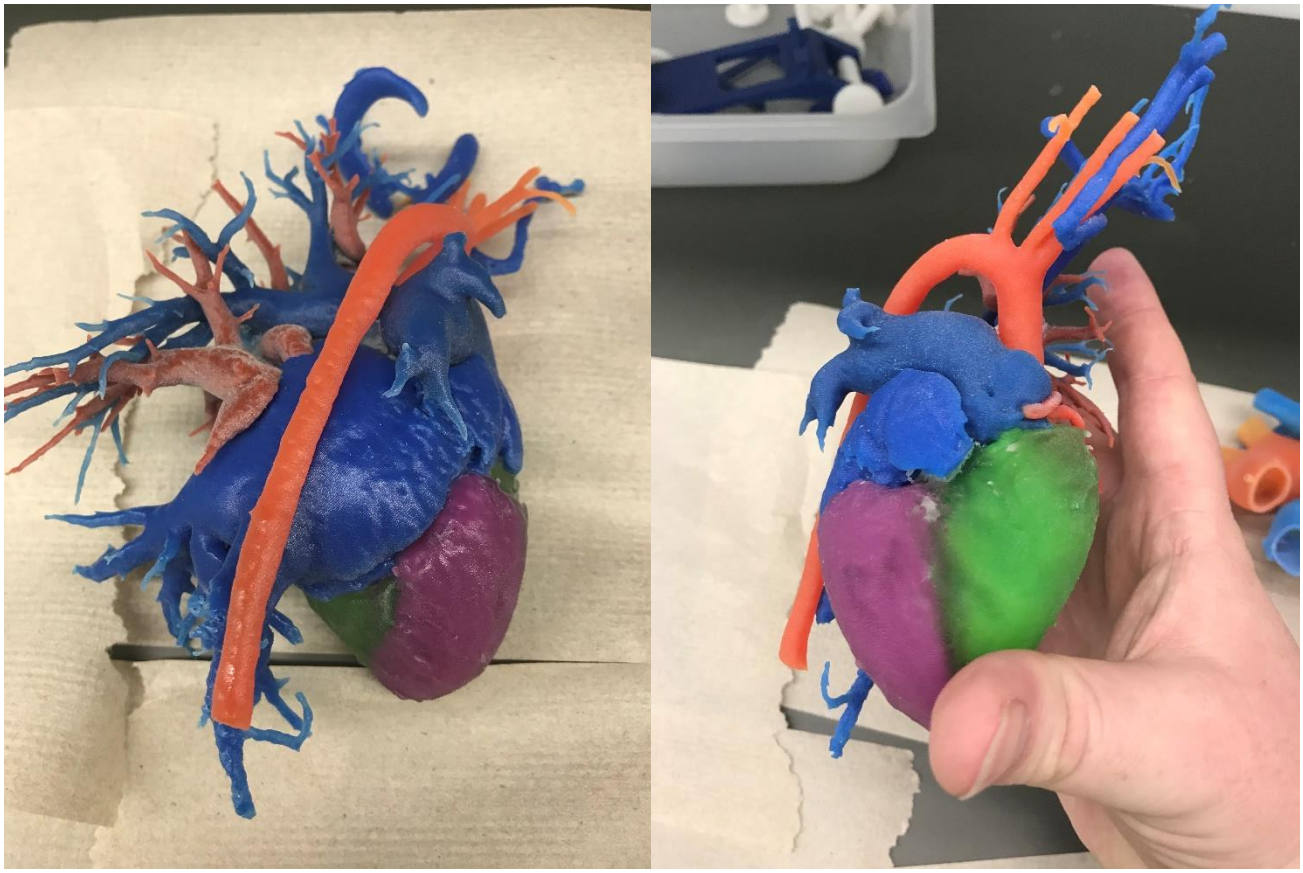

Figure 4.10: Pictures of a solid 3D printed heart. This heart was printed to show how durable the material can be and to the explore the fine detail that can be seen in the blood vessel network close to the heart.

are completely encased in the support material. Fortunately, these structures could be cleaned without damage.

Figure 4.11 shows a highly segmented healthy human heart. The goal of this print was to explore printing a heart with a cavity to observe defects within the heart. While the detail that could be achieved with this high degree of segmentation was quite high, there

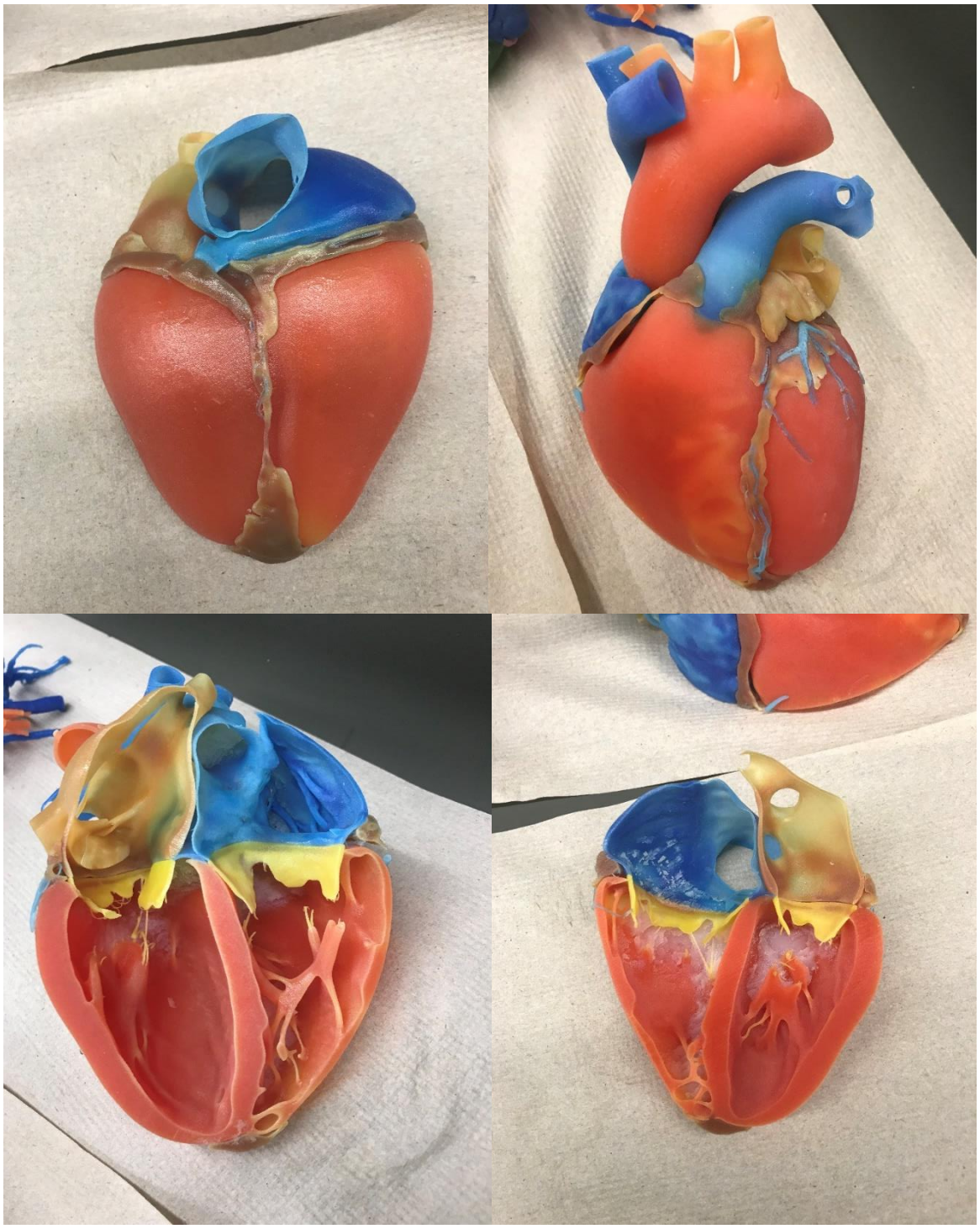

Figure 4.11: A highly segmented healthy heart. As can be seen in the bottom right panel, not all of the support material has been removed, but all of the chordae tendineae have been broken off.

were issues with the print. Specifically, some of the ultrafine detail was not retained such as the chordee tendineae, which are tissue that connects muscles within the heart to the

heart valves. Experts have long been interested in visualizing this section of the heart because of various heart conditions that affect this region of the heart.

4.3.2.3 Heart for Surgery Prep

A clear, defective heart was printed for testing with a custom-made stent. The heart was segmented by the physicians at the Helen DeVos Children's Hospital in Grand Rapids, MI. The file was then sent to Michigan State University, where printing and post processing were completed. This heart was printed to scale in a flexible material (Shore 40). The flexibility of the material closely mimics how the heart responds to the stent

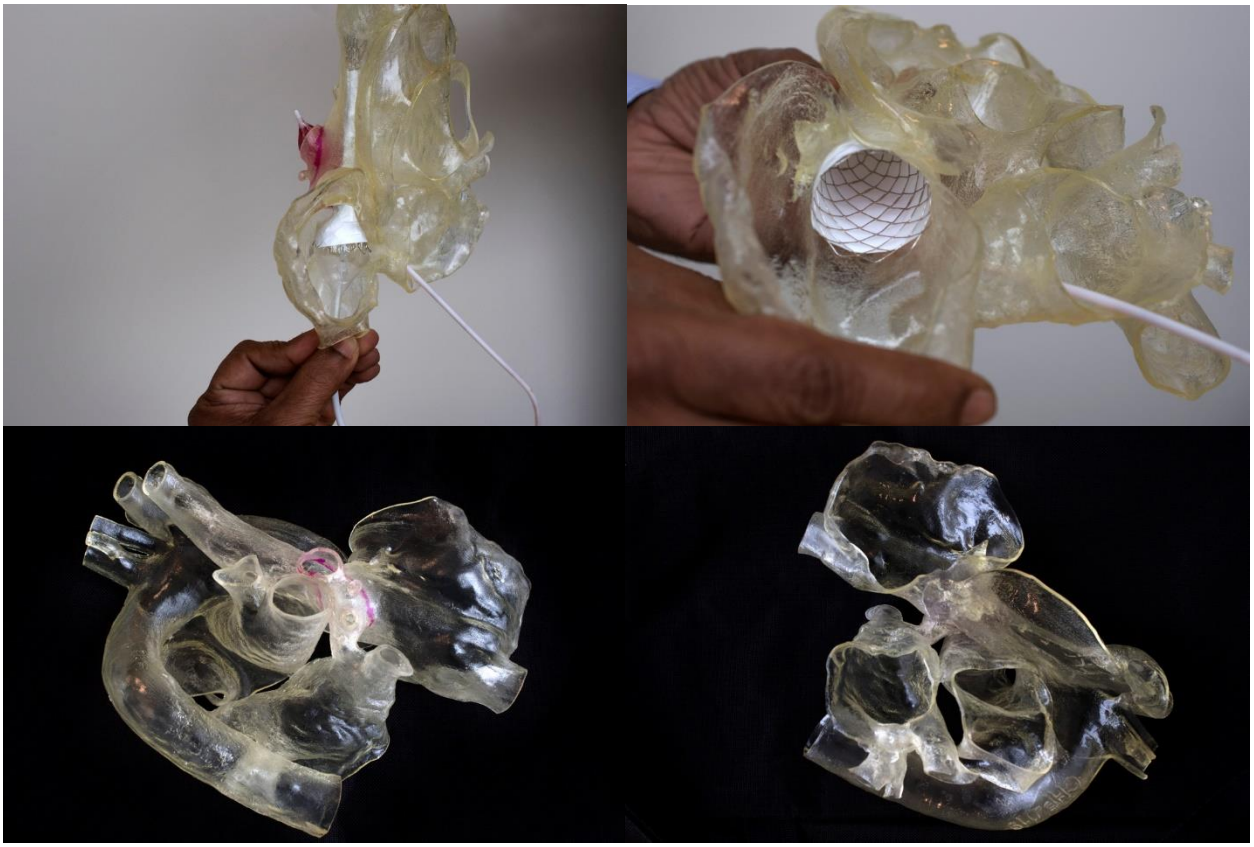

Figure 4.12: A transparent heart for testing a custom-ordered non-sterile stent. The top two panels show the physician practicing the stent placement on the 3D printed model. The bottom two panels show the heart after the practice procedure was performed. It is important to note that the physician was able to deploy the custom stent and the model was able to with stand the pressures of the procedure.

placement within the body. **Figure 4.12** shows the collaborating physician practicing the stent placement. It should be noted that this heart was printed with a wall thickness of 1.5 mm, thinner than generally accepted thickness of the heart, but at this thickness the material gave a good representation of the properties of an actual heart.

4.3.3 Discussion

Dr. Vettukattil, the lead physician on the project, requested a clear model of a defective heart be printed. His hope was that the heart would closely mimic the flexibility and durability of the heart. The doctor was custom ordering a stent to insert into the patient's heart via catheter. This stent would be used to seal a hole between two sections of the heart. After printing some samples, it was decided that a blend of the commercially available Agilus30 and VeroClear, specifically FLXA9940-DM with a shore value of A-40 had the optimum material properties. Some testing was done on small sections of the heart to determine the minimum wall thickness required for this material to survive the cleaning procedure. It was determined that 1.5 mm would suffice and a full model was printed. The full model allowed Dr. Vettukattil and his team to practice the procedure and test a non-sterile version of the custom stent. They have reported that the stent was able to be deployed into the device in the same way that it was in the actual procedure thus aiding in a successful operation, and the development of novel procedure.

While this is only one case study for the application of 3D printing in surgical applications, Dr. Vettukattil's group is not the only group advancing this research. Several groups around the world are using 3D printers to help improve both recovery time and surgical outcome. One of the major limitations with advancing this research is funding. Segmenting the heart or any other organ into a printable model with useful information is

a time consuming and laborious process. Plus, printing a full-size heart can take over 48 hours and cost over one thousand dollars. To this end, there are currently studies being conducted to prove that these 3D printed models increase patient recovery and surgery outcomes.

REFERENCES

REFERENCES

(1) Gross, B.; Lockwood, S. Y.; Spence, D. M. Recent Advances in Analytical Chemistry by 3D Printing. Anal. Chem. **2017**, 89 (1), 57–70.

(2) Tibbits, S. 4D Printing. Archit. Des. **2014**, 84 (1), 116–121.

(3) Whitehead, H. D.; Waldman, J. V.; Wirth, D. M.; LeBlanc, G. 3D Printed UV-Visible Cuvette Adapter for Low-Cost and Versatile Spectroscopic Experiments. ACS Omega **2017**, 2 (9), 6118–6122.

(4) Coakley, M.; Hurt, D. E. 3D Printing in the Laboratory: Maximize Time and Funds with Customized and Open-Source Labware. J. Lab. Autom. **2016**, 21 (4), 489–495.

(5) Baden, T.; Chagas, A. M.; Gage, G.; Marzullo, T.; Prieto-Godino, L. L.; Euler, T. Open Labware: 3-D Printing Your Own Lab Equipment. PLoS Biol. **2015**, 13 (3), 1–12.

(6) Lücking, T. H.; Sambale, F.; Beutel, S.; Scheper, T. 3D-Printed Individual Labware in Biosciences by Rapid Prototyping: A Proof of Principle. Eng. Life Sci. **2015**, 15 (1), 51–56.

(7) Johnson, R. D. Custom Labware: Chemical Creativity with 3D Printing. Nat. Chem. **2012**, 4 (5), 338–339.

(8) Pinger, C. W.; Heller, A. A.; Spence, D. M. A Printed Equilibrium Dialysis Device with Integrated Membranes for Improved Binding Affinity Measurements. Anal. Chem. **2017**, 89 (14), 7302–7306.

(9) Salentijn, G. I.; Oleschuk, R. D.; Verpoorte, E. 3D-Printed Paper Spray Ionization Cartridge with Integrated Desolvation Feature and Ion Optics. Anal. Chem. **2017**, acs.analchem.7b02490.

(10) Porter, L. A.; Chapman, C. A.; Alaniz, J. A. Simple and Inexpensive 3D Printed Filter Fluorometer Designs: User-Friendly Instrument Models for Laboratory Learning and Outreach Activities. J. Chem. Educ. **2017**, 94 (1), 105–111.

(11) Scalfani, V. F.; Turner, C. H.; Rupar, P. A.; Jenkins, A. H.; Bara, J. E. 3D Printed Block Copolymer Nanostructures. J. Chem. Educ. **2015**, 92 (11), 1866–1870.

(12) Higman, C. S.; Situ, H.; Blacklin, P.; Hein, J. E. Hands-On Data Analysis: Using 3D Printing to Visualize Reaction Progress Surfaces. J. Chem. Educ. **2017**, 94 (9), 1367–1371.

(13) Kaliakin, D. S.; Zaari, R. R.; Varganov, S. A. 3D Printed Potential and Free Energy

Surfaces for Teaching Fundamental Concepts in Physical Chemistry. J. Chem. Educ. **2015**, 92 (12), 2106–2112.

(14) Mcmenamin, P. G.; Quayle, M. R.; Mchenry, C. R.; Adams, J. W. The Production of Anatomical Teaching Resources Using Three-Dimensional (3D) Printing Technology. Anat. Sci. Educ. **2014**, 7 (6), 479–486.

(15) Tam, M. D. B. S.; Laycock, S. D.; Brown, J. R. I.; Jakeways, M. 3D Printing of an Aortic Aneurysm to Facilitate Decision Making and Device Selection for Endovascular Aneurysm Repair in Complex Neck Anatomy. J. Endovasc. Ther. **2013**, 20 (6), 863–867.

(16) Klein, G. T.; Lu, Y.; Wang, M. Y. 3D Printing and Neurosurgery--Ready for Prime Time? World Neurosurg. **2013**, 80 (3–4), 233–235.

(17) Waran, V.; Narayanan, V.; Karuppiah, R.; Owen, S. L. F.; Aziz, T. Utility of Multimaterial 3D Printers in Creating Models with Pathological Entities to Enhance the Training Experience of Neurosurgeons. J. Neurosurg. **2014**, 120 (2), 489–492.

(18) Jariwala, S. H.; Lewis, G. S.; Bushman, Z. J.; Adair, J. H.; Donahue, H. J. 3D Printing of Personalized Artificial Bone Scaffolds. 3D Print. Addit. Manuf. **2015**, 2 (2), 56–64.

(19) Schneider, U.; Pedroni, E.; Lomax, A. The Calibration of CT Hounsfield Units for Radiotherapy Treatment Planning The Calibration of CT Hounsfield Units for Radiotherapy Treatment Planning. Phys. Med. Biol. **1996**, 41, 111–124.

Chapter 5 – Overall Conclusions and Future Works

5.1 Conclusions

3D printing is rapidly becoming commonplace within research laboratories.[1–7] The commercially available 3D printers offer a wide range of materials: rubber, hard plastic, metals, biomaterials, and more.[6,8–10] This wide selection in material allows researchers to customize devices for every need and application. However, the printers with the best resolution have the most restrictions on material properties and the printers with the widest array of materials have poor resolution.[11,12] Furthermore, each type of printer has different resolution options; thus, it is difficult to print multiple parts from different printers with different materials and fit them together.

Resolution is also limited by the properties of the material type. These limitations are troublesome for research involving microfluidics and bioapplications, specifically research involving mammalian cells. The available resolution for most printers does not allow one to truly mimic blood flow in the body, as the required channels would need to be as small as 10 μm. While larger diameter channels are easily achievable, most printers are limited to around 500 μm at the lower limit.[11–13] This limit in feature size is compounded by the need to support the model as it is being printed (that is, the use of a support material). Some techniques like SLA mentioned in chapter 1 do not require support material in the channels, but SLA can only incorporate one material per device and is very time consuming. Polyjet, on the other hand, can incorporate multiple materials and is a rapid printing technique, but utilizes a soft sacrificial support material that is laid within the channel during the print process.[2,14,15] This support material must be removed after the print job is completed. This can be complicated and time consuming if the

channel size is small or the channel geometry is complex. This thesis shows that despite these limitations, 3D printing can be a versatile tool to push the boundaries of scientific research.

5.1.1 Selective Cell to Cell Communication

Understanding the complex dynamics of in vivo systems has been a goal of researchers for decades.[16,17] The body utilizes numerous signaling molecules to initiate complex mechanisms in the body. Understanding how these mechanisms are initiated is vital to the treatment and prevention of many diseases. Traditionally, scientists utilize knockdowns, knockouts, and knock ins to selectively explore mechanisms within cells and animals and how certain chemicals react throughout a biological system.[18–20] Other methods include the introduction of chemical stimuli to activate a receptor or block a receptor from being activated. Often with knockdown systems, the act of modifying the cell to stop production or transmission of a particular analyte will lead to undesirable affects elsewhere in the cell, sometimes resulting in unwanted up-regulation or down-regulation of other chemicals or hormones.[21]

Chapter 2 describes a new platform for exploring cell to cell communication. This platform can be used to explore cell to cell communication on unmodified cells. Specifically, this device was developed to study the communication between adherent cell lines and flowing red blood cells. The device utilizes compartments separated by membranes that contain either cells or antibody-modified beads. The modified beads used have been shown to capture either Zn^{2+} or C-peptide. This device is designed to be a platform technology used to study a variety of systems, as the beads can be modified

with various antibodies that could be used to pull out one or more specific target analytes between cell types.

Technology to selectively determine the function of biomolecules is needed to push a C-peptide therapeutic to the final stage. The Spence group, as well as others, have shown strong evidence to support that the introduction of C-peptide into the body under proper conditions will directly or indirectly lead to the increased production of nitric oxide (NO).[22–27] The increase in NO leads smooth muscle relaxation, vasodilation, and ultimately improved blood flow. This has translated well to rat studies. Rat studies have shown positive effects from C-peptide on nerve function most likely through increased blood flow in the small arteries that supply blood to the peripheral nerves.[25,27] There have even been human trials, one of which lasted 12 months, that have shown the same positive effects, but to a diminished extent.[28,29] This has raised a debate about what the proper formulation and delivery mechanism should be for C-peptide. With the ability to flow RBCs and selectively stimulate them for communication with other cell lines the proposed formulations can be explored in a systematic way.

5.1.2 3D Printed Devices for Protein Binding Characterization

Carrier proteins, such as albumin, are used in the body to distribute small molecules to different cell types and tissues.[30–32] These proteins can undergo post translational modifications which can alter their function. Glycation, a post translational modification resulting from reaction of a molecule of glucose with a terminal amine group of a protein, occurs in people with diabetes at an increased occurance.[33–35] The modification becomes more prevalent after longer term exposure to increased levels of glucose in the bloodstream, such as conditions seen in Type 1 and Type 2 diabetes.[35]

This prolonged exposure leads to the formation of advanced glycation end products (AGEs). It has been documented in the literature that these modifications lead to changes in functionality for proteins that undergo these modifications.[30,36–39] It is hypothesized that these changes in functionality may result in downstream complications in patients with diabetes.

In order to explore the effects of glycation on protein function, two different custom ultrafiltration devices were 3D printed. The first device is a pressure driven syringe platform, which can incorporate any type of membrane, allowing the user to choose both material and pore-size. Membranes utilized in this device include polycarbonate and cellulose. Utilizing the cellulose membranes, it was determined that glycated human serum albumin (gHSA) binds Zn^{2+} differently than normal human serum albumin (nHSA). Specifically, nHSA was shown to bind more Zn^{2+} than gHSA. This may explain problematic zinc homeostasis and hyperzincuria, or the excess Zn^{2+} secreted through the urinary track seen in diabetic patients. This device performed adequately and yielded results consistent with literature values. The syringe-device had limitations when attempting to do large numbers of samples, specifically in the form of a failure rate from leaking around the threaded connection, leaking around the membrane O-ring, or breaking of the membrane. The second device was based on commercially available centrifugal filter units. This device was printed as one continuous piece with an embedded membrane to prevent the failures that were seen with the syringe device. Both devices performed comparably to commercially produced products but can be made in house at a fraction of the cost.

5.1.3 3D Printing as a tool for Scientific Research

As mentioned above, 3D printing is useful in creating devices to determine information of biological relevance, however 3D printing has many more potential applications. Initially, 3D printing was used for rapid prototyping and design. Now scientific researchers are pushing 3D printing to the next level of functionality and mimicry. Functionality comes in the form of tools that replace commercially available products. Mimicry comes in the form of reproduced physical objects.

The creation of functional tools is a fast growing area of 3D printing and will expand in the near future.[4,40] The ability to make what is needed as it is needed will greatly decrease the foot print of the lab. For instance, in remote areas such as outer space, resources and storage are limited. The ability to rapidly manufacture replacement parts or new tools would be beneficial. This is something that NASA has been doing and working to make better.[41,42]

The reproduction of physical objects aids both teaching and medical care. Having students print physical objects such as energy diagrams or crystal structures has been proven to improve comprehension and test scores.[40,43] In medical care, 3D printing organs or tumors from body scans allows for novel surgical planning. The ability to practice a surgical procedure beforehand can increase the quality of patient care and decrease the chance of complications.[44,45]

5.2 Future Direction for 3D Printing

5.2.1 Material

As mentioned several times throughout this work, 3D printers were primarily used for rapid prototyping of mainly design elements. This seminal work has greatly limited the available materials that can be 3D printed. As 3D printing has moved from a prototyping tool to a manufacturing tool, the array of available materials has increased. This has led to quality materials with a wide array of mechanical properties for the lower resolution printers, FDM and SLS. However, high-resolution printers, polyjet, SLA, DLP, have a limited selection of materials. These materials are often proprietary and chemical properties not available. The lack of understanding of the surface chemistry of the resin leads to issues such as nonspecific binding especially with small molecules. With Polyjet machines, the issues with surface chemistry are compounded by the soft sacrificial support material. When a device is printed in contact with the support material, a mixed layer of hard plastic and support material remains even after cleaning, further changing the surface properties. Some work has been done in coating the 3D printed plastics with well characterized polymers, PDMS, vapor depositing fluorinated polymers, and even direct functionalization of the surface, in order to reduce these effects.

5.2.2 Support Free Printing

For printing complex or highly detailed parts, supporting the printed part is an important issue. Whether support material is made from hard plastic or a soft material its presence changes the design, dimensions, and functionality of the part. A large portion of this work would not have been possible without advances in support free printing. That

being noted, a lot of this work was also limited by the fact that not all geometries can be printed free of support material. The ability to print multiple materials completely support free would allow for more complex geometries, and more robust incorporation of membranes or other materials.

One method for working around the support issue is to utilize non-printable material as a support structure. One such method would be to print complex channels or structures then lay a membrane over top of the device to support a new print job on top. To accomplish this, modification of the printer would be required, and all models would need to be drawn in multiple parts. For example, if a serpentine channel was required one part would be drawn with an open channel then a second part would be drawn to close off the channel. The first part would be printed, a membrane laid to cover the channel, the Z-axis dropped such that when the printer was started for the next model it would print directly on top of the previous part. Utilizing this with PolyJet technology allows the research to take advantage of the multiple material capabilities for O-rings and septa as well as the high resolution of the printer. The advantage of this technique is limited to no postprocessing or cleaning of the printed device. **Figure 5.1** shows three devices with serpentine channels that were printed in this fashion, reaching channels as small as 101 µm square. While not shown here, utilizing this technique channels as small as 200 µm x 28 µm were achieved. More work is needed to determine the minimum channel size and maximum internal void that can be supported with this technique.

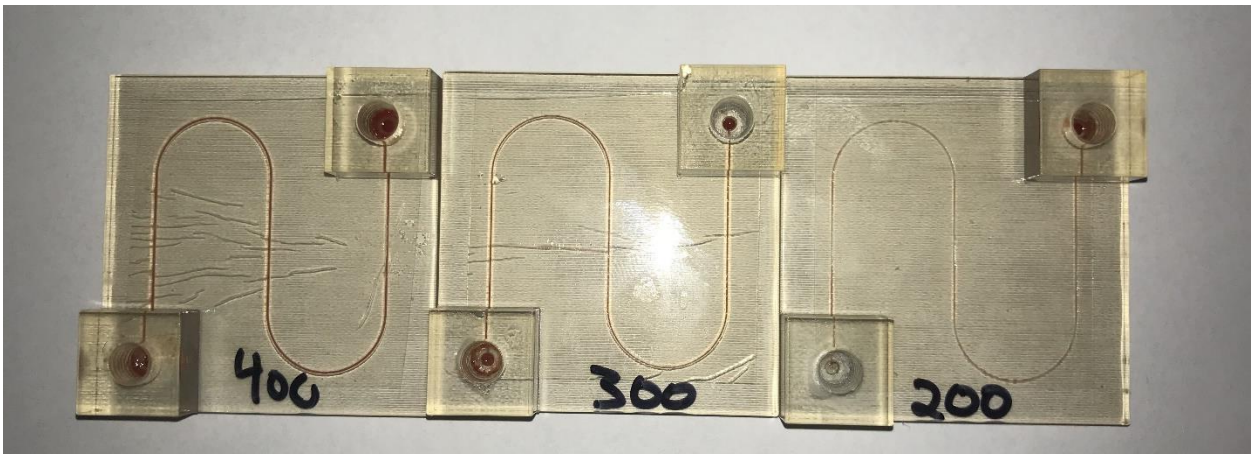

Figure 5.1: 3D printed flow devices with serpentine channels. Working left to right 400 µm, 300 µm, and 200 µm square shaped channels. These were printed in two components. The first component had the open channel, once this component was finished a polycarbonate membrane was laid on the device to close off the channel. The print stage was dropped and a second component was printed on top with two holes, an inlet and outlet to allow access to the channel. A 7% suspension of RBCs was successfully flowed through each channel.

5.3 Future Direction of Diabetic Related Research

5.3.1 Selective Cell-to-Cell Communication

Ultimately, it is naive to think that looking at the communication between three cell types will give a complete picture of the function of messenger molecules in the body. There are about 200 identified cell types in the body, with RBCs, glial cells, endothelial cells, dermal fibroblasts, platelets, and bone marrow cells comprising about 97% of the total cell count. It is logical to conclude that a majority of the signaling in the body will interact in some form with these cell types. This information should lead to a more complex flow device being developed to incorporate at minimum the six cell types listed above and pancreatic β-cells for diabetes related work. Utilizing diabetic conditions or even diabetic blood to monitor how the liver cells are storing glucose or how kidney model systems are processing the waste could be accomplished with this system.

With the skills that have been developed in 3D printing, specifically, the ability to incorporate membranes and the ability to modify print geometries to print support free, one could envision a more complex dual flow device with wells that sit on top for cell culture. This device could separate white blood cells and red blood cells to study long range communication between the blood cell types and between other cell types in the body. Such a device has been sketched in **Figure 5.2**. The blue components are sheets of membrane while the hard plastic is depicted in grey. In this crude work up, the wells are drawn as simple one compartment wells, but they could easily be modified to the nested design proposed in Chapter 2 for selective communication.

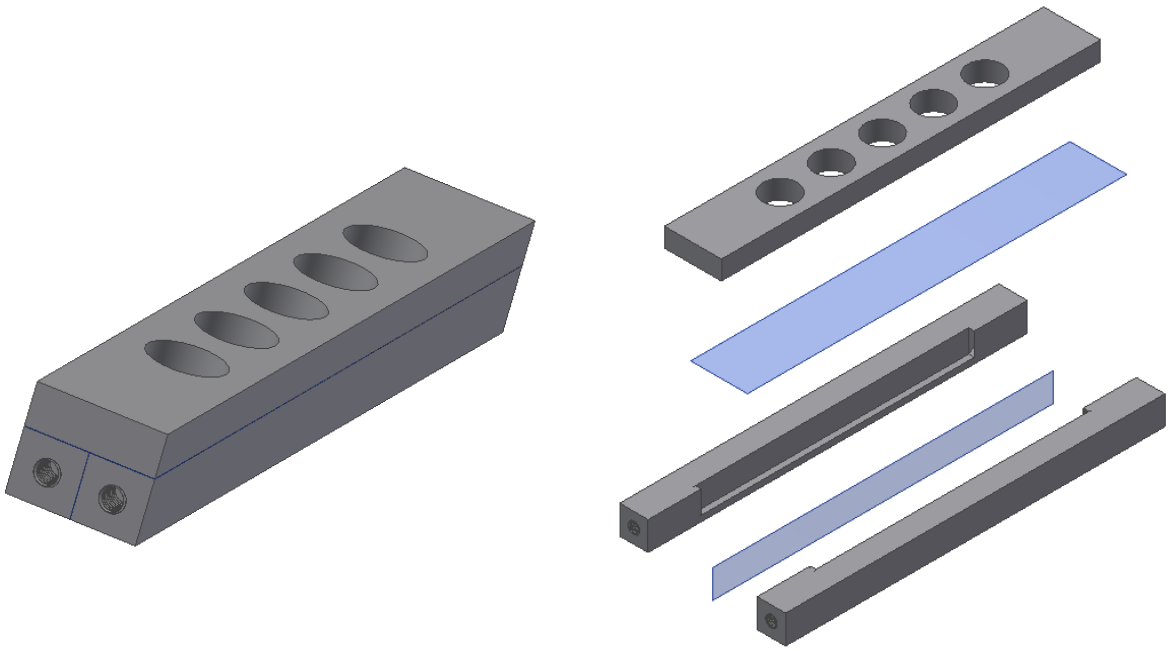

Figure 5.2: Proposed multiflow cell to cell communication device. (Left) assembled version with threaded ports on either end and wells for stagnant cell culture above flowing channels. (right) Component view of proposed multiflow cell to cell communication device. Membranes are depicted in blue and hard plastic is depicted in gray. The bottom components would be printed separately, and UV welded together with a membrane in between. Then a second print job would be run to embed the membrane on top of the channels but underneath the wells.

5.3.2 Protein Binding Under Diabetic Conditions

It was shown in Chapter 3 that post translational modifications can affect the function of proteins in vivo. Specifically, it was shown that under diabetic conditions albumin that is glycated has compromised function when looking at its ability to bind or carry zinc throughout the body. This discovery was made possible by the development of cheap and disposable devices for the determination of protein binding. More work is needed to understand how these post translational modifications affect function within the body. Our theory suggests that there is intricate interplay between zinc, albumin, and C-peptide within the body that assists in proper blood flow within the body. However, if anyone of these components is compromised in any way, the entire system may break down. The inability for glycated albumin to effectively interact with zinc could explain some of the trends seen when C-peptide is implemented in human trails. If the patient's albumin is compromised due to long term diabetic conditions that are not seen in the animal trials the injected formulation may need to be modified in order to provide those beneficial effects in vivo.

REFERENCES

REFERENCES

(1) Jose, R. R.; Rodriguez, M. J.; Dixon, T. A.; Omenetto, F.; Kaplan, D. L. Evolution of Bioinks and Additive Manufacturing Technologies for 3D Bioprinting. ACS Biomater. Sci. Eng. **2016**, 2 (10), 1662–1678.

(2) Chen, C.; Mehl, B. T.; Munshi, A. S.; Townsend, A. D.; Spence, D. M.; Martin, R. S. 3D-Printed Microfluidic Devices: Fabrication, Advantages and Limitations - a Mini Review. Anal. Methods **2016**, 8 (31), 6005–6012.

(3) Gong, H.; Bickham, B. P.; Woolley, A. T.; Nordin, G. P. Custom 3D Printer and Resin for 18 Mm × 20 Mm Microfluidic Flow Channels. Lab Chip **2017**, 17 (17), 2899–2909.

(4) Lücking, T. H.; Sambale, F.; Beutel, S.; Scheper, T. 3D-Printed Individual Labware in Biosciences by Rapid Prototyping: A Proof of Principle. Eng. Life Sci. **2015**, 15 (1), 51–56.

(5) Shirazi, S. F. S.; Gharehkhani, S.; Mehrali, M.; Yarmand, H.; Metselaar, H. S. C.; Adib Kadri, N.; Osman, N. A. A. A Review on Powder-Based Additive Manufacturing for Tissue Engineering: Selective Laser Sintering and Inkjet 3D Printing. Sci. Technol. Adv. Mater. **2015**, 16 (3), 1–20.

(6) Murphy, S. V.; Atala, A. 3D Bioprinting of Tissues and Organs. Nat. Biotechnol. **2014**, 32 (8), 773–785.

(7) Johnson, R. D. Custom Labware: Chemical Creativity with 3D Printing. Nat. Chem. **2012**, 4 (5), 338–339.

(8) Jariwala, S. H.; Lewis, G. S.; Bushman, Z. J.; Adair, J. H.; Donahue, H. J. 3D Printing of Personalized Artificial Bone Scaffolds. 3D Print. Addit. Manuf. **2015**, 2 (2), 56–64.

(9) Hofmann, M. 3D Printing Gets a Boost and Opportunities with Polymer Materials. ACS Macro Lett. **2014**, 3 (4), 382–386.

(10) Vaezi, M.; Yang, S. Extrusion-Based Additive Manufacturing of PEEK for Biomedical Applications. Virtual Phys. Prototyp. **2015**, 10 (3), 123–135.

(11) Gross, B.; Lockwood, S. Y.; Spence, D. M. Recent Advances in Analytical Chemistry by 3D Printing. Anal. Chem. **2017**, 89 (1), 57–70.

(12) Gross, B. C.; Erkal, J. L.; Lockwood, S. Y.; Chen, C.; Spence, D. M. Evaluation of 3D Printing and Its Potential Impact on Biotechnology and the Chemical Sciences. Anal. Chem. **2014**, 86 (7), 3240–3253.

(13) Bhattacharjee, N.; Urrios, A.; Kang, S.; Folch, A. The Upcoming 3D-Printing Revolution in Microfluidics. Lab Chip **2016**, 16 (10), 1720–1742.

(14) Tibbits, S. 4D Printing. Archit. Des. **2014**, 84 (1), 116–121.

(15) Stratasys. No Title http://www.stratasys.com/materials.

(16) Harrisox, R. G. Observations on the Living Developing Nerve. Anat. Rec. **1907**, 116–128.

(17) Breslin, S.; O'Driscoll, L. Three-Dimensional Cell Culture: The Missing Link in Drug Discovery. Drug Discov. Today **2013**, 18 (5–6), 240–249.

(18) Saltiel, A. R.; Kahn, C. R. Insulin Signalling and the Regulation of Glucose and Lipid Metabolism. Nature **2001**, 414 (6865), 799–806.

(19) Ekim Üstünel, B.; Friedrich, K.; Maida, A.; Wang, X.; Krones-Herzig, A.; Seibert, O.; Sommerfeld, A.; Jones, A.; Sijmonsma, T. P.; Sticht, C.; et al. Control of Diabetic Hyperglycaemia and Insulin Resistance through TSC22D4. Nat. Commun. **2016**, 7 (May), 1–11.

(20) Holland, A. M.; Go, L. J.; Naselli, G.; MacDonald, R. J.; Harrison, L. C. Conditional Expression Demonstrates the Role of the Maintenance and Regeneration of {b}-Cells in the Adult. Diabetes **2005**, 54 (September), 2586–2595.

(21) Entwistle, K. PANCREATIC SECRETIONS AND THEIR EFFECT ON CIRCULATORY AND IMMUNE CELLS, 2016.

(22) Meyer, J. A.; Subasinghe, W.; Sima, A. A. F.; Keltner, Z.; Reid, G. E.; Daleke, D.; Spence, D. M. Zinc-Activated C-Peptide Resistance to the Type 2 Diabetic Erythrocyte Is Associated with Hyperglycemia-Induced Phosphatidylserine Externalization and Reversed by Metformin. Mol. Biosyst. **2009**, 5 (10), 1157–1162.

(23) Meyer, J. A.; Froelich, J. M.; Reid, G. E.; Karunarathne, W. K. A.; Spence, D. M. Metal-Activated C-Peptide Facilitates Glucose Clearance and the Release of a Nitric Oxide Stimulus via the GLUT1 Transporter. Diabetologia **2008**, 51 (1), 175–182.

(24) Medawala, W.; McCahill, P.; Giebink, A.; Meyer, J.; Ku, C. J.; Spence, D. M. A Molecular Level Understanding of Zinc Activation of C-Peptide and Its Effects on Cellular Communication in the Bloodstream. Rev. Diabet. Stud. **2009**, 6 (3), 148–158.

(25) Sima, A. A. F.; Zhang, W.; Sugimoto, K.; Henry, D.; Li, Z.; Wahren, J.; Grunberger, G. C-Peptide Prevents and Improves Chronic Type I Diabetic Polyneuropathy in the BB/Wor Rat. Diabetologia **2001**, 44 (7), 889–897.

(26) Johansson, B. L.; Borg, K.; Fernqvist-Forbes, E.; Kernell, A.; Odergren, T.; Wahren,

J. Beneficial Effects of C-Peptide on Incipient Nephropathy and Neuropathy in Patients with Type 1 Diabetes Mellitus. Diabet Med **2000**, 17, 181–189.

(27) Cotter, M. A.; Ekberg, K.; Wahren, J.; Cameron, N. E. Effects of Proinsulin C-Peptide in Experimental Diabetic Neuropathy: Vascular Actions and Modulation by Nitric Oxide Synthase Inhibition. Diabetes **2003**, 52 (7), 1812–1817.

(28) Ekberg, K.; Brismar, T.; Johansson, B. L.; Jonsson, B.; Lindström, P.; Wahren, J. Amelioration of Sensory Nerve Dysfunction by C-Peptide in Patients with Type 1 Diabetes. Diabetes **2003**, 52 (2), 536–541.

(29) Wahren, J.; Foyt, H.; Daniels, M.; Arezzo, J. C. Long-Acting C-Peptide and Neuropathy in Type 1 Diabetes: A 12-Month Clinical Trial. Diabetes Care **2016**, 39 (4), 596–602.

(30) Hage, D. S. Analysis of Biological Interactions by Affinity Chromatography: Clinical and Pharmaceutical Applications. Clin. Chem. **2017**, 63 (6), 1083–1093.

(31) Pinger, C. W.; Heller, A. A.; Spence, D. M. A Printed Equilibrium Dialysis Device with Integrated Membranes for Improved Binding Affinity Measurements. Anal. Chem. **2017**, 89 (14), 7302–7306.

(32) Albumin Structure, Function and Uses, 1st ed.; Rosenoer, V., Oratz, M., Rothschild, M., Eds.; 1977.

(33) Brownlee, M. Biology of Diabetic Complications. Nature **2001**, 414 (December), 813–820.

(34) Brownlee, M.; Cerami, A.; Vlassara, H. Advance Glycosylation End Products in Tissue and the Biochemical Basis of Diabetic Complications. Semin. Med. Beth Isr. Hosp. Bost. **2010**, 318 (20), 1315–1321.

(35) Association, A. D. Diagnosis and Classification of Diabetes Mellitus. Diabetes Care **2010**, 33 (SUPPL. 1), S62–S69.

(36) Michael J. Fowler, M. Microvascular and Macrovascular Complications of Diabetes. Clin. Diabetes **2008**, 26 (2), 77–82.

(37) Forst, T.; Kunt, T.; Wilhelm, B.; Weber, M. M.; Pf, A. Role of C-Peptide in the Regulation of Microvascular Blood Flow. Exp. Diabetes Res. **2008**, 2008.

(38) Anguizola, J.; Matsuda, R.; Barnaby, O. S.; Hoy, K. S.; Wa, C.; DeBolt, E.; Koke, M.; Hage, D. S. Glycation of Human Serum Albumin. Clin. Chim. Acta **2013**, 425, 64–76.

(39) Barnaby, O. S.; Cerny, R. L.; Clarke, W.; Hage, D. S. Comparison of Modification Sites Formed on Human Serum Albumin at Various Stages of Glycation. Clin. Chim. Acta **2011**, 412 (3–4), 277–285.

(40) Chen, T.-H.; Lee, S.; Flood, A. H.; Miljanić, O. Š. How to Print a Crystal Structure Model in 3D. CrystEngComm **2014**, 16 (25), 5488–5493.

(41) Schubert, C.; Van Langeveld, M. C.; Donoso, L. A. Innovations in 3D Printing: A 3D Overview from Optics to Organs. Br. J. Ophthalmol. **2014**, 98 (2), 159–161.

(42) Leach, N. 3D Printing in Space. Archit. Des. **2014**, 84 (6), 108–113.

(43) Kaliakin, D. S.; Zaari, R. R.; Varganov, S. A. 3D Printed Potential and Free Energy Surfaces for Teaching Fundamental Concepts in Physical Chemistry. J. Chem. Educ. **2015**, 92 (12), 2106–2112.

(44) Wang, K.; Ho, C. C.; Zhang, C.; Wang, B. A Review on the 3D Printing of Functional Structures for Medical Phantoms and Regenerated Tissue and Organ Applications. Engineering **2017**, 3 (5), 653–662.

(45) Klein, G. T.; Lu, Y.; Wang, M. Y. 3D Printing and Neurosurgery--Ready for Prime Time? World Neurosurg. **2013**, 80 (3–4), 233–235.